TRIGGERED EARTHQUAKES AND TREMOR:

THEIR CHARACTERISTICS AND PHYSICAL MECHANISMS

A Dissertation
Presented to
The Academic Faculty

by

Chastity Aiken

In Partial Fulfillment
of the Requirements for the Degree
Doctorate of Philosophy in the
School of Earth & Atmospheric Sciences

Georgia Institute of Technology
August 2015

TRIGGERED EARTHQUAKES AND TREMOR:

THEIR CHARACTERISTICS AND PHYSICAL MECHANISMS

Approved by:

Dr. Zhigang Peng, Advisor
School of Earth & Atmospheric Sciences
Georgia Institute of Technology

Dr. Christian Huber
School of Earth & Atmospheric Sciences
Georgia Institute of Technology

Dr. Andrew Newman
School of Earth & Atmospheric Sciences
Georgia Institute of Technology

Dr. Constantine Dovrolis
School of Computer Science
Georgia Institute of Technology

Dr. Josef Dufek
School of Earth & Atmospheric Sciences
Georgia Institute of Technology

Date Approved: April 6, 2015

The more that you read, the more things you will know.
The more that you learn, the more places you'll go.

- Dr. Seuss, *I Can Read With My Eyes Shut!*

I dedicate this dissertation
to my beloved dog, Ana,
whose unconditional love will never be forgotten.

ACKNOWLEDGEMENTS

The success I have endured the last 5 years would not have been possible without my advisor, Zhigang Peng. He has been a great foundation of support since I was a Physics undergraduate student at Georgia State University. From the very beginning, he has challenged my critical thinking. I remember early on I was afraid to answer his questions, in the case I would say something wrong. However, I now realize that throughout all these years he has helped me to find the strength I will need for overcoming challenges when I am beyond his open door. Zhigang has not only supported me academically but also professionally throughout my graduate career. His constant encouragement to petition for any and all professional opportunities has awarded me adventures, experiences, and a robust network of colleagues in the scientific community that will remain with me for a lifetime. Reflecting back, I see that Zhigang has helped me discover in part who I am as a scientist and what I want most out of my career, and for that, I am extremely grateful.

I entered graduate school aspiring to learn more about seismology, never expecting that I would be gaining life lessons in the process. By the very nature of the people who are the foundation of geophysics at Georgia Tech, I have been enlightened in more ways than I can express. I appreciate Andy Newman for never going easy on me, never restraining his opinion of my work. His criticism was hard to accept in the beginning but has made me more resilient. I am thankful to Joe Dufek for his patience, understanding, and willingness to always provide an open ear for a quick discussion. His openness has taught me that solutions come from expressing ideas and to never be afraid

to ask. I appreciate Chris Huber for showing me that modeling is not as scary as I originally thought. Lastly, I am grateful to Dr. Constantine Dovrolis for happily agreeing to serve on my thesis committee in the last few months. But most importantly, I appreciate all of my thesis committee members for helping me understand what success really is. Prior to entering graduate school, I firmly believed that success meant never failing. However, they have taught me that success means not losing enthusiasm when the research road gets tough.

There are countless others who have immeasurably helped me throughout my graduate school experience to whom I would like to show appreciation. I am grateful to Kevin Chao, who took me under his wing much like a big brother and has (and continues to) provide valued advice, support, and discussion regarding my research. I thank my husband, John Mark, who from the moment I met has supported every adventure I have sought and reminds me to this day that laughter is a great remedy for stress. I am thankful for Shannon and Irene, who taught me life balance. I am also grateful to the staff and regular volunteers of Trees Atlanta for their constant support and boundless friendship over the last 5 years. And finally, I thank my family and family-in-law, who have shown me that even the smallest successes are worth celebrating.

TABLE OF CONTENTS

LIST OF TABLES

LIST OF FIGURES

SUMMARY

Earthquake triggering occurs when a fault has been pushed to failure by additional stress loading. It has been observed worldwide that large, shallow earthquakes are capable of loading faults, thereby triggering additional earthquakes and tremors. Since seismic activity arises when a fault has reached its critical state of stress, earthquakes and tectonic tremor can be used as a probe for understanding a fault's stress state, especially when these events are triggered by an external source (for more details, see Chapter 1). My Ph.D. research has focused on systematically investigating dynamic triggering of earthquakes and tremors to better understand the characteristics of and the physical mechanisms responsible for triggering. Specifically, I investigate dynamic triggering of earthquakes in three geothermal/volcanic regions of California (Chapter 2), and I examine dynamic triggering of tremor along three strike-slip faults in the Western Hemisphere (Chapter 3), namely the Queen Charlotte Margin (Canada), eastern Denali Fault (Canada), and Enriquillo-Plantain Garden Fault (Haiti). The ultimate goal is to not only understand how earthquakes and tremor nucleate but to also gain a deeper understanding of fundamental fault behavior in these regions.

Chapter 2 highlights a systematic survey of local earthquakes triggered by distant earthquakes in three geothermal/volcanic regions of California: Long Valley Caldera, Coso Geothermal Field, and Geysers Geothermal Field. Waveforms of distant earthquakes with magnitudes (M) $\geq$ 5.5 occurring between 2000 and 2012 were examined for triggering, and β-statistics were computed to confirm the significance of the findings. The percentage of distant events triggering in Long Valley, Coso, and Geysers vary –

2.0%, 3.8%, and 6.8% in the 12 year period, respectively – and when compared to the triggering of tectonic tremors along the Parkfield-Cholame section of San Andreas Fault (SAF, 9.2% in the 12 year period). Apparent triggering thresholds vary among the regions with Long Valley having the highest of ~5 kPa and ~1 kPa for the other regions. In addition, the frequency contents of the triggering waves do not appear to be a dominant factor that controls triggering. Overall, the variation in triggering behavior is likely a reflection of faults having a tendency to be at or near failure, such that a region with a higher background activity rate is more susceptible to triggering.

Chapter 3 highlights three studies of tremor triggered along strike-slip faults in the Western Hemisphere – the Queen Charlotte Margin (Canada), eastern Denali Fault (Canada), and Enriquillo-Plantain Garden Fault (Haiti). In the Queen Charlotte Margin and eastern Denali Fault regions, I conduct a systematic survey of large earthquakes triggering tremor, while along the Enriquillo-Plantain Garden Fault I present the results of tremor triggered by the 27 February 2010 *Mw*8.8 Maule, Chile earthquake. In general, the tremor in these regions has frequencies ranging from 5 to 40 Hz and is modulated by the surface waves of large, shallow earthquakes. However, which surface wave triggers (Love or Rayleigh) is controlled by the incidence of the seismic wave on the fault. In the Queen Charlotte Margin and eastern Denali Fault regions, I investigate the peak dynamic stress caused by these earthquakes and find a similar triggering threshold, i.e. dynamic stress $\geq$ 10 kPa is needed to push the faults to failure. An examination of the frequency contents of the triggering waves reveals that long-period (>20 s), high amplitude surface waves are predominantly responsible for triggering tremor. Along the Enriquillo-Plantain Garden Fault, I find tremor that is triggered primarily by the Love wave of the Maule

mainshock, which is in agreement with high triggering potential for a Love wave with near vertical incidence on a left-lateral strike-slip fault. I also search for aftershock activity of 12 January 2010 *Mw*7.0 Haiti earthquake that is possibly influenced by the seismic waves of the Chile mainshock but currently find no evidence of increased aftershock activity.

Systematic surveys of earthquake and tremor triggering presented here indicate whether amplitude, frequency, and incidence of the triggering waves on faults can be used to predict whether or not triggering will occur. For earthquake triggering, peak dynamic stress appears to be the primary controlling factor. On the other hand, tremor triggering is controlled by amplitude, frequency, and incidence. Earthquake triggering primarily occurs in geothermal regions with extensional tectonics, and geothermal regions with higher background activity rates are most susceptible triggering. However, tremor triggering occurs much more often than earthquake triggering (at least in California) and predominately in compressional or transpressional tectonic environments. The observation that tremor is triggered more often than earthquakes could be a reflection of a fault being weaker at depth (where tremor occurs) than in the shallower crust (where earthquakes occur). Potential research directions related to the topic of dynamic triggering are presented in Chapter 4.

CHAPTER 1

INTRODUCTION

1.1 Background

Earthquakes and tectonic tremor are two manifestations of fault failure that can be dynamically triggered. An earthquake is a seismic signal that emerges from a sudden slip on the locked portion of a fault, has distinct *P*- and *S*-waves, and can have a broad range of frequencies (1-100 Hz). Tectonic tremor (hereafter 'tremor'), on the other hand, is a seismic signal thought to emerge from faults where properties and behaviors are transitional between locked and creeping [*Obara*, 2002]. The tremor signal itself is embedded with low-frequency earthquakes (LFEs) [*Shelly et al.*, 2007] that when conflated in a short amount of time appear to behave like a packet of *S*-waves and with no distinct *P*-waves. Tremor embedded with LFEs generally has frequencies of 1-10 Hz [e.g., *Peng and Gomberg*, 2010], but tremor has also been shown to contain frequencies up to 40 Hz [e.g., *Guilhem et al.*, 2010].

Triggering is considered to occur as a result of additional stress loading that promotes fault failure 'ahead of schedule' [e.g., *Gomberg*, 2010]. Additional stress loading can arise due to stress perturbations caused by earthquakes, solid earth tides, anthropogenic activities, etc. Earthquakes generate stress changes in Earth's crust due to permanent deformation (static stress changes) and passing seismic waves (dynamic stress changes). Both static and dynamic stress changes caused by earthquakes can load faults and push them closer to failure. In the near-field (i.e., within 1-2 fault rupture lengths of an earthquake), static stress changes are capable of promoting failure on adjacent faults, resulting in increased earthquake and tremor activity [e.g., *King et al.*, 1994; *Harris et al.*, 1995; *Nadeau and Guilhem*, 2009]. On the other hand, dynamic stress changes arising from passing seismic waves are capable of triggering in the near-field as well as the far-

field, well beyond a few fault rupture lengths where static stress changes no longer dominate [e.g. *Hill et al.*, 1993; *Kilb et al.*, 2000].

The discovery of dynamic triggering more than two decades ago [*Hill et al.*, 1993] offers new insights into earthquake interaction at long-range distances but also fault behaviors during an earthquake cycle. Dynamic triggering can occur in a wide range of tectonic environments [e.g., *Brodsky and Prejean*, 2005; *Velasco et al.*, 2008; *Peng and Gomberg*, 2010]. Geothermal/volcanic environments with extensional and transtensional tectonics are more susceptible to earthquake triggering due to the presence of fluids [e.g., *Hill and Prejean*, 2007; *Aiken and Peng*, 2014 and references therein]. On the other hand, triggered tremor has been observed in areas of high pore pressure within compressional subduction zones [*Peng and Gomberg*, 2010; *Beroza and Ide*, 2011] and transpressional environments such as the strike-slip SAF in California [e.g., *Peng et al.*, 2009]. In most cases, tremor and earthquakes are induced by surface waves of distant earthquakes, i.e. by the Love and Rayleigh waves. However, body wave triggering has also been observed [*Ghosh et al.*, 2009; *Miyazawa*, 2012; *Hill et al.*, 2013].

Tremor and earthquake activity can be triggered on critically stressed faults, according to the Coulomb-Failure criterion [*Hill,* 2012]. One proposed mechanism for fault failure is that fluids can be pressurized on pre-existing fractures as a result of dynamic strain from passing seismic waves, which lowers a fault's effective normal stress pushing it toward failure [*Hill et al*., 1993; *Rubinstein et al.*, 2007]. Furthermore, *Brodsky and Prejean* [2005] found that large-amplitude and long-period (>30s) surface waves from distant earthquakes are most effective at triggering earthquakes via fluid pressurization in geothermal/volcanic regions. Similar amplitude and frequency dependence has been observed for the triggering of tremor [*Peng et al.*, 2009; *Guilhem et al.*, 2010]. Other characteristics of triggering include phase-correlated triggering [e.g. *Brodsky and Prejean*, 2005], phase-uncorrelated triggering [*Peng et al.*, 2010], and triggering that occurs after surface waves have already passed either by a simple

cascading effect [*Brodsky*, 2006], a delayed effect [*Shelly et al.*, 2011], or multiple surface waves circling the earth [*Peng et al.*, 2011].

1.2 Motivation

Earthquake and tremor triggering has been observed throughout the world [e.g., *Pollitz et al.* 2014; *Peng and Gomberg*, 2010]. For instance, earthquake triggering has mostly been observed in geothermal/volcanic regions [e.g., *Hill and Prejean*, 2014], while triggered tremor has mostly been detected within subduction zones around the Pacific Rim [*Peng and* Gomberg, 2010] and along a few strike-slip faults in California [e.g., *Shelly et al.*, 2011; *Chao et al.,* 2012a]. Little is understood about the characteristics of and physical mechanisms responsible for triggering. There are several key questions related to triggering, such as when, where, and how does triggering occur and how do different regions compare where it is observed. For example, does tremor occur on strike-slip faults beyond California? By conducting systematic investigations of triggering, we gain not only knowledge of the physical processes responsible for the occurrence of earthquakes and tremor but also a deeper understanding of fundamental fault behavior and how earthquakes and tremor nucleate. Furthermore, understanding how fault systems respond to external stressing and how earthquakes and tremor nucleate offers vital information for seismic hazard assessment.

The investigation of earthquake and tectonic tremor triggering is relatively simple, for a couple of reasons. First, earthquake and tremor triggering can occur during or immediately following the passing seismic waves of an earthquake, and thus we know when to look for triggering to occur. Second, triggered tremor generally radiates larger amplitude signals than spontaneous (ambient) tectonic tremor, which makes triggered tremor more easily distinguishable from noise in seismic data [e.g., *Rubinstein et al.*, 2007; *Peng et al.*, 2008].

Beyond the objective of understanding of how earthquakes and tremor occur on active faults, the research presented here provides a foundation for addressing the larger question about the role of tremor activity in earthquake cycles. Specifically, it has been suggested that ambient tremor activity that occurs deep within faults transfers stress to the shallower portion of a fault where earthquakes occur [e.g., *Wech and Creager*, 2011]. Because triggered tremor is ambient tremor occurring 'ahead of schedule' [*Gomberg*, 2010], discovering regions where triggered tremor occurs launches new opportunities for the investigation of ambient tremor activity and its role with earthquake cycles in those regions.

1.3 Preview of Subsequent Chapters

In the subsequent chapters, I present published papers as well as some preliminary work that will be submitted for publication at a later date. In Chapter 2, I present results of a systematic survey of triggered earthquakes in three geothermal/volcanic regions of California [*Aiken and Peng*, 2014], namely Long Valley Caldera, Coso Geothermal Field, and Geysers Geothermal Field. In Chapter 3, I show the results of three systematic surveys of tremor triggered along strike-slip faults: the Queen Charlotte Margin of Haida Gwaii, Canada [*Aiken et al.*, 2013a], along the eastern Denali Fault in western Yukon Territory, Canada [*Aiken et al*., 2015b], and along the Enriquillo-Plantain Garden Fault in the southern Haiti peninsula [*Aiken et al.*, 2015a which is in preparation for publication]. Chapter 4 (the final chapter) provides reflections on the work presented here and possible future research directions for studies on the topic of dynamic triggering. There are also 3 appendices. Appendix A details how to estimate dynamic stress from an earthquake's magnitude. Appendix B shows how to compute the β- and Z-statistics using MatLab. Appendix C provides a list of papers I authored and co-authored during my Ph.D.

CHAPTER 2

DYNAMIC TRIGGERING OF MICROEARTHQUAKES IN THREE GEOTHERMAL REGIONS OF CALIFORNIA

The results presented in this chapter are from the work of *Aiken and Peng* [2014].

Summary

Geothermal/volcanic regions are most susceptible to local earthquake triggering by regional and remote earthquakes. Transient stresses caused by surface waves of these earthquakes can activate critically stressed faults. Though earthquakes can be triggered in geothermal/volcanic regions, it is less understood how these regions differ in their triggering responses to distant earthquakes. We conduct a systematic survey of local earthquakes triggered by distant earthquakes in three geothermal/volcanic regions of California: Long Valley Caldera, Coso Geothermal Field, and Geysers Geothermal Field. We examine waveforms of distant earthquakes with magnitudes ≥ 5.5 occurring between 2000 and 2012 and compute β-statistics to confirm the significance of our findings. We find that Long Valley, Coso, and Geysers vary in triggering frequency – 2.0%, 3.8%, and 6.8% in the 12 year period, respectively – and when compared to the triggering of deep tectonic tremors along the Parkfield-Cholame section of SAF (9.2% in the 12 year period). Stress triggering thresholds vary among the regions with Long Valley having the highest of ~5 kPa and ~1 kPa for the other regions. Because dynamic stresses from distant earthquakes are similar in these three regions, the varying triggering behavior likely reflects faults having a tendency to be at or near failure. This is compatible with Geysers having a higher *a*-value in the Gutenberg-Richter relationship and higher geothermal productivity than the other two regions. The observation of more frequency

triggering of tremor than microearthquakes is consistent with recent laboratory studies on increasing triggerability with lower effective stress.

2.1 Introduction

Surface waves of large, distant earthquakes at a few fault lengths away can dynamically trigger microearthquakes and deep tectonic tremor in differing tectonic regimes including extensional, transtensional, and transpressional environments [*Brodsky and Prejean,* 2005; *Hill and Prejean,* 2014 and references therein; *Velasco et al.*, 2008; *Peng and Gomberg*, 2010]. Among them, geothermal/volcanic regions are mostly associated with extensional or transtensional environments and often contain repeatedly triggered earthquakes [*Stark and Davis*, 1996; *Hough and Kanamori*, 2002; *Bhattacharyya and Lees*, 2002; *Hill*, 2006]. On the other hand, recent studies [e.g. *Peng and Gomberg*, 2010; *Aiken et al.*, 2013b] have shown that deep tectonic tremor is mostly observed in compressional (subduction zones) or transpressional environments, e.g. the SAF, the Queen Charlotte Fault, etc.

Although microearthquake triggering in geothermal/volcanic regions has been documented, it is not well understood how geothermal/volcanic regions differ in their triggering responses as compared with other tectonic regions. The objective of this study is to compare behaviors of microearthquake triggering in three geothermal/volcanic regions of California. We also compare our earthquake triggering observations with tremors triggered along the Parkfield-Cholame segment of the SAF. Such a comparison will illuminate similarities and/or differences between microearthquake and tremor triggering, specifically in California. Furthermore, Parkfield, CA is ideal for the comparison of microearthquake and tremor triggering for two reasons. First, tremors have

been triggered along the Parkfield-Cholame segment by passing seismic waves of many large distant events [e.g. *Ghosh et al.*, 2009; *Peng et al.*, 2008, 2009; *Guilhem et al.*, 2010; *Shelly et al.*, 2011]. Second, the Parkfield-Cholame segment is in the regional neighborhood (within 300 km) of Long Valley, Coso, and Geysers, which allows for a simple comparison between dynamic stresses of earthquakes in each region.

2.2 Tectonic Settings

California has 3 notable geothermal/volcanic regions that are suitable for comparing dynamic triggering of microearthquakes: Long Valley Caldera, Coso Geothermal Field, and Geysers Geothermal Field. Long Valley Caldera is located on the eastern edge of the Sierra Nevada Mountains in the Basin and Range Province of eastern California (Figure 2.1a). Coso Geothermal Field is located in the southwestern portion of the Basin and Range Province, bounded by the Sierra Nevada Mountains and the Coso Range (Figure 2.1b). The last region, Geysers Geothermal Field, is located in northern California about 130 km north of San Francisco (Figure 2.1c). Each of these geothermal/volcanic regions has not only active fault systems but also active fluid processes that account for their high background seismicity rate, which could be one of the many reasons that contribute to their susceptibility to dynamic triggering [*Hill and Prejean*, 2014].

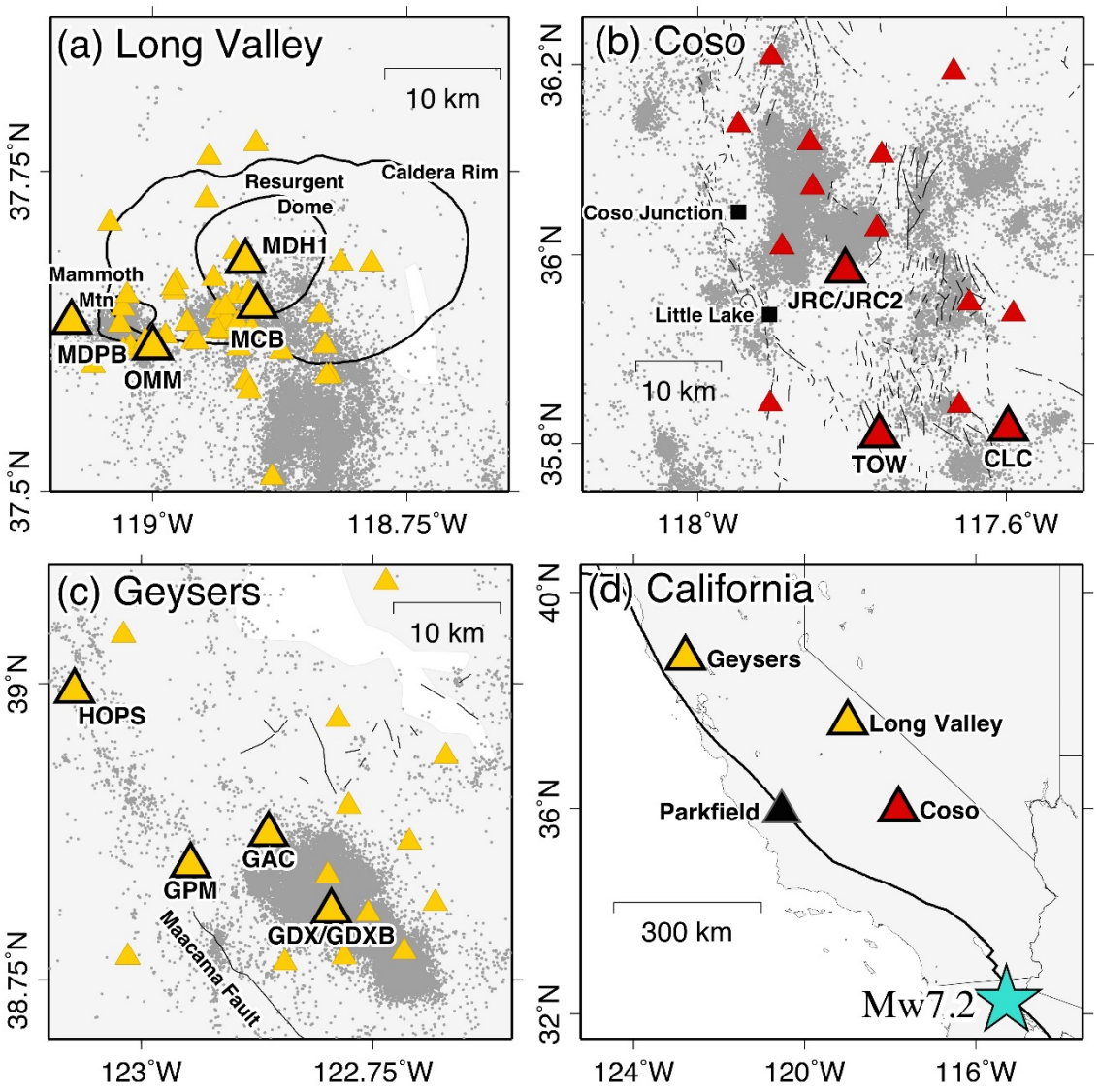

Figure 2.1 - Map view of three geothermal regions in California. Gray dots represent background seismicity during the 2000 - 2012 study period. Locations are marked in black text. Black lines = faults and/or outline of tectonic features. Yellow triangles = Northern California Seismic Network (NCSN) stations. Red triangles = Southern California Seismic Network (SCSN) stations. Larger triangles = stations used either for the dynamic stress calculation or as a second station for visual observations. **(a)** Long Valley Caldera. **(b)** Coso Geothermal Field. **(c)** Geysers Geothermal Field. **(d)** California. Main reference station from each region is marked, as well as the PKD station in Parkfield, CA. Turquoise star = 4 April 2012 *M*7.2 Baja California earthquake.

Previous studies have observed dynamic triggering at the Brawley/Salton Sea Geothermal Field in Southern California [*Hough and Kanamori*, 2002; *Doran et al.*, 2011]. However, we exclude this region in this study for two reasons. First, while several

surface-based broadband stations (CI network) exist in this region, the waveform quality for local events is relatively poor due to thick sediment and near-surface attenuation. High-quality borehole station (EN network) only became available since December 2007, which is not comparable to our study time period of 2000 to 2012. Second, Salton Sea is relatively far from the other study regions in central and northern California. Hence, the list of teleseismic events could be different. Because our primary purpose is to select the same distant events and compare their triggering behavior at different sites, we did not include the Salton Sea region in this study.

2.3 Analysis and Procedure

We first selected distant earthquakes that occurred during the 2000-2012 period and that have a depth < 100 km from the Advanced National Seismic System (ANSS, accessible via the Northern California Earthquake Data Center) catalog. Next, we separate them into two groups. In the first group, we selected earthquakes with magnitude (M) ≥ 5.5 and an epicentral distance between 100 km and 2,000 km from each region's reference station. The second group was comprised of earthquakes with $M \geq 7.5$ and an epicentral distance over 2,000 km from each region's reference station. *Brodsky and Prejean* [2005] chose a similar minimum distance of 100 km because transient dynamic stresses are expected to dominate over static stress changes at such distance [*Freed*, 2005]. In addition, it is relatively easy to separate seismic signals of locally triggered microearthquakes and triggering mainshocks occurring at relatively large distances [*Guilhem et al.*, 2010]. The reference stations for Long Valley, Coso, Geysers, and Parkfield are OMM, JRC2, GDXB, and PKD, respectively. Given these selection criteria, we obtained ~150 distant earthquakes for each region (Tables S2.1-S2.4).

After selecting our distant earthquakes, we retrieved ±5 hours of seismic data from the Northern California Earthquake Data Center (NCEDC) and Southern California Earthquake Data Center (SCEDC) around the *P*-wave arrival of each selected earthquake. Seismic data from both broadband and short period stations in each region were used to identify locally triggered microearthquakes. We first discarded broadband waveforms that were clipped or poorly recorded. We then removed the instrument response and rotated the broadband horizontal waveforms to the great circle path (GCP, radial) and a clockwise 90° rotation (transverse) direction using the Seismic Analysis Code (SAC) command "rotate to GCP." Next, we applied filters to detect triggered microearthquakes. Filters we used were either high-pass > 5 Hz to avoid contamination of body waves from distant events or band-pass filters (e.g., 2-16 Hz, 15-30 Hz) to avoid local noise contamination. We applied all three filters to determine the best choice. We then took the Hilbert transform of the filtered trace and computed the envelope function using SAC's command "envelope", and smoothed it with a half width of 50 data points using SAC's command "smooth h 50". Finally, for each station, we computed an averaged envelope function by stacking the filtered radial, transverse, and vertical component envelope functions and dividing by 3. For earthquakes that appeared to instantaneously trigger microearthquakes, we used the filtered envelope functions and filtered seismograms together to hand-pick local seismic activity that occurred ±5 hours around the *P*-wave arrival. In particular, we hand-picked microearthquakes that had distinct *P*- and *S*-waves and $S-P$ time < 10 seconds, which is appropriate for local earthquakes within ~80 km of the seismic station.

We estimated the magnitudes of the hand-picked microearthquakes using the following steps. First, we identified a hand-picked microearthquake that was also listed in the earthquake catalog. Second, we measured the *S*-wave amplitude of the same hand-picked microearthquake from a nearby station. Third, we assumed that a tenfold increase in displacement amplitude corresponds to an increase in one unit magnitude [*Peng et al.*, 2007] and estimated the constant to convert $\log_{10}$(amplitude) to local magnitude *M*. We then used the *S*-wave amplitudes of all hand-picked events in conjunction with our calibration constant to estimate the magnitude of microearthquakes not listed in the catalog. Admittedly, this is a simple estimation of earthquake magnitude. Since we do not locate the hand-picked events, we do not include the distance effect in the magnitude estimation for each hand-picked earthquake. Moreover, we note that our calibration constant assumes that all of our hand-picked events occur at the same distance as our calibration earthquake listed in the earthquake catalog. However, because the magnitudes of the triggered events are mostly used for plotting purposes (e.g., Figure 2.2a), any potential errors in magnitude estimation have minor effects on the overall conclusion of this study.

We verified increases in seismic activity following the surface wave arrival by calculating the β-statistic [e.g. *Aron and Hardebeck*, 2009]. For broadband stations without clipped or poorly recorded data, we determine the β-values from the hand-picked events. The β-statistic values were computed by

$$\beta = \frac{N_a - N(T_a / T))}{\sqrt{N(T_a / T)(1-(T_a / T))}}. \quad (2.1)$$

The variables T_a and T are the time periods for the triggering window and the sum of the triggering time window and 5 hours before the *P*-wave of the distant earthquake,

respectively. That is, $T = T_a + T_b$, where T_b is the time window before the *P*-wave of the distant earthquake. We defined two triggering windows: instantaneous and delayed. The instantaneous triggering window is the time between the 5 km s^{-1} and 2 km s^{-1} wave arrival of the distant earthquake, when most of the surface wave energy is captured [e.g., *Peng et al.*, 2009]. The delayed triggering window is the time between the 2 km s^{-1} wave arrival and up to 5 hours after the *P*-wave arrival. The variables N_a and N are the number of events in the triggering time window and the total number of events occurring in the triggering time window and 5 hours before the *P*-wave arrival, respectively. That is, $N = N_a + N_b$, where N_b is the number of events occurring in the time window before the *P*-wave. When at least one microearthquake was identified following the distant event, we computed β-statistic values for both the instantaneous and delayed triggering windows using all hand-picked events and those above the median amplitude of hand-picked events occurring after the *P*-wave arrival (Table S2.5).

We chose ± 5 hours mainly for the following reasons. While recent studies have shown that delayed triggering can occur days after seismic waves have already passed [e.g. *Parsons et al.,* 2014], here we focus on short-term delayed triggering which has been shown to follow an Omori Law decay [*Brodsky*, 2006]. Another potential difficulty is that it is rather time consuming to hand-pick microearthquakes at three regions for hundreds of distant mainshocks. Hence, in this study, we limit our waveform examination period to be a few hours before and after each distant mainshock. In general, a β-statistic ≥ 2 indicates a significant increase in seismic activity as compared to background seismic activity at ~95% confidence level [e.g., *Hill and Prejean*, 2014]. In addition to computing the β-statistic values using our hand-picked events, when possible, we also cross-

examined our hand-picked microearthquakes with ANSS earthquake catalogs obtained from NCEDC to determine if a clear increase in seismicity around the surface wave arrival time could be seen in both approaches.

Finally, to compare triggering thresholds in each region, we applied a 1-s low-pass filter to the instrument-corrected seismograms prior to measuring the peak ground velocity (PGV) to avoid bias due to local earthquake activity. Using the measured PGV values, a shear rigidity (μ) of 30 GPa and surface wave phase velocities (v_{ph}) of 4.3 km s^{-1} and 3.5 km s^{-1} for the Love and Rayleigh waves, respectively, we computed the maximum dynamic stress (σ) generated by distant earthquakes, similar to *Aiken et al.* [2013a], as

$$\sigma = \frac{(\mathrm{PGV})(\mu)}{v_{ph}}. \tag{2.2}$$

2.4 Triggering Observations

Triggered earthquake observations from each geothermal/volcanic region as well as triggered tremor observations along the Parkfield-Cholame segment of the SAF will be discussed individually in the following four subsections.

2.4.1 Long Valley Caldera

Of the 149 distant earthquakes we examined for triggering in Long Valley, we observed microearthquakes triggered by surface waves of 3 distant earthquakes: the 3 November 2002 *M*7.9 Denali Fault (dynamic stress (σ) = 78 kPa), 15 June 2005 *M*7.2 Mendocino (σ = 43 kPa), and 4 April 2010 *M*7.2 Baja California earthquakes (σ = 18 kPa) (Table S2.1). Triggering by the 2002 *M*7.9 Denali earthquake in Long Valley has

been documented by previous studies [*Prejean et al.*, 2004; *Brodsky and Prejean*, 2005]. These 3 triggering earthquakes account for about 2.0% of the 149 earthquakes we examined.

Figure 2.2 is an example of triggering in Long Valley by the 2010 Baja California earthquake, where the transverse (T) and vertical (Z) components exemplify its Love and Rayleigh waves, respectively. We did not include the radial (R) component mainly because it shows similar Rayleigh waves as the Z component except with a 90° phase shift. One microearthquake occurred during the Love wave arrival at ~250 seconds. It has an estimated magnitude of ~1.6 and was not listed in the ANSS catalog. Three more microearthquakes occurred during the subsequent Rayleigh wave up until around 400 seconds. In total, we were able to identify 47 microearthquakes in the 5 hours following the *P*-wave arrival of the 2010 Baja California earthquake. These events were only visible on the MDH1 station, which is a borehole station deployed at 2.5 km at depth with a sampling rate of 500 samples/s. We did not use the surface broadband station MCB because the data was clipped due to the amplitude of this earthquake. Figure 2.3a is another example of triggering in Long Valley by the 2005 *M*7.2 Mendocino earthquake. Only 2 earthquakes were triggered during the Rayleigh wave (~300 seconds) and the coda, and 22 microearthquakes in total occurred up to 5 hours after the *P*-wave using station MCB (Figure S2.1).

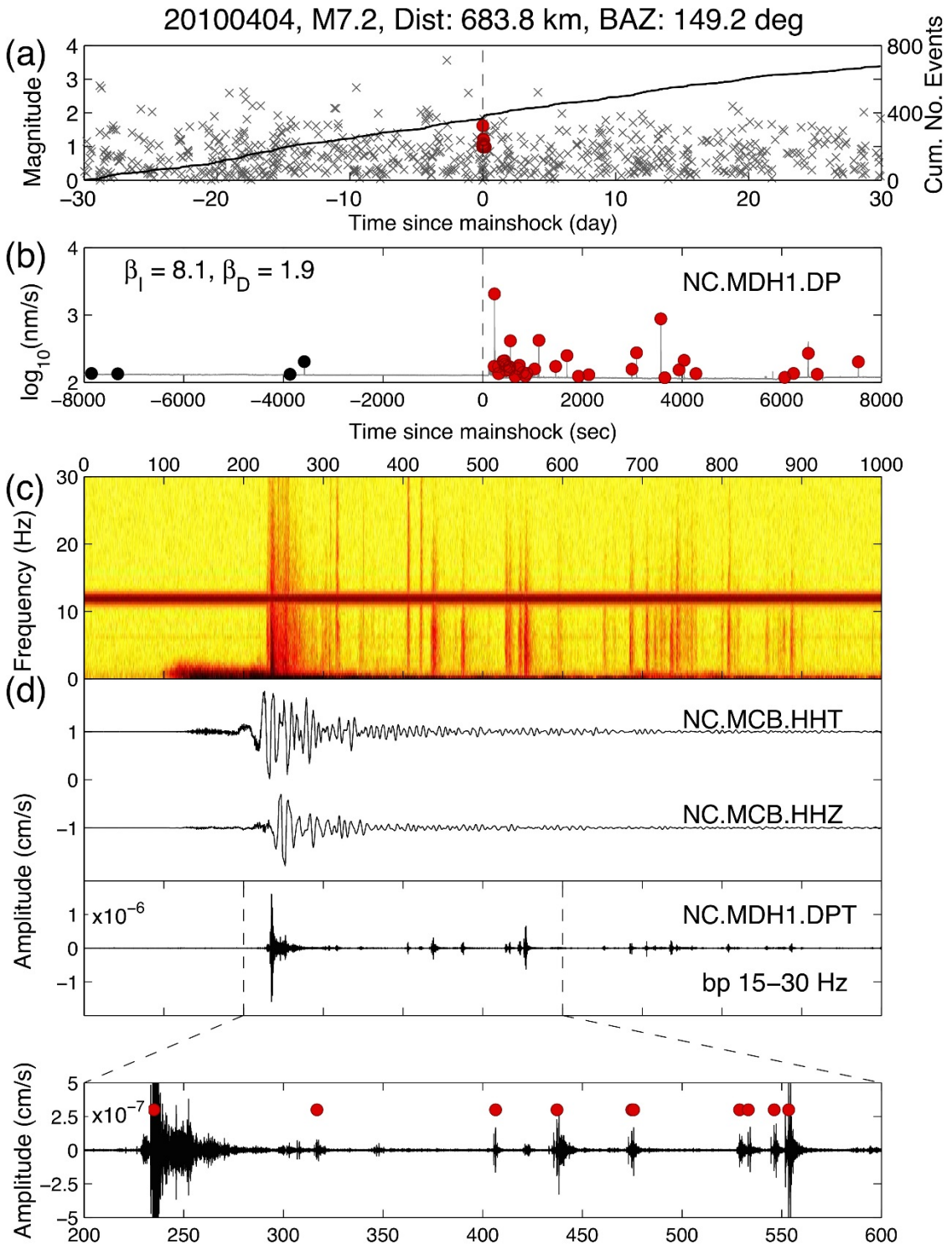

Figure 2.2 - Earthquakes triggered in Long Valley Caldera by the 2010 *M*7.2 Baja California earthquake. **(a)** 60-day seismicity around the mainshock origin time with cumulative number of events. Earthquakes listed in the ANSS earthquake catalog are indicated by a gray "x" and are from the Long Valley region illustrated in Figure 2.1. Red circles represent manually picked events. **(b)** Band-pass filtered (15-30 Hz) envelope

function as recorded by the MDH1 station. Black circles represent manually picked events before the *P*-wave arrival. Red circles are manually picked events after the *P*-wave arrival. β-value without regard to amplitude threshold is indicated – instantaneous (I) and delayed (D). All sequential figures contain similar computed β-values, i.e. no amplitude threshold criterion is applied. **(c)** Spectrogram with high-frequency bursts representative of local earthquakes. There is a constant noise source around 12 Hz. **(d)** Instrument-corrected broadband velocity seismograms from station MCB band-pass filtered (15-30 Hz) to show triggered microearthquakes, with zoom in of triggered microearthquake activity. We show seismic activity on the borehole MDH1 station because more triggered microearthquakes are visible on this station.

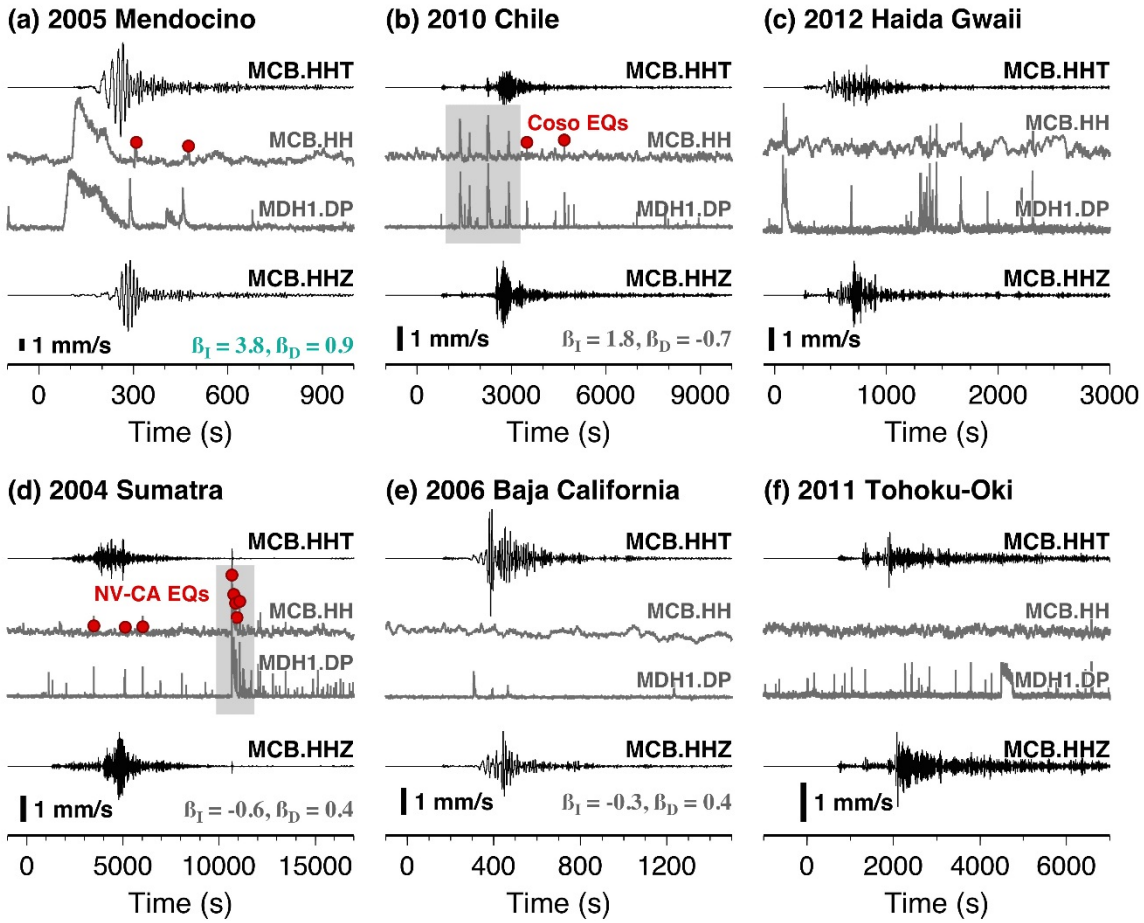

Figure 2.3 - Additional examples of triggering and non-triggering in Long Valley Caldera. In each panel, the broadband transverse, high-passed > 5 Hz averaged filtered envelopes, and broadband vertical waveforms are plotted. We show both the surface MCB station and borehole MDH1 station. The vertical bar in each panel indicates the amplitude for broadband data in that panel. For earthquakes that appeared to trigger seismicity, we hand-picked local microearthquakes (red circles) from the waveform and computed their β-statistics. β-statistics in turquoise are considered as statistically significant (i.e. triggers); β-statistics in grey are considered as non-triggers. We did not hand-pick microearthquakes for all distant earthquakes and so some spikes may represent

either earthquakes or noise. Gray boxes in (b) and (d) illustrate earthquakes radiating from Coso and the Nevada-California border, respectively. Symbols and notation are the same as in Figure 2.2.

It is worth mentioning that several large, distant earthquakes that have triggered microearthquakes/tremor in other regions [e.g. *Peng et al.*, 2009, 2010] did not trigger microearthquakes in Long Valley. For example, the 26 December 2004 *M*9.0 Sumatra (σ = 16 kPa), 27 February 2010 *M*8.8 Chile (σ = 14 kPa), and 11 March 2011 *M*9.0 Tohoku-Oki (σ = 10 kPa) mainshocks did not trigger any statistically significant activity during large amplitude surface waves (Figure 2.3b-f). The 2004 Sumatra earthquake appears to trigger a cluster of microearthquakes at ~11,000 seconds after the passage of surface waves. However, this cluster of events occurred in a seismically active region about 40 km northeast of Long Valley, near the Nevada-California border [*Velasco et al.*, 2008]. Hence, they cannot be considered as triggered seismicity associated with Long Valley. Similarly, the four high-frequency bursts that occurred during the teleseismic waves of the 2010 Chile mainshock shown in Figure 2.3b were associated with triggered seismicity in the Coso geothermal/volcanic region [*Peng et al.*, 2010], instead of originating from Long Valley. Lastly, no microearthquakes were detected on the MCB surface station during the surface waves of the 2006 Baja California earthquake (σ = 13 kPa)(Figure 2.3e). However, a few events appear to be triggered on the MDH1 borehole station. After hand-picking events on the MDH1 station, we found that the instantaneous β-value is -0.3, and thus, the 2006 Baja California earthquake does not appear to have dynamically triggered microearthquakes in Long Valley.

2.4.2 Coso Geothermal Field

In Coso Geothermal Field, we examined a total of 156 distant earthquakes for locally triggered microearthquakes and found 6 triggering earthquakes (Table S2.2). These 6 cases account for 3.8% of the 156 earthquakes we examined. Of these 6 triggering earthquakes, the 2002 *M*7.9 Denali (σ = 37 kPa) and 2010 *M*8.8 Chile earthquakes (σ = 9 kPa) were analyzed in previous studies [e.g. *Prejean et al.*, 2004; *Peng et al.*, 2010, 2011]. Thus, we have identified 4 additional triggering events: the 2005 *M*7.2 Mendocino (σ = 8 kPa) earthquake, as well as the 4 January 2006 *M*6.6 (σ = 8 kPa), 3 August 2009 *M*6.9 (σ = 35 kPa), and 2010 *M*7.2 Baja California (σ = 102 kPa) earthquakes.

Figure 2.4 shows an example of microearthquakes triggered in Coso by the 2009 Baja California earthquake. During its large-amplitude surface waves, we identified 8 triggered microearthquakes with estimated magnitudes *M* ranging from ~0.1 to 1, with the largest of these occurring during the Rayleigh wave around 340 seconds. Five hours prior to the 2009 Baja California earthquake, Coso Geothermal Field was relatively quiet as we detected only 2 local earthquakes during this period. Up to 5 hours after the *P*-wave arrival, we identified a total of 27 microearthquakes, most of which occurred in the first hour following the surface wave arrivals.

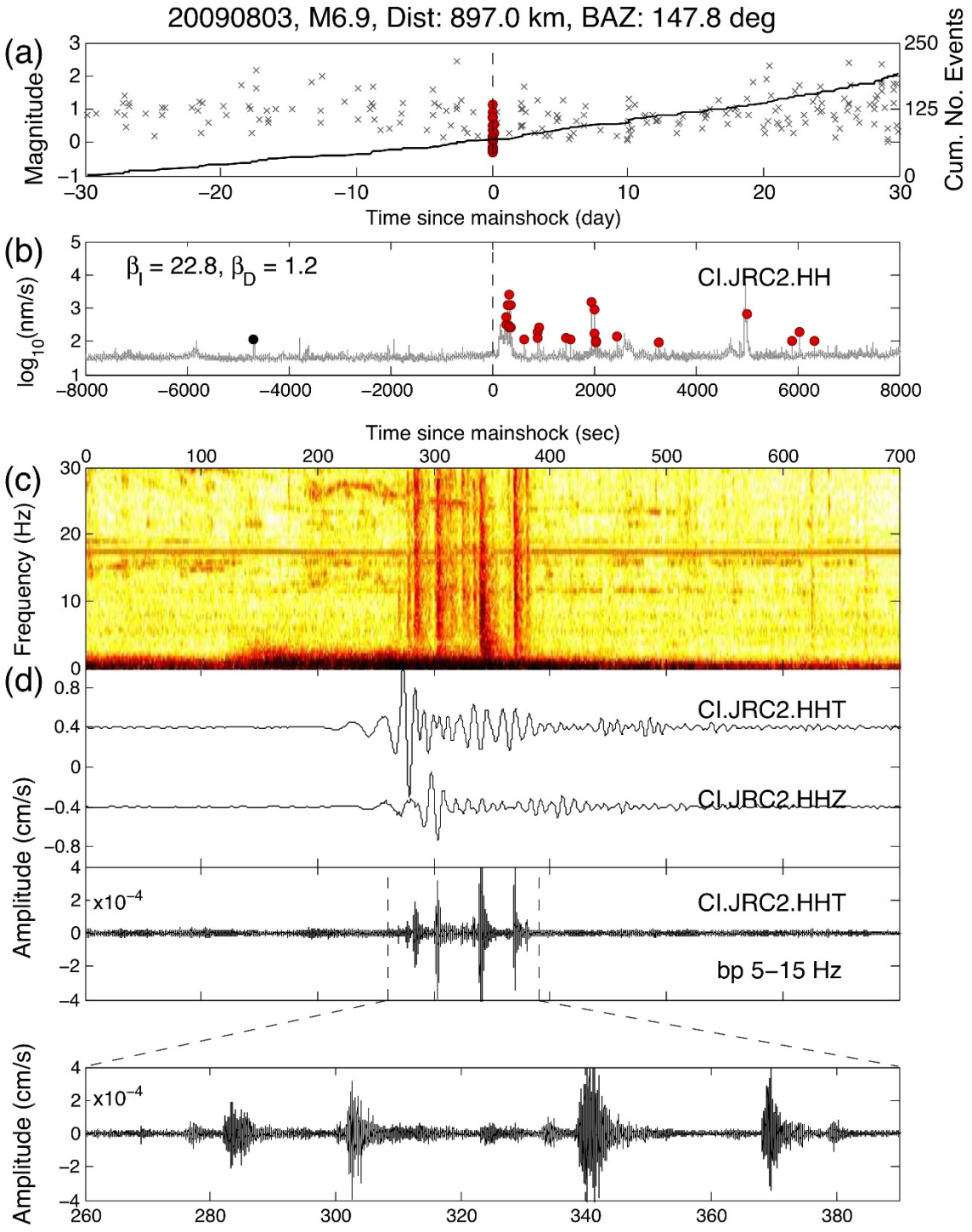

Figure 2.4 - Earthquakes triggered in Coso Geothermal Field by the 2009 *M*6.9 Baja California earthquake. Symbols and notation are the same as in Figure 2.2. Earthquakes ("x") are listed in the ANSS earthquake catalog and are from the Coso region illustrated in Figure 2.1. The high β-value of 22.8 indicates that the microearthquakes were triggered by dynamic stresses of the 2009 Baja California earthquake.

The 2006 and 2010 Baja California earthquakes also triggered microearthquakes in this region (Figure 2.5). Compared to the 2009 Baja California mainshock, these earthquakes triggered only 1-2 microearthquakes during the wavetrain and ~30 events in total 5 hours after the *P*-wave arrival (Figure S2.2). Similarly, the 2006 Baja California and 2005 Mendocino earthquakes triggered seismicity in Coso during their surface waves with β-values larger than 2, suggesting that the triggering is statistically significant with 95% confidence (Figure 2.5c, 2.5e). Similar to Long Valley, many large distant earthquakes did not trigger microearthquakes at Coso based on β-value calculations, such as the 2004 *M*9.0 Sumatra (σ = 10 kPa, Figure 2.5b), 29 September 2009 *M*8.1 Samoa (σ = 8 kPa, Figure 2.5d), and 22 January 2003 *M*7.6 Colima earthquakes (σ = 6 kPa, Figure 2.5f). In particular, the 2009 Samoa earthquake appears to trigger 2 microearthquakes around the *S*-wave arrival, but these microearthquakes did not synchronously occur with the peaks of the *S*-wave nor was a seismicity rate increase detected.

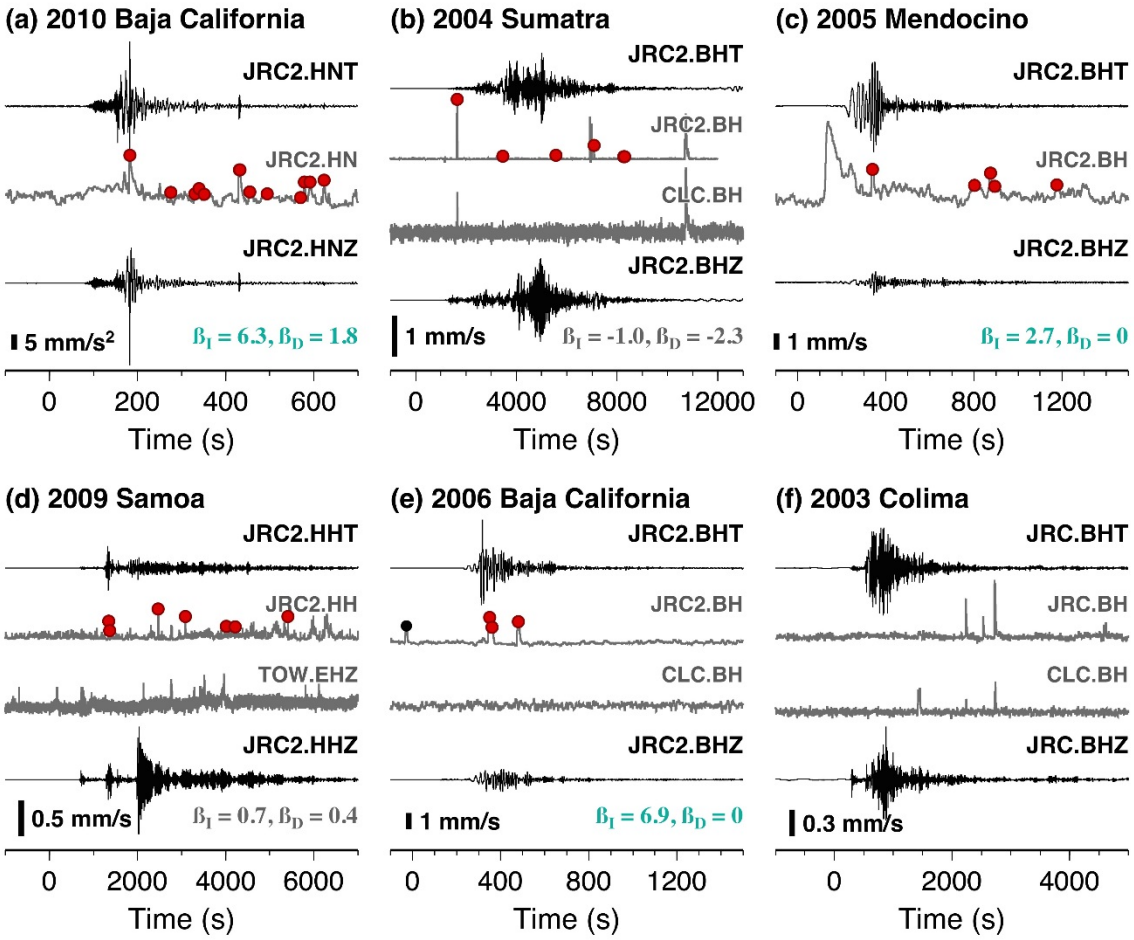

Figure 2.5 - Additional examples of triggering and non-triggering in Coso Geothermal Field. Symbols and notation are the same as in Figure 2.3. We do not show multiple stations for the 2010 Baja California earthquake because the seismic data is clipped at nearby stations. For the 2005 Mendocino earthquake, no additional waveforms were available at nearby stations. The β-values for the 2010 Baja California, 2005 Mendocino, and 2006 Baja California are all > 2, indicating significant microearthquake triggering has occurred.

2.4.3 Geysers Geothermal Field

We examined 148 distant earthquakes recorded in Geysers Geothermal Field, and 10 of these events triggered microearthquakes (Table S2.3), which account for 6.8% of the 148 earthquakes we examined. These include the 2002 *M*7.9 Denali (σ = 26 kPa) [*Prejean et al.*, 2004; *Brodsky and Prejean*, 2005] and the 2005 *M*7.2 Mendocino (σ = 18 kPa) [*Brodsky*, 2006] earthquakes that were previously reported as microearthquake

triggers in Geysers. The remaining 8 triggering earthquakes were the 23 June 2001 *M*8.4 Peru (σ = 5 kPa), 2003 *M*7.6 Colima (σ = 4 kPa), 2006 *M*6.6 Baja California (σ = 4 kPa), 13 January 2007 *M*8.1 Kuril Islands (σ = 12 kPa), 2009 *M*6.9 Baja California (σ = 21 kPa), 10 January 2010 *M*6.5 Northern California (σ = 10 kPa), 2010 *M*8.8 Chile (σ = 9 kPa), and 2010 *M*7.2 Baja California (σ = 29 kPa) earthquakes.

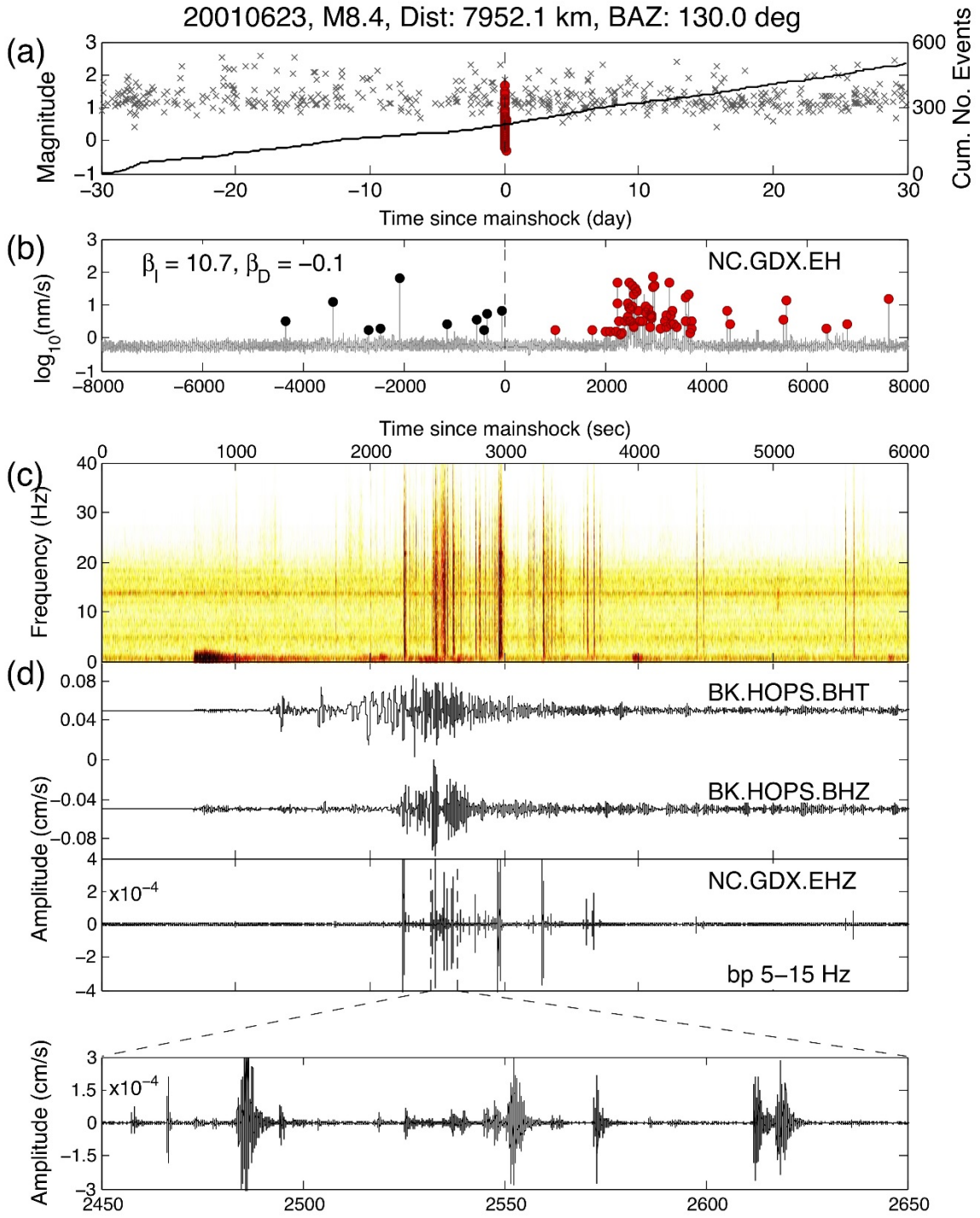

Figure 2.6 - Earthquakes triggered in Geysers Geothermal Field by the 2001 *M*8.4 Peru earthquake. Symbols and notation are the same as in Figure 2.2. We show the HOPS broadband waveforms because the GDXB station did not come on-line until 2004. Earthquakes ("x") are listed in the ANSS earthquake catalog and are from the Geysers region illustrated in Figure 2.1. The β-value of 10.7 indicates that the microearthquakes were triggered by dynamic stresses of the 2001 Peru earthquake.

Figure 2.6 shows microearthquakes triggered in Geysers by the 2001 Peru earthquake. We detected 22 local earthquakes 5 hours prior to the *P*-wave arrival of the 2001 Peru earthquake. In comparison, we identified 76 local earthquakes up to 5 hours after the *P*-wave arrival. Most of these triggered microearthquakes occurred during or immediately following the teleseismic surface waves of the 2001 Peru mainshock. Specifically, we detected over 50 microearthquakes triggered during the Rayleigh wave between ~2200 and ~3800 seconds. Only one smaller magnitude (M<1) was identified during the Love wave at ~2000 seconds. Furthermore, we detected 49 and 147 triggered microearthquakes during and immediately following the surface waves of the 2009 and 2010 Baja California earthquakes, respectively, with ~25 events occurring prior to the *P*-wave arrival in both cases (Figure 2.7a, 2.7c). We note that microearthquake activity triggered by the 2010 Baja California earthquake continued long after the surface waves passed. We also detected an increase in seismicity during the surface waves of the 2010 Northern California earthquake, a M6.5 far-field event that occurred 230 km (~13 fault lengths) away from Geysers (Figure 2.7e). For this earthquake, we used a 10 Hz high pass filter to avoid contamination of teleseismic body wave coda and observe events triggered during the surface waves (Figure S2.3). A similar M6.1 earthquake that occurred recently (10 March 2014, not studied in depth in this work) near the epicenter of the 2010 Northern California earthquake also triggered microearthquakes (Figure S2.4). Thus, moderate-size earthquakes from off the shore of Northern California appear to repeatedly trigger microearthquakes in Geysers, which could be a directivity effect. However, we do not explore triggering by directivity in this work.

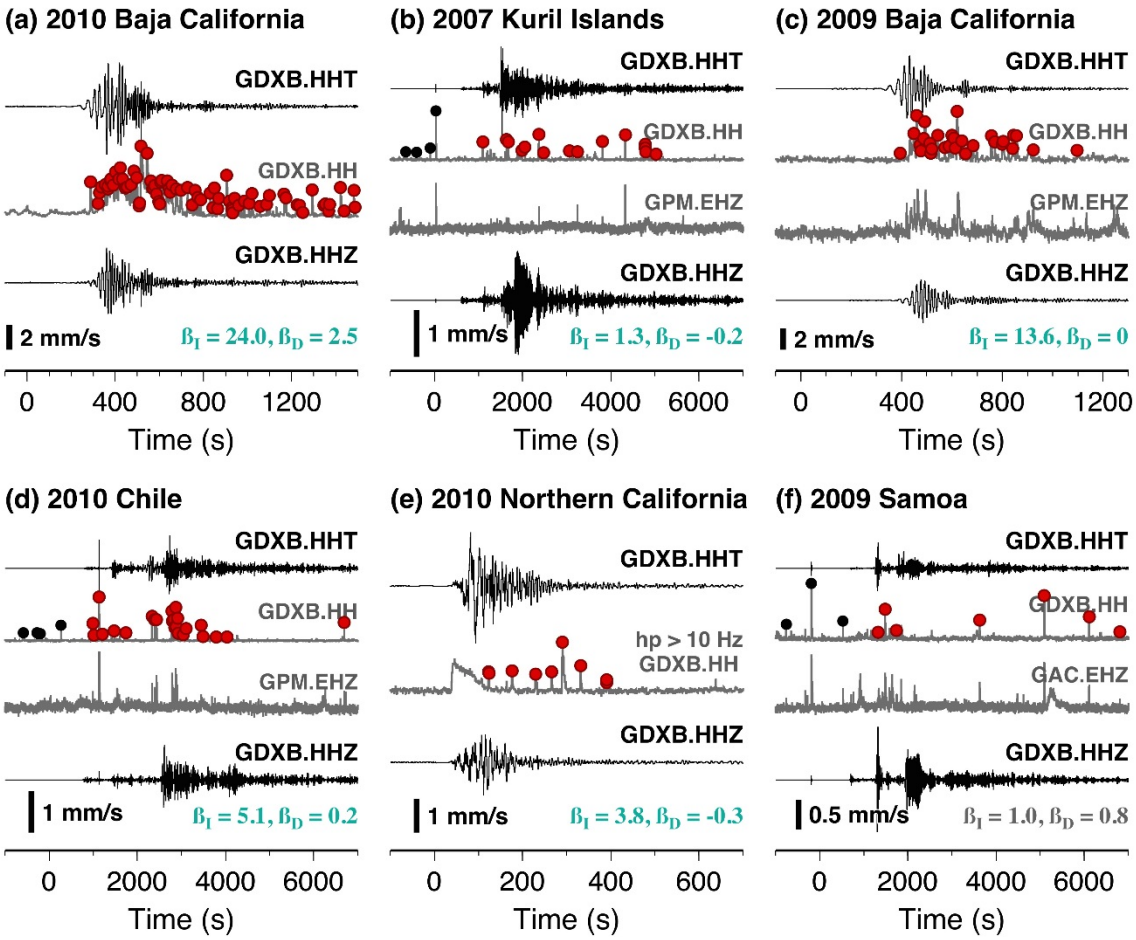

Figure 2.7 - Additional examples of triggering and non-triggering in Geysers Geothermal Field. Symbols and notation are the same as in Figure 2.3. We do not show multiple stations for the 2010 Baja California and 2010 Northern California earthquakes because the seismic data is clipped for both events at nearby stations. The β-values for the 2010 Baja California, 2009 Baja California, 2010 Chile, and 2010 Northern California earthquakes are all > 2, indicating significant microearthquake triggering has occurred.

In addition to clear evidence of triggering by these distant earthquakes, we also identified several ambiguous instances. Figure 2.7b depicts the apparent triggering of local earthquakes by passing *S*- and surface waves of the 2007 Kuril Islands earthquake. Even though these triggered microearthquakes are coincident with the *S*- and surface waves, the β-value does not show a significant increase, i.e. $\beta < 2$. This was also observed for the 2003 Colima and 2006 Baja California earthquakes in that many microearthquakes occurred during the surface waves, but the increase of seismicity rate

was not significant (Figure S2.5). Furthermore, we do not consider the 2009 Samoa earthquake triggered local events near the Geysers because the microearthquakes occurring around the time of the Love wave arrival are not coincident with the surface wave peaks, and no microearthquakes are triggered during the Rayleigh waves as was observed in several other more confident cases.

2.4.4 San Andreas Fault, Parkfield, California

Our method for identifying triggered tremor in Parkfield for comparison to triggered earthquakes is similar to our method for the geothermal/volcanic regions. We first selected distant earthquakes (see Table S2.4) and retrieved seismic data from the Northern California Earthquake Data Center for the station PKD, similar to the methods outlined in Section 2.3. The Parkfield-Cholame segment has a high-resolution seismic network, but for consistency in our analysis, we opted to use only station PKD because it is similar to the stations found in Long Valley, Coso, and Geysers. Next, we visually inspected the instrument-corrected and filtered waveforms of our selected earthquakes for events that appeared to trigger tremors – i.e. tremors triggered by the surface waves of the distant earthquakes and visible on the broadband PKD station. Our filters were similar to those used for triggered microearthquake identification. In particular, we used both low-frequency band-pass filters (e.g. 2-8 Hz, *Peng et al.* [2009]) and high-pass filters (e.g. >10 Hz *Guilhem et al.* [2010]) to detect triggered tremors. Finally, we computed β-statistic values to test the statistical significance of the tremor that appeared to be triggered by distant earthquakes. The β-values were computed using a low-frequency earthquake (LFE) template-based tremor catalog. *Shelly et al.* [2009] first detected the LFEs along the Parkfield segment using the matched filter technique and have since

continued their detections in this region. Since tremor is mainly comprised of LFEs [*Shelly et al.*, 2007], we used the LFE-based tremor catalog to detect increases in tremor activity following the passing of seismic waves from a distant event. Parkfield LFEs are detected using a 2-8 Hz matched band-pass filter across the entire high-resolution seismic network and require a correlation sum across all stations ≥ 4.0 [*Shelly and Hardebeck*, 2010]. In short, the β-values were computed similar to our analysis for detecting triggered microearthquakes in the geothermal/volcanic regions (i.e. equation 2.1); however, we used the matched-filter detected LFEs instead of hand-picking events.

Given these analysis steps, we examined 153 distant earthquakes and found that 14 of the distant earthquakes triggered tremors along the Parkfield-Cholame segment of the SAF. These 14 earthquakes account for the 9.2% of the 153 earthquakes we examined. All distant earthquakes identified as triggers can be see in Tables S2.4 and S2.5. We did not find any instances of distant earthquakes triggering microearthquakes near Parkfield, an observation similar to *Kane et al.* [2007] who investigated remote triggering along the San Jacinto Fault in southern California. Figure 2.8 shows a comparison of the triggered behaviors caused by the 2011 *Mw*9.0 Tohoku-Oki earthquake, as recorded in Parkfield (σ = 10 kPa), Long Valley (σ = 10 kPa), Coso (σ = 7 kPa), and Geysers (σ = 9 kPa). While clear tremor was observed at Parkfield [*Chao et al.*, 2013; *Hill et al.*, 2013], we did not observe any clear statistically significant increase of instantaneously triggered microearthquakes in the three geothermal/volcanic regions, though Long Valley appears to have a delayed increase in seismic activity. An additional example is the 28 October 2012 *M*7.7 Haida Gwaii earthquake (Figure S2.6). There is clear evidence of triggered tremor in Parkfield during the teleseismic waves that generate

dynamic stress of ~5 kPa. However, this mainshock did not trigger any microseismicity in the geothermal/volcanic regions – Long Valley (σ = 15 kPa), Coso (σ = 11 kPa), or Geysers (σ = 10 kPa). While there is some earthquake activity during the surface waves in Coso and Geysers, these microearthquakes are not coincident with the surface wave peaks as observed in other triggering cases (e.g., Figure 2.4) and are perhaps just a continuation of the background seismicity.

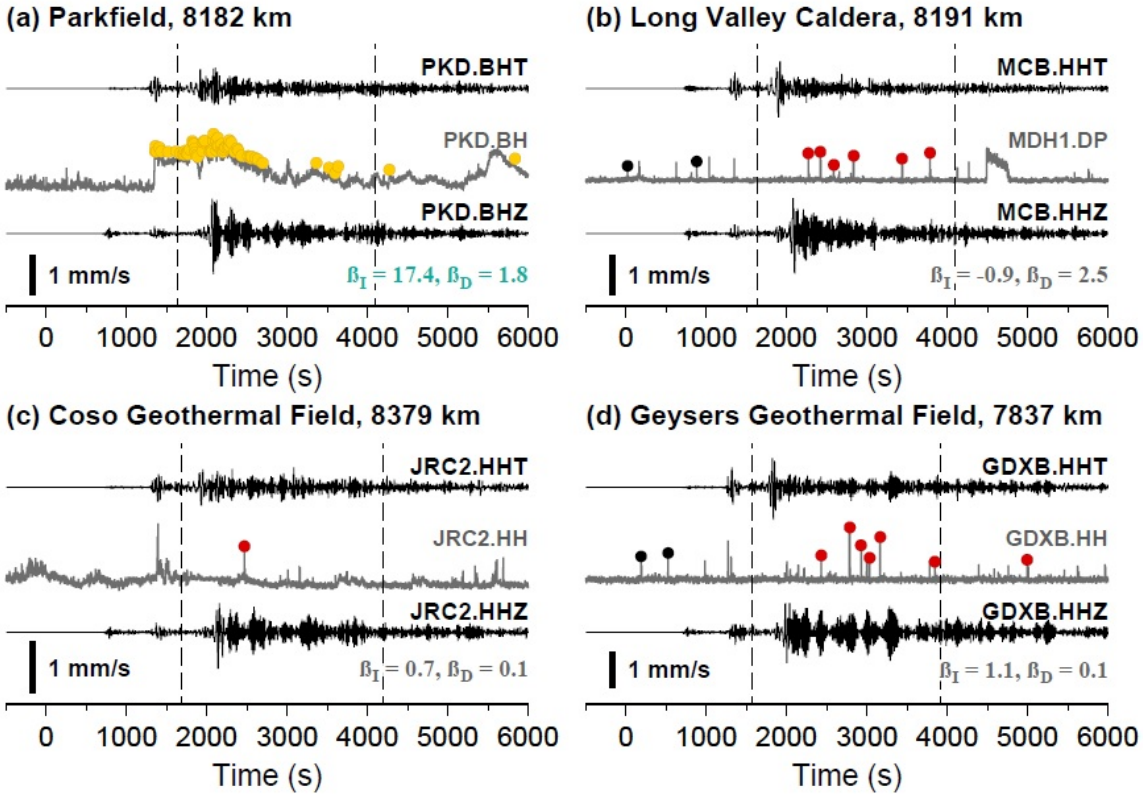

Figure 2.8 - Example of the 2011 *Mw*9.0 Tohoku-Oki earthquake that did not trigger earthquakes in the geothermal regions but did trigger tremor in Parkfield, CA. In each panel, the broadband transverse, high-passed > 5 Hz filtered envelope, and broadband vertical waveforms are plotted. Yellow circles = detected LFEs; Red circles = hand-picked microearthquakes. Vertical bar in each panel indicates the amplitude for broadband data. Instantaneous and delayed β-values are indicated. β-statistics in turquoise are considered statistically significant (i.e. triggers); β-statistics in gray are considered non-triggers.

2.5 Characteristics of Triggered Activity

As mentioned before, for earthquakes that appeared to trigger microearthquakes in the geothermal/volcanic regions, we hand-picked local earthquakes 5 hours before and after the *P*-wave arrival. In addition to using them for the β-statistic calculations, we examined the temporal evolution of local seismicity patterns in these regions before and after the distant earthquakes (Figure 2.9). Figure 2.9a shows that the seismicity rate in Long Valley after the *P*-wave arrival of the 2010 Baja California earthquake is greater than the background seismicity rate. Similarly, Figure 2.9b depicts a seismicity rate greater than the background rate in Geysers following the 2001 Peru earthquake. The 2010 Baja California earthquake occurred 1,100 km (~28 fault lengths) away from Long Valley, while the 2001 Peru earthquake occurred ~8,000 km (~50 fault lengths) away from Geysers. Thus, the wavetrain of the Baja California earthquake is much shorter in duration and triggering occurs closer to its origin time, as compared to the 2001 Peru earthquake. However, the seismicity rate in Long Valley remains above the background level for at least 4000 s following the 2010 Baja California event, long after the passage of the large-amplitude surface waves. On the other hand, local earthquakes in Geysers were mostly triggered by the Rayleigh wave of the 2001 Peru earthquake, outlined in the box of Figure 2.9b (see also Figure 2.6). As such, the seismicity rate clearly returns to the background level immediately after the passage of large-amplitude surface waves (Figure 2.9b).

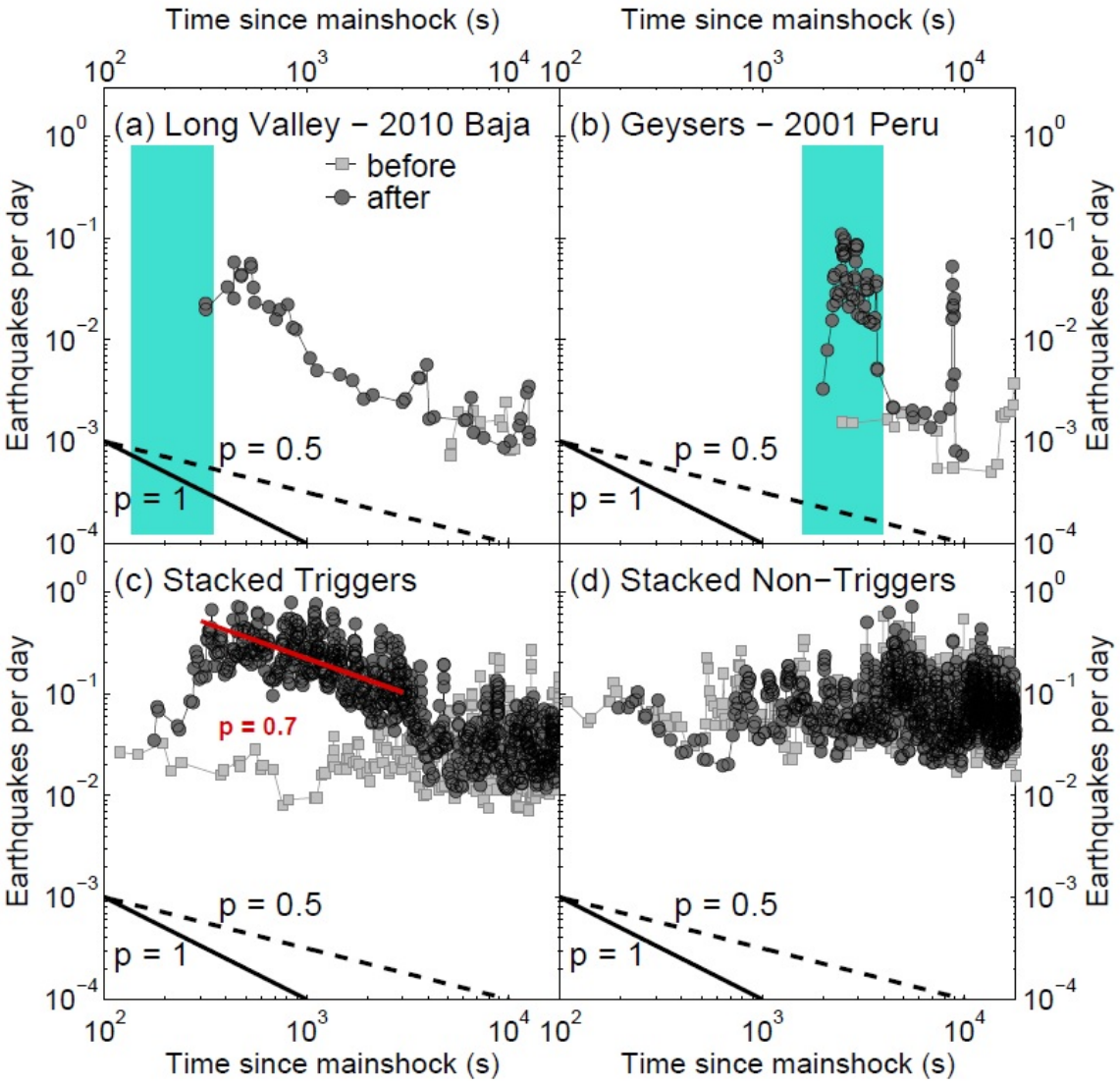

Figure 2.9 - Triggered seismicity rates. Gray squares = seismicity rates prior to the P-wave arrival; Black circles = seismicity rates after. Thick solid and dashed lines are Omori's law decay rate p = 1 and 0.5, respectively. In (a) and (b), waves traveling between 5 km s^{-1} to 2 km s^{-1} arrive in the time window marked with the turquoise background (see Section 2.6). **(a)** Triggering example of the 2010 Baja California earthquake in Long Valley and **(b)** 2001 Peru earthquake in Geysers. **(c)** Stacked hand-picked local earthquake catalogs for all triggering cases. Red line = Omori's law decay rate for p = 0.7. **(d)** Stacked hand-picked local earthquake catalogs for all non-triggering cases.

To further investigate the overall temporal behavior of seismicity rates following the many triggering and non-triggering earthquakes we identified, we stacked all the triggered and non-triggered sequences, separately (Figure 2.9c-d). We found that the

stacked triggered seismicity rate follows an apparent Omori law decay with a decay constant p = 0.7 (Figure 2.9c). The seismicity rate returned to the background level at ~3000 s after the *P* wave arrivals. Not surprisingly, we did not observe any changes in the seismicity rate for the non-triggering cases (Figure 2.9d).

Lastly, we compared the average number of events (microearthquakes and LFEs) occurring before the *P*-wave of triggering mainshocks, as well as during the instantaneous triggering and delayed triggering windows. We summed the number of events in these windows and divided by the number of triggering earthquakes in that region to normalize the results (Figure 2.10). In each geothermal/volcanic region, the number of earthquakes occurring after the wavetrain exceeded that of events triggered during the wavetrain for our study period. In particular, Long Valley and Coso can trigger ~4 times as many microearthquakes after the surface waves than those triggered directly, and both regions appear to instantaneously trigger the same number of earthquakes on average. Prior to a mainshock, more microearthquakes and tremor on average appear to occur in Geysers and Parkfield, respectively, and both regions appear to instantaneously trigger three times as many as the other two regions. Moreover, the ratio between delayed and instantaneously triggered events in Parkfield and Geysers is approximately half that of Long Valley and Coso.

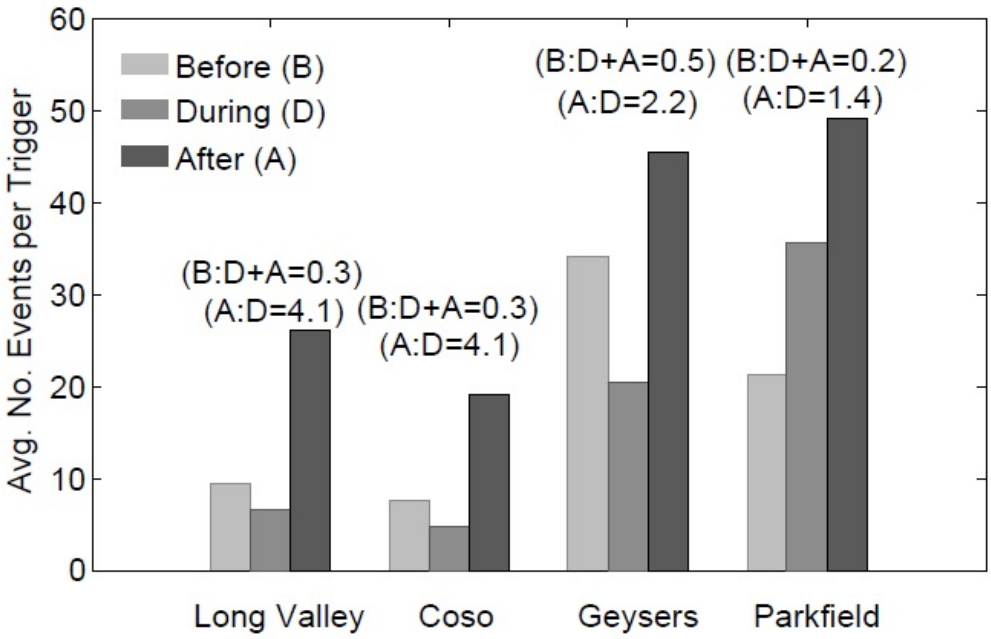

Figure 2.10 - Average number of events occurring before, during, and after the surface waves per triggering earthquake by region. The number in parentheses indicates how many more earthquakes on average occurred after the wavetrain as compared to during the wavetrain. Delayed triggering is more pronounced in Long Valley and Coso, while more events on average are triggered instantaneously in Geysers and Parkfield.

2.6 Characteristics of Triggering Waves

Under the assumption that faults are critically stressed, we examined the PGVs of our triggering earthquakes to determine a stress threshold for microearthquake triggering, similar to previous studies of dynamically triggered earthquakes [e.g., *Brodsky and Prejean*, 2005]. In addition, we examined the PGVs of distant earthquakes that triggered deep tectonic tremor along the Parkfield-Cholame segment of the SAF in Central California to better understand the differences in the mechanisms responsible for microearthquake and tremor triggering.

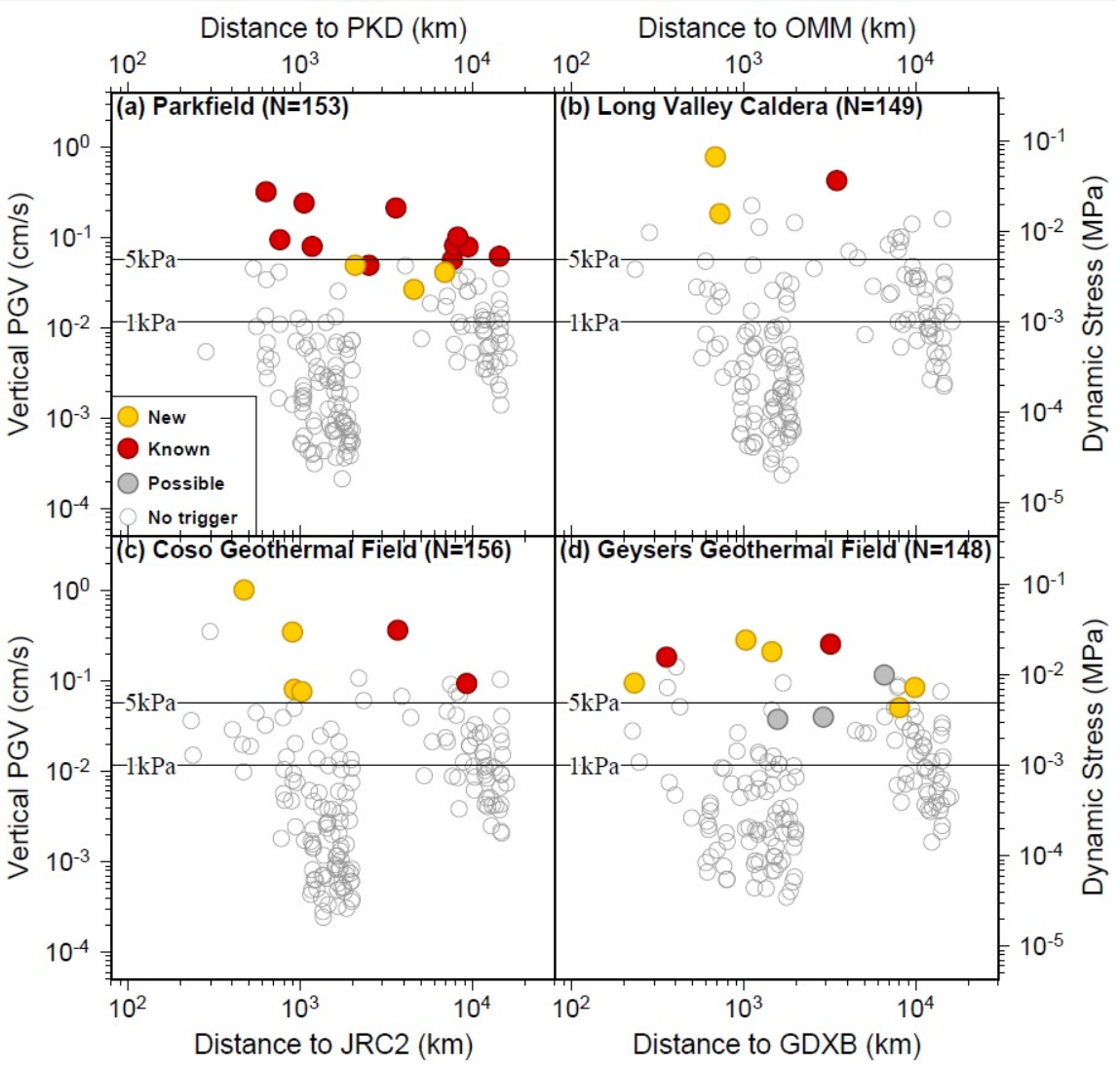

Figure 2.11 – Vertical PGV and dynamic stress versus epicentral distance for 4 regions of California. Yellow circles = triggering earthquakes identified in this study, red circles = triggering events reported in previous studies, gray circles = possible triggering events, and open circles = non-triggering events. PGVs were measured at from the vertical components of station(s) PKD for Parkfield, OMM/MCB/MDPB for Long Valley, JRC/JRC2 for Coso, and HOPS/GDXB for Geysers, such that secondary stations were used when seismic data from the primary station was not available. PGVs shown are measured from low-passed 1-s waveforms (see Figure 1). For transverse PGVs, see Figure S2.7. The dynamic stress is estimated using a shear rigidity of 30 GPa and a phase velocity of 3.5 km s^{-1}. **(a)** Parkfield, **(b)** Long Valley, **(c)** Coso, and **(d)** Geysers. We consider tremor triggered in Parkfield, CA if it has been previously reported or the triggered tremor (1) is coincident with body and/or surface waves, (2) is observable on the PKD station, and (3) is statistically significant (see Section 6). We only observed ambiguous cases of triggering in Geysers.

Figures 2.11 and S2.7 show the PGVs and dynamic stresses measured at Parkfield, as well as Long Valley, Coso, and Geysers for the vertical and transverse components, respectively. Following *Brodsky and Prejean* [2005], we also applied a 30-s low-pass filter to the waveforms, and re-measured these parameters (Figures S2.8 and S2.9). We found that the two newly identified distant events (2005 Mendocino and 2010 Baja California earthquakes) that triggered microearthquakes in Long Valley also produced at least 5 kPa of dynamic stress (when low-passed 30-s), similar to observations of *Brodsky and Prejean* [2005]. However, we observed triggering in Coso and Geysers by distant earthquakes generating as low as ~1 kPa of vertical dynamic stress (when low-passed at 30-s). The Parkfield segment also requires less dynamic stress (~1 kPa) to trigger tremors compared to the stress (> 5 kPa) needed to trigger microearthquakes in Long Valley. In addition, there are a number of earthquakes that generate dynamic stresses above 1 kPa that do not trigger microearthquakes in Long Valley, Coso, or Geysers, 94%, ~74%, and ~67% of earthquakes with vertical dynamic stress > 1 kPa, respectively (when low-passed 30-s). For this reason, we also examined the surface wave amplitude spectra generated by all distant earthquakes we examined (Tables S2.1-S2.4). Following *Peng et al.* [2009], we computed the arrival times of the 5 km s^{-1} and 2 km s^{-1} wave arrivals, cut the transverse and vertical velocity instrument-corrected data between these times, integrated the data to obtain displacement, and then computed the fast-Fourier transform (FFT). Finally, we smoothed the amplitude spectra with a sliding window of 5 points [*Peng et al.*, 2009]. As shown in Figures S2.10 and S2.11, most earthquakes with large, long-period amplitude spectra triggered microearthquakes in Long Valley, Coso, and Geysers. However, there are a few cases where non-triggering

earthquakes generated amplitude spectra similar to earthquakes that triggered microearthquakes in the three geothermal/volcanic regions studied here. Thus, while long-period shaking (>10s) can cause triggering in the three geothermal/volcanic regions, there is no clear dominant period solely responsible for triggering microearthquakes.

2.7 Discussion and Conclusions

In this study [*Aiken and Peng*, 2014], we provided evidence of long-term microearthquake triggering in three geothermal regions of California – Long Valley Caldera, Coso Geothermal Field, and Geysers Geothermal Field. We examined 148-156 earthquakes in each geothermal region and found that 2.0%, 3.8% and 6.8% of our distant earthquakes triggered microearthquakes in these regions, respectively. These percentages are mainly based on the β-statistic. However, as a secondary test, we applied the Z-statistic [e.g. *Aron and Hardebeck*, 2009]. While 1-2 sequences are different, the overall percentage of triggering in each region is similar to those when using the β-statistic (Table S2.6). We also verified the robustness of our findings over a longer time window (± 5 days) using a combined ANSS recorded catalog with our hand-picked events for several events (Figure S2.12) and confirmed that the triggering for these sequences are statistically significant.

In total, we identified 10 unique, distant earthquakes that triggered microearthquakes in Long Valley, Coso, and/or Geysers (Table 2.1). Among them, the 3 November 2002 *M*7.9 Denali, 15 June 2005 *M*7.2 Mendocino, and 4 April 2010 *M*7.2 Baja earthquakes triggered small magnitude (< *M*2) earthquakes in all three regions, in addition to triggering tremor on Parkfield-Cholame section of the SAF. Furthermore, most microearthquakes triggered in the three geothermal/volcanic regions were not

detected by automated earthquake catalogs (e.g., ANSS) likely due to their low amplitudes (< *M*2). Although we did not locate the triggered microearthquakes, we maintain that the microearthquakes occur locally to each region, as we required microearthquakes to have a *S*–*P* time < 10 seconds and to contain high frequencies (e.g., Figure 2.2c.

Table 2.1. Summary of 15 triggering earthquakes [a]

Date (mm/dd/yyyy)	Origin Time	Magnitude	Parkfield	Geysers	Coso	Long Valley
4/4/2010	22:40:42	7.2	Y (0.321)	Y (0.285)	Y (1.020)	Y (0.782)
8/3/2009	17:59:56	6.9	Y (0.242)	Y (0.210)	Y (0.348)	N (0.227)
11/3/2002	22:12:42	7.9	Y (0.214)	Y (0.256)	Y (0.365)	Y (0.428)
3/11/2011	5:46:24	9.1	Y (0.102)	N (0.085)	N (0.070)	N (0.102)
6/15/2005	2:50:54	7.2	Y (0.095)	Y (0.184)	Y (0.081)	Y (0.183)
9/29/2009	17:48:11	8.1	Y (0.082)	N (0.089)	N (0.075)	N (0.090)
1/4/2006	8:32:32	6.6	Y (0.080)	Y (0.038)	Y (0.077)	N (0.130)
2/27/2010	6:34:12	8.8	Y (0.079)	Y (0.085)	Y (0.094)	N (0.141)
12/26/2004	0:58:53	9	Y (0.063)	N (0.076)	N (0.104)	N (0.160)
6/23/2001	20:33:14	8.4	Y (0.057)	Y (0.051)	N (0.092)	N (0.099)
1/22/2003	2:06:35	7.6	Y (0.050)	Y (0.040)	N (0.061)	N (0.046)
10/28/2012	3:04:09	7.8	Y (0.049)	N (0.095)	N (0.108)	N (0.146)
1/13/2007	4:23:21	8.1	Y (0.042)	Y (0.117)	N (0.046)	N (0.084)
1/10/2010	0:27:39	6.5	Y (0.035)	Y (0.095)	N (0.039)	N (0.055)
9/5/2012	14:42:08	7.6	Y (0.027)	N (0.026)	N (0.040)	N (0.059)

[a] Y = trigger; N = not a trigger; PGVs (low-passed at 1-s) in parentheses beneath Y or N.

Previous studies have suggested that dynamic triggering of earthquakes and tremors may be dependent upon amplitude and frequency of incident surface waves [e.g. *Brodsky and Prejean*, 2005; *Peng et al.*, 2009]. In our study, the 2002 Denali, 2005 Mendocino, and 2010 Baja earthquakes generated over 10 kPa of dynamic stress in each of the 4 regions where we observed triggered phenomena. Specifically, we found that Long Valley required a slightly higher dynamic stress for microearthquake triggering than Coso and Geysers, i.e. ~5 kPa and ~1 kPa respectively when low-pass filtered 30-s (Figures S2.8-S2.9). Similar to Coso and Geysers, Parkfield tremors can be triggered by dynamic stresses as little as ~1 kPa, even though triggering in Parkfield is more abundant than in Coso and Geysers.

We note that some earthquakes that generated large dynamic stresses triggered tremors in Parkfield but did not trigger microearthquakes in Long Valley, Coso, or Geysers (Table 2.1). For example, the 26 December 2004 *M*9.0 Sumatra earthquake is one of the largest earthquakes to have occurred in the past decade. Yet, the 2004 Sumatra earthquake did not trigger microearthquakes in any of the geothermal/volcanic regions of California we examined, even though increased earthquake activity had been observed in an active geothermal region of Alaska following the same event [*West et al.*, 2005]. One possible explanation is that the geothermal/volcanic regions can experience prominent earthquake activity prior to the arrival of large amplitude surface waves, resulting in the loss of accumulated stress and the near-critical state needed for triggering to occur (Figure S2.13). This could be the case for Coso, where a swarm-like sequence occurred

about 3 hours before the Sumatra mainshock, but we did not see any obvious increase of seismic activity right before the mainshock in the other two geothermal/volcanic regions.

Previous studies have also suggested that microearthquake triggering may occur after surface waves have already passed either by aftershock decay [*Brodsky*, 2006] or by multiple surface waves circling the earth [*Peng et al.*, 2011]. While we did not observe any additional triggering by multiple surface waves circling the earth in this study, we did find that triggered microearthquakes can occur both swarm-like when examining triggered sequences individually and as Omori law decay ($p=1$) when considering all triggered sequences (Figure 2.9). However, the Omori law decay we observed could be affected by the stacking of the triggered catalogs. That is to say, that the time period over which surface waves pass in these regions varies based on each earthquake's epicentral distance, and therefore triggered microearthquakes can occur over a wide period of time. In addition, we only observed 8 cases where microearthquakes or tremor were delay triggered in total over all regions (Table S2.5-S2.6). In particular, the 2010 Baja earthquake was the only event to sustain seismicity long after the surfaces waves in all three geothermal regions, as captured by our β-statistic analysis. Moreover, delayed triggering appears to be more prominent in Long Valley and Coso where triggering occurs less frequently (e.g., Figure 2.10).

Hill and Prejean [2014] suggested that areas of elevated background seismicity are more susceptible to dynamic triggering. One distinct feature that could explain the subtle differences in triggering responses in the three geothermal/volcanic regions studied here is their background seismicity rates. To examine this further, we selected all earthquakes between 2000 and 2012 from the ANSS catalog for each study region and

computed the Gutenberg-Richter frequency-size relationship, after normalizing by the area of each region (Figure 2.12). While their *b*-values are somewhat similar, their *a*-values (or inferred total number of events at magnitude 0) vary and appear to coincide with the quantity of triggers identified in each region. That is to say, the Geysers responded more to passing seismic waves and has the highest background seismicity rate. Moreover, Geysers and Coso appears to have higher heat flow than Long Valley (Figure S2.14), and Geysers is home to the world's largest geothermal power plant with the installed capacity of ~2000 MW, while the installed capacities at Coso and Mammoth near Long Valley are 270 MW and 40 MW, respectively [*Bertani*, 2012]. A higher power production would help to promote steam/fluid circulation in the shallow crust and hence result in higher background seismic activity and greater triggerability.

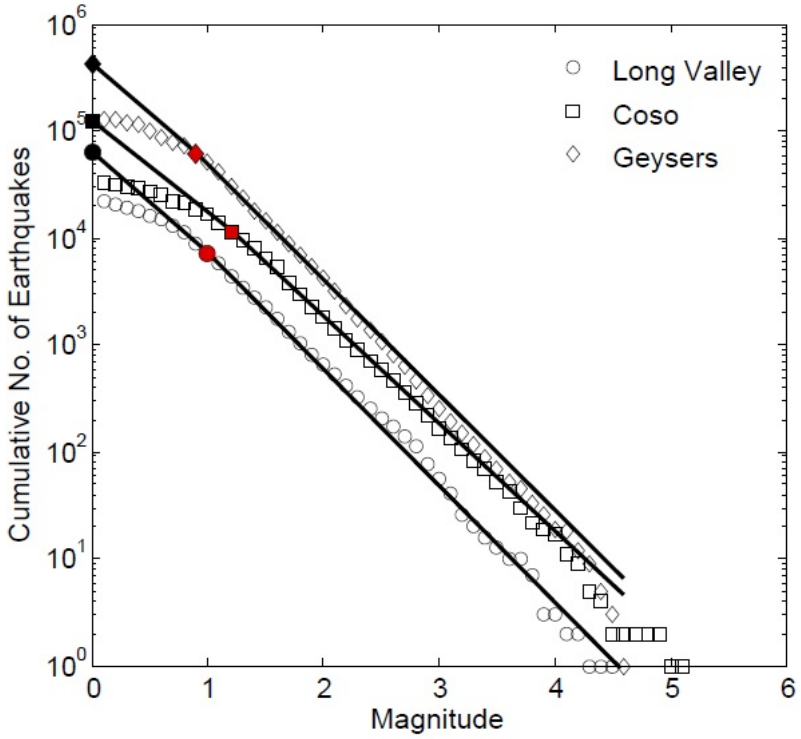

Figure 2.12 – Gutenberg-Richter relationship for Long Valley, Coso, and Geysers. Cumulative number of events as a function of magnitude was computing using events listed in the ANSS catalog between 2000 and 2012. Symbol shape = region. Red symbols = magnitude of completeness, which was determined using the entire magnitude range (EMR) method in ZMAP [*Woesnner and Wiemer*, 2005; *Wiemer*, 2001]. Black symbols = the *a*-values for each region. Solid lines are *b*-values. While each region has a somewhat similar *b*-value, their background seismicity rates (*a*-values) vary.

When comparing the three geothermal/volcanic regions with the Parkfield-Cholame section of the SAF, it appears that distant earthquakes trigger tremor more often than microearthquakes. However, there is a wide range of variability on how tremor is triggered in other regions. For example, many tremor episodes have been found in Southwest Japan [*Miyazawa et al.*, 2008; *Enescu et al.*, 2013; *Chao and Obara*, 2012], Vancouver Island [*Rubinstein et al.*, 2007, 2009], southern Taiwan [*Chao et al.*, 2012b], and other transpressional tectonic settings [e.g., *Aiken et al.,* 2013b; *Peng et al.*, 2013].

The inferred tremor triggering threshold is roughly on the range of 1-10 kPa. On the other hand, a few recent studies found that the 2002 Mw7.9 Denali Fault earthquake is the only distant even associated with clearly triggered tremor at the San Jacinto and the Calaveras faults, as well as in Simi Valley [*Chao et al.*, 2012a; *Wang et al.*, 2013; *Yang and Peng*, 2013].

One may also suspect that we observed more triggering cases in Parkfield since we used a waveform based LFE catalog resulting in more local event detections, while in the geothermal/volcanic regions we only hand-picked local events from nearby stations. In addition, one may consider that the correlation coefficient (CC) used to detect LFEs could bias the β-values. We argue that this is unlikely for the following reasons. First, the average number of events per trigger appears to be similar (Figure 2.10), at least for Parkfield and Geysers. In addition, the matched filter technique used to detect LFEs is applied to the entire study period (2001-now), rather than focusing specifically during the time period immediately during/after large distant earthquakes, i.e. ± 5 hours with respect to an earthquake's *P*-wave arrival. The matched filter technique also requires a correlation sum across the entire high-resolution seismic network ≥ 4.0 and mean CC value of 0.16 [e.g., *Shelly and Hardebeck,* 2010]. To test the effect of the detection CC on β-values, we also computed β-values for all possible correlation coefficients as a threshold (Figure S2.15) and found that only 1-2 sequences have β≤ 2 when the correlation coefficient is greater than the 1 times the median absolution deviation (MAD) for the entire time period (2001-2012). Hence, there is no bias towards detecting more events during teleseismic surface waves. Finally, we also visually inspected the waveforms at the broadband station PKD at Parkfield, a station similar to ones we used

for observations in the three geothermal/volcanic regions. Even though we did not use the high-resolution seismic network at Parkfield, we easily identified triggered tremor at PKD for several cases (e.g., Figures 2.8 and S2.6). Hence, while we cannot completely rule out its effect, we can say that the observed differences in the tremor and microearthquake triggering behavior are not purely caused by the differences in seismic network and processing techniques.

Crustal fluids also play a role in triggering threshold. *Bartlow et al.* [2012] conducted a laboratory test of triggered stick-slip events by oscillatory loading in the presence of pore fluid. They found that with increasing pore fluid pressures (and hence smaller effective stress), the correlation between stick-slip and oscillatory loading is significantly increased. Their results suggested an apparent higher triggering threshold for microearthquakes than tremor, which is qualitatively consistent with our observation. While it is impossible to directly measure fluid pressure at depth, various geophysical methods have found very high V*p*/V*s* ratio, high attenuations and/or high conductivity in the lower crust near the tremor source regions [*Shelly et al.*, 2006; *Fry et al.*, 2011; *Becken et al.*, 2011], suggesting the existence of near-lithostatic fluid pressure. Hence, we would expect to see a lower triggering threshold for tremor due to the elevated fluid pressure. In contrast, fluid pressure in the shallow crust of the geothermal/volcanic regions is likely hydrostatic in most areas, which could explain the differences in earthquake and tremor triggering thresholds. This is also in agreement with observations of tidally modulated tremor [*Thomas et al.*, 2012], while microearthquakes are only weakly modulated by tides or not at all [*Cochran et al.*, 2004; *Vidale et al.*, 1998].

In summary, Long Valley, Coso, and Geysers respond differently to seismic waves from distant sources. The differences, as observed here, include how frequently the region is triggered, how much dynamic stress is needed to trigger microearthquakes, and even how many microearthquakes can be triggered during and after seismic waves have passed in each region. The frequency of triggering in each region can be best explained by their background seismicity rates. Triggering occurs as a result of varying amplitudes and frequencies, and microearthquake triggering will continue to occur if the conditions are favorable, i.e. seismic waves of large amplitude, distant earthquakes propagating through a seismically productive, geothermal region where faults are critically stressed and fluids are present. However, it remains to be shown whether triggered tremor and geothermal/volcanic regions outside of California exhibit similar characteristics.

2.8 Data and Resources

The Advanced National Seismic System (ANSS) earthquake catalog as well as Northern California Seismic Network waveforms, response files, and station locations are all accessible via the Northern California Earthquake Data Center website (www.ncedc.org, last accessed 11 March 2015). Southern California Seismic Network waveforms, response files, and station locations are accessible via the Southern California Earthquake Data Center website (www.data.scec.org, last accessed 11 March 2015). We used Seismic Analysis Code (SAC) to process all waveform data. The M_c, a, and b values of Figure 2.12 were derived using ZMAP software for MATLAB 2010b, which is openly available at http://www.seismo.ethz.ch/prod/software/zmap/index_EN (last accessed 11 March 2015). Heat flow values in Figure S2.14 were obtained from

http://geomaps.wr.usgs.gov/heatflow/table.htm (last accessed 11 March 2015). All figures were made using either GMT version 4 or MATLAB 2010b. Table 1 was made using Microsoft Excel.

2.9 Supplemental Information

This section contains fifteen figures and links for six tables that are referenced in the previous sections.

2.9.1 Supplemental Figures

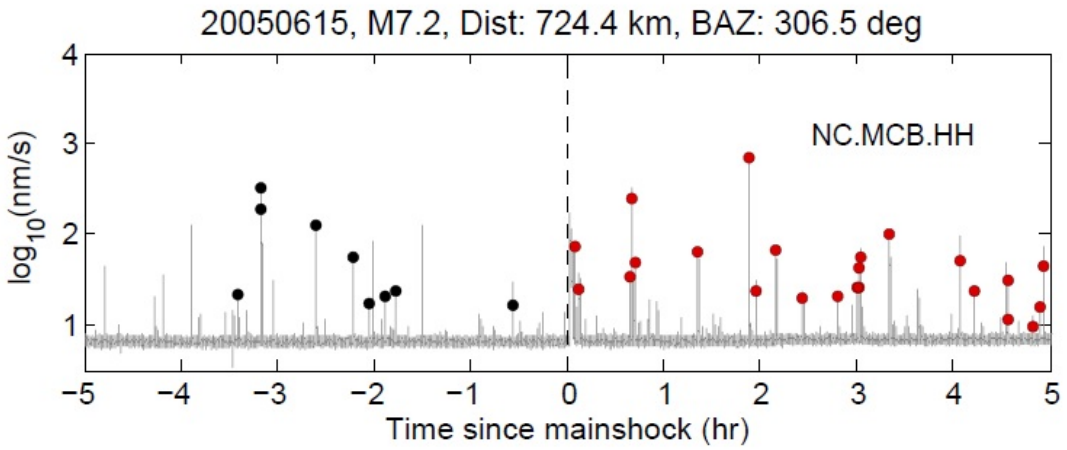

Figure S2.1 - Hand-picked local earthquakes occurring in Long Valley Caldera around the P-wave arrival for the 15 June 2005 *M*7.2 Mendocino earthquake. Symbols and notation are the same as in Figure 2.2b.

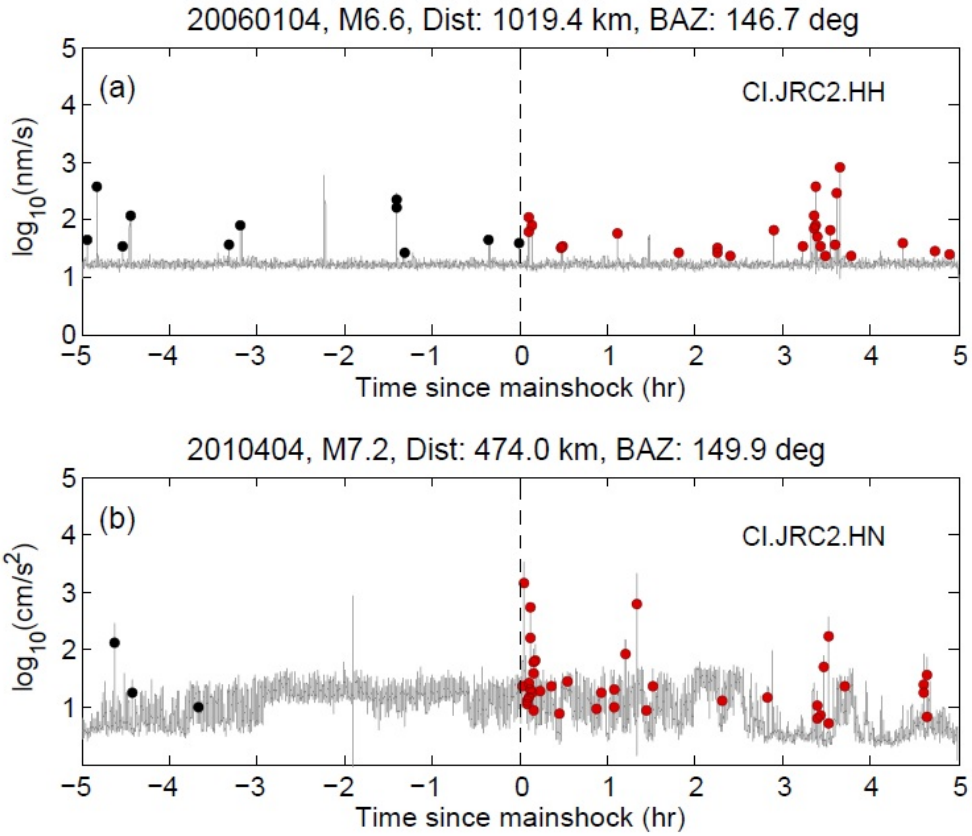

Figure S2.2 - Hand-picked local earthquakes occurring in Coso Geothermal Field around the P-wave arrival of two earthquakes. **(a)** 4 January 2006 *M*6.6 Baja California **(b)** 4 April 2010 *Mw*7.2 Baja California. Symbols and notation are the same as in Figure 2.2b.

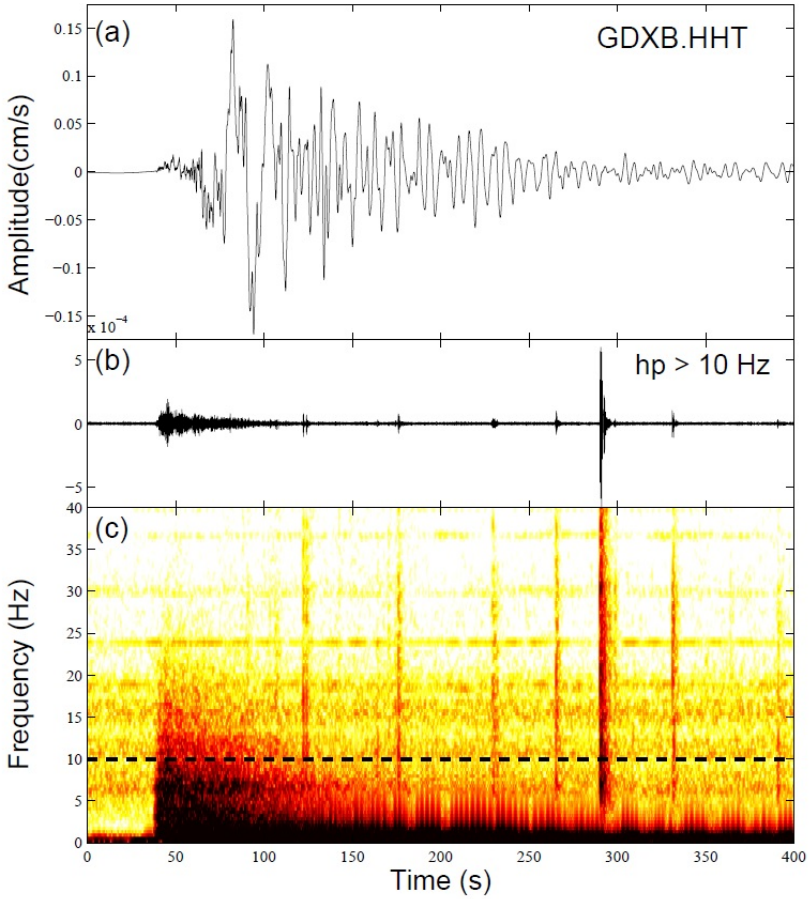

Figure S2.3 - Spectrogram of 10 January 2010 *M*6.5 Northern California earthquake. **(a)** Broadband transverse component recorded at station GDXB. **(b)** High-pass 10 Hz filtered waveform. **(c)** Corresponding spectrogram indicating the 10 Hz high pass filter needed to avoid contaminating body waves.

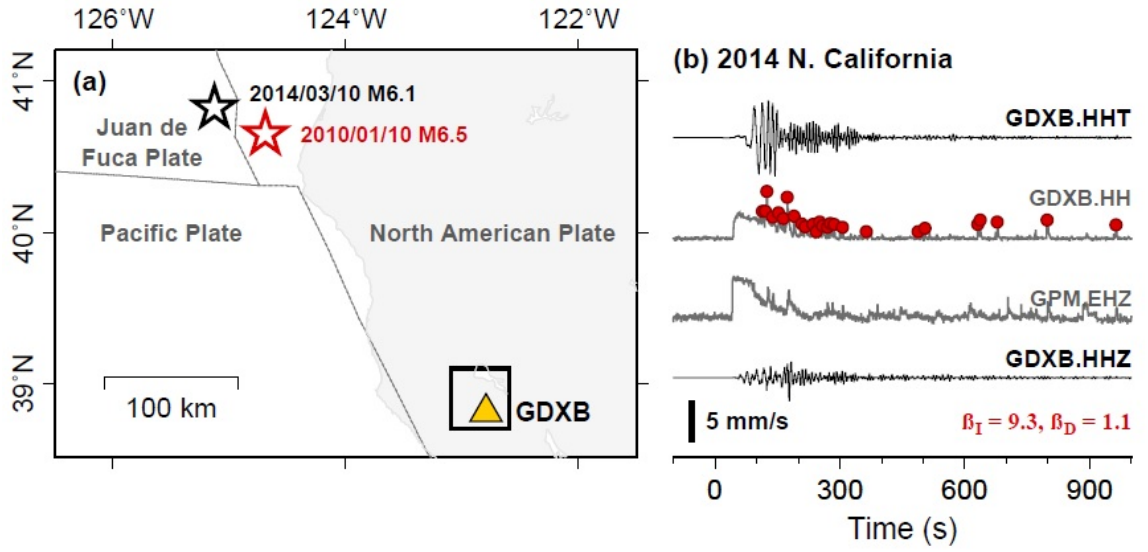

Figure S2.4 - Recent example of earthquakes triggered in Geysers by a second moderate-size earthquake occurring off the shore of Northern California. **(a)** Map indicating the Geysers study region (black box) and location of the 10 January 2010 *M*6.5 and 10 March 2014 *M*6.1 Northern California earthquakes. Plate boundaries are in light gray. **(b)** Broadband transverse, high-passed > 5 Hz filtered envelopes, and broadband vertical waveforms are plotted. Red circles = hand-picked earthquakes. Vertical bar = amplitude of broadband waveforms. β-values are indicated.

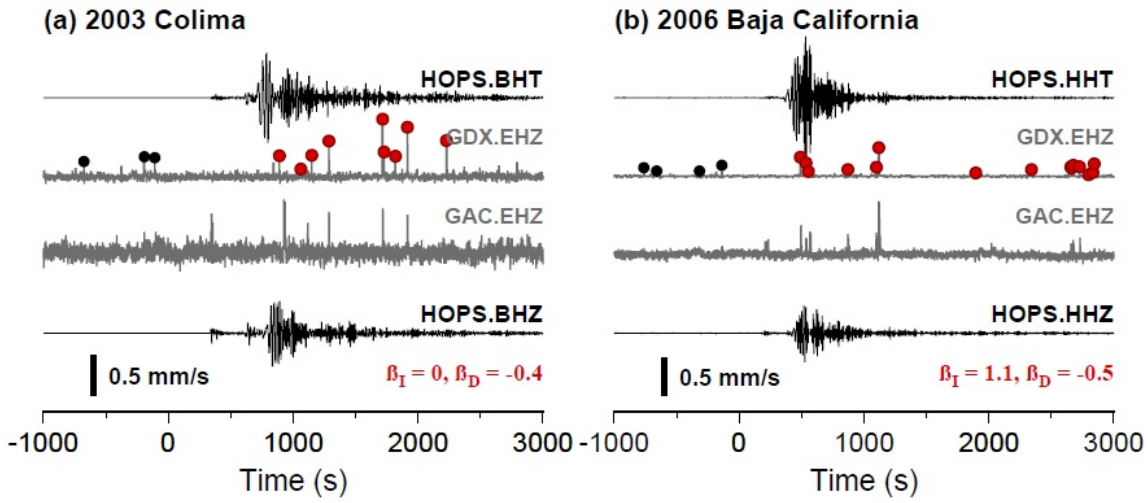

Figure S2.5 - Local earthquakes possibly triggered in Geysers Geothermal Field by the 22 January 2003 *M*7.6 and 4 January 2006 *M*6.6 Baja California earthquakes. Symbols and notation are the same as in Figure 2.3.

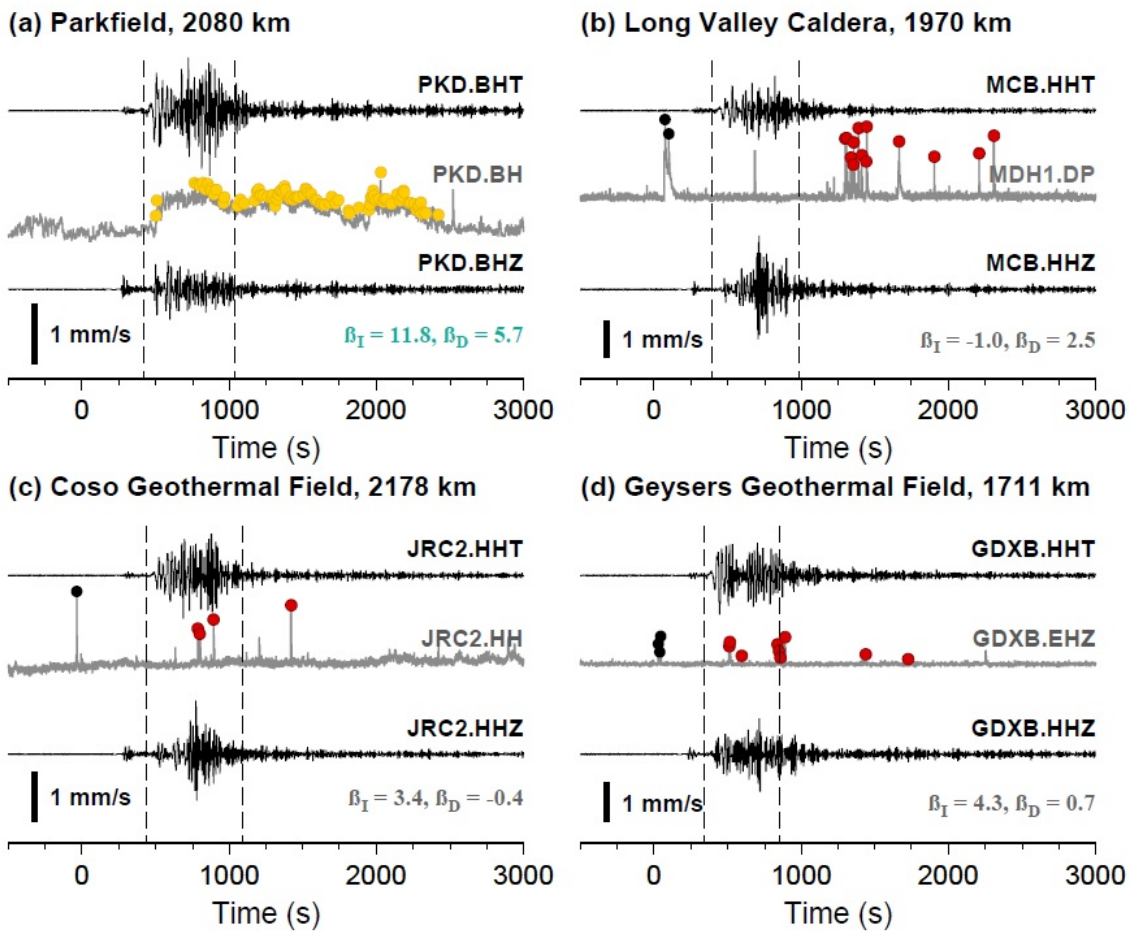

Figure S2.6 - Example of the 28 October 2012 *Mw*7.7 Haida Gwaii earthquake that did not trigger earthquakes in the geothermal regions but did trigger tremor in Parkfield, CA. Symbols and notation same as in Figure 2.8.

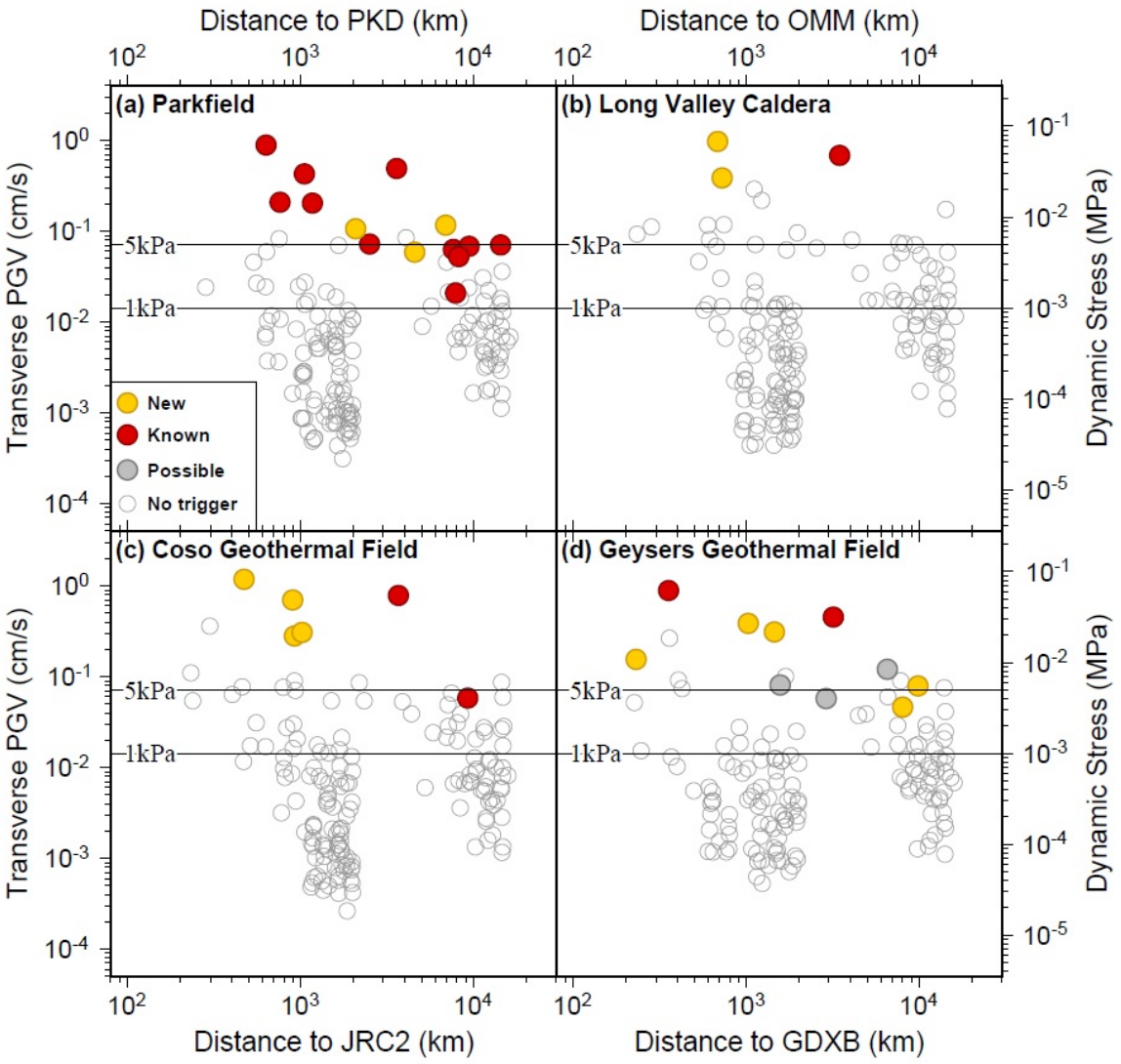

Figure S2.7 - Transverse PGV and dynamic stress versus epicentral distance for 4 regions of California. Symbols and notation are the same as in Figure 2.11. PGVs shown are measured from low-passed 1-s waveforms. The dynamic stress is estimated using a shear rigidity of 30 GPa and a phase velocity of 4.1 km s^{-1}. **(a)** Parkfield, **(b)** Long Valley, **(c)** Coso, and **(d)** Geysers.

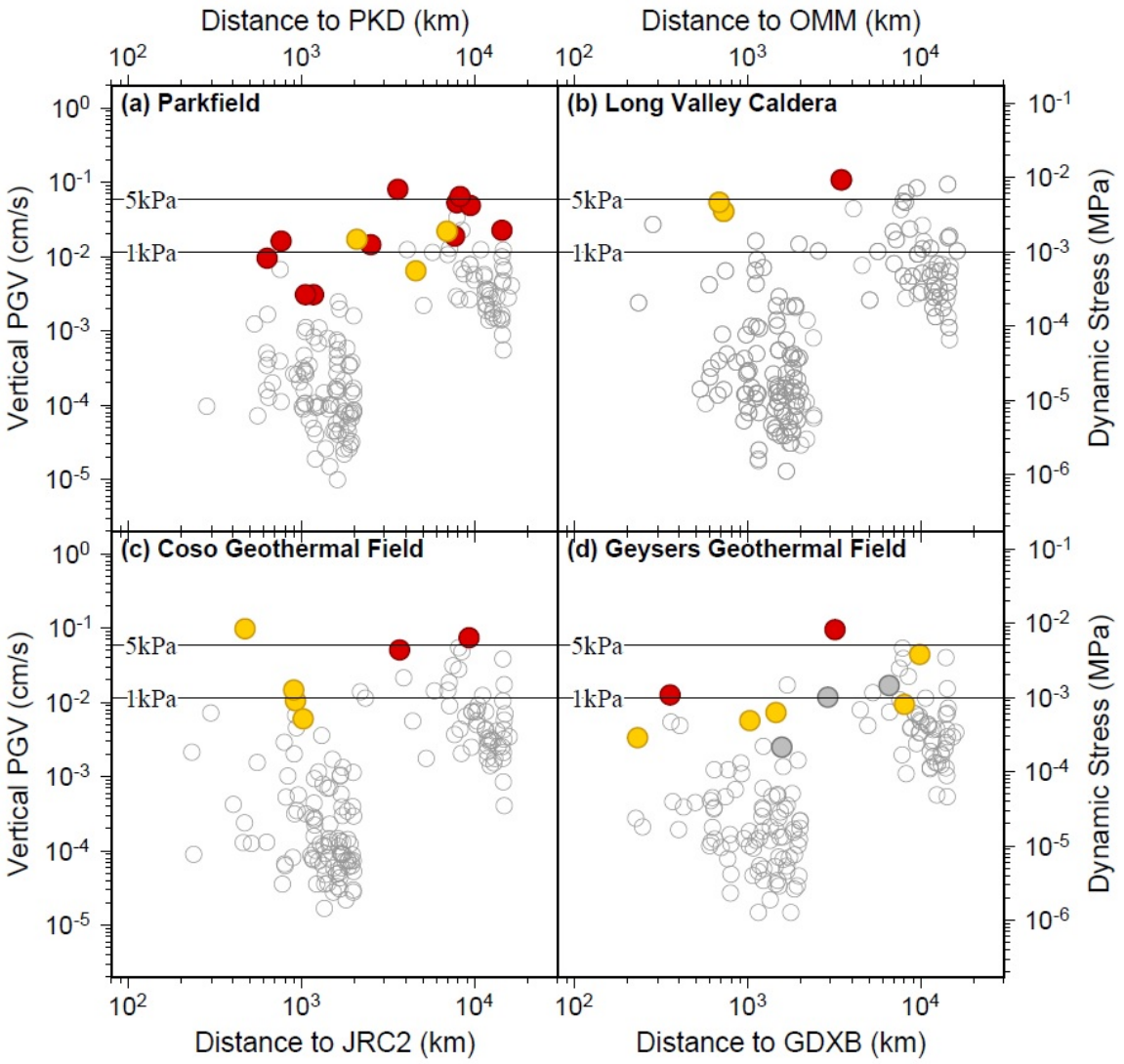

Figure S2.8 - Vertical PGV and dynamic stress versus epicentral distance for 4 regions of California. Symbols and notation are the same as in Figure 2.11. PGVs shown are measured from low-passed 30-s waveforms. The dynamic stress is estimated using a shear rigidity of 30 GPa and a phase velocity of 3.5 km s^{-1}. **(a)** Parkfield, **(b)** Long Valley, **(c)** Coso, and **(d)** Geysers.

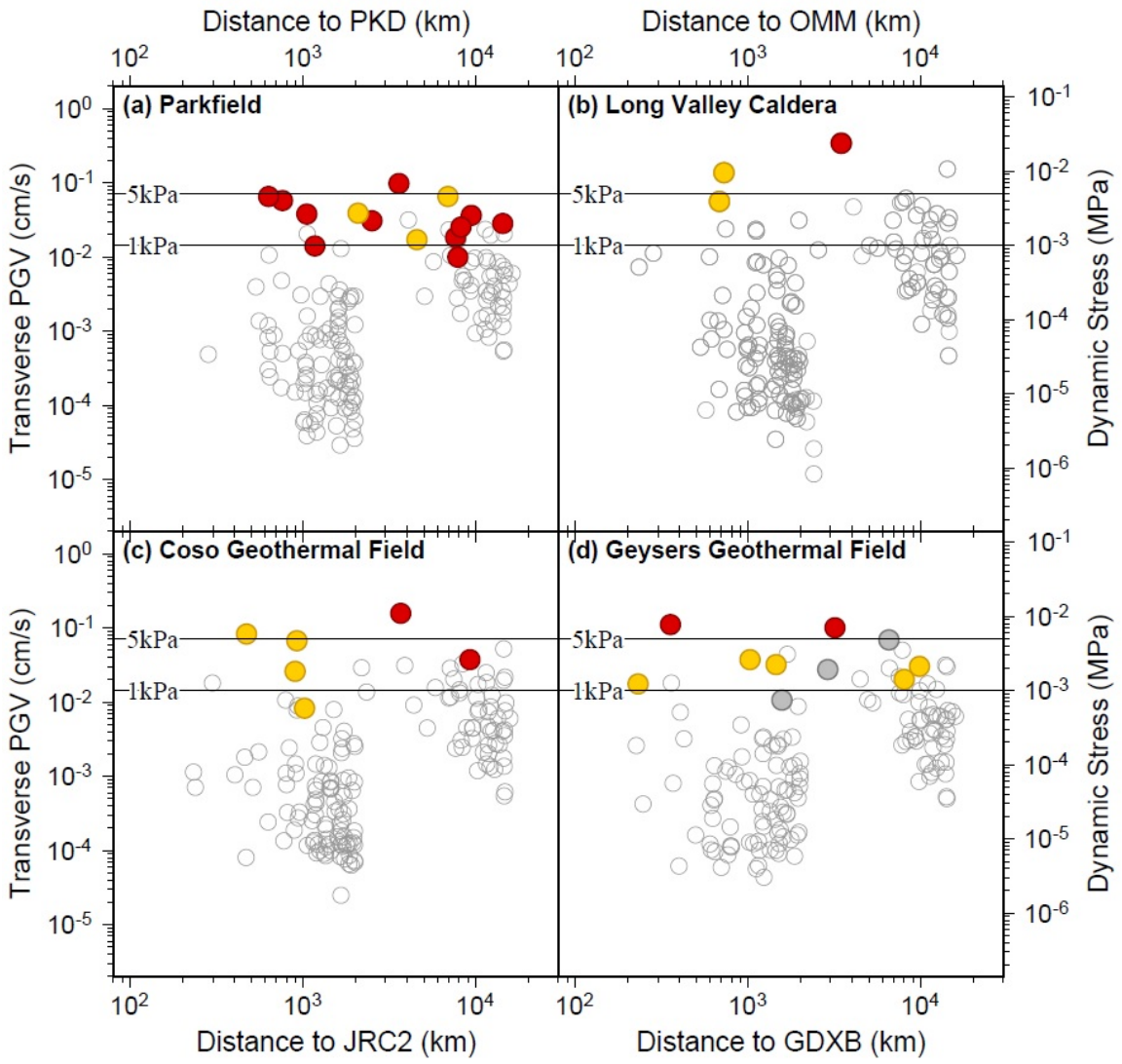

Figure S2.9 - Transverse PGV and dynamic stress versus epicentral distance for 4 regions of California. Symbols are the same as in Figure 2.11. PGVs shown are measured from low-passed 30-s waveforms. The dynamic stress is estimated using a shear rigidity of 30 GPa and a phase velocity of 4.1 km s^{-1}. **(a)** Parkfield, **(b)** Long Valley, **(c)** Coso , and **(d)** Geysers.

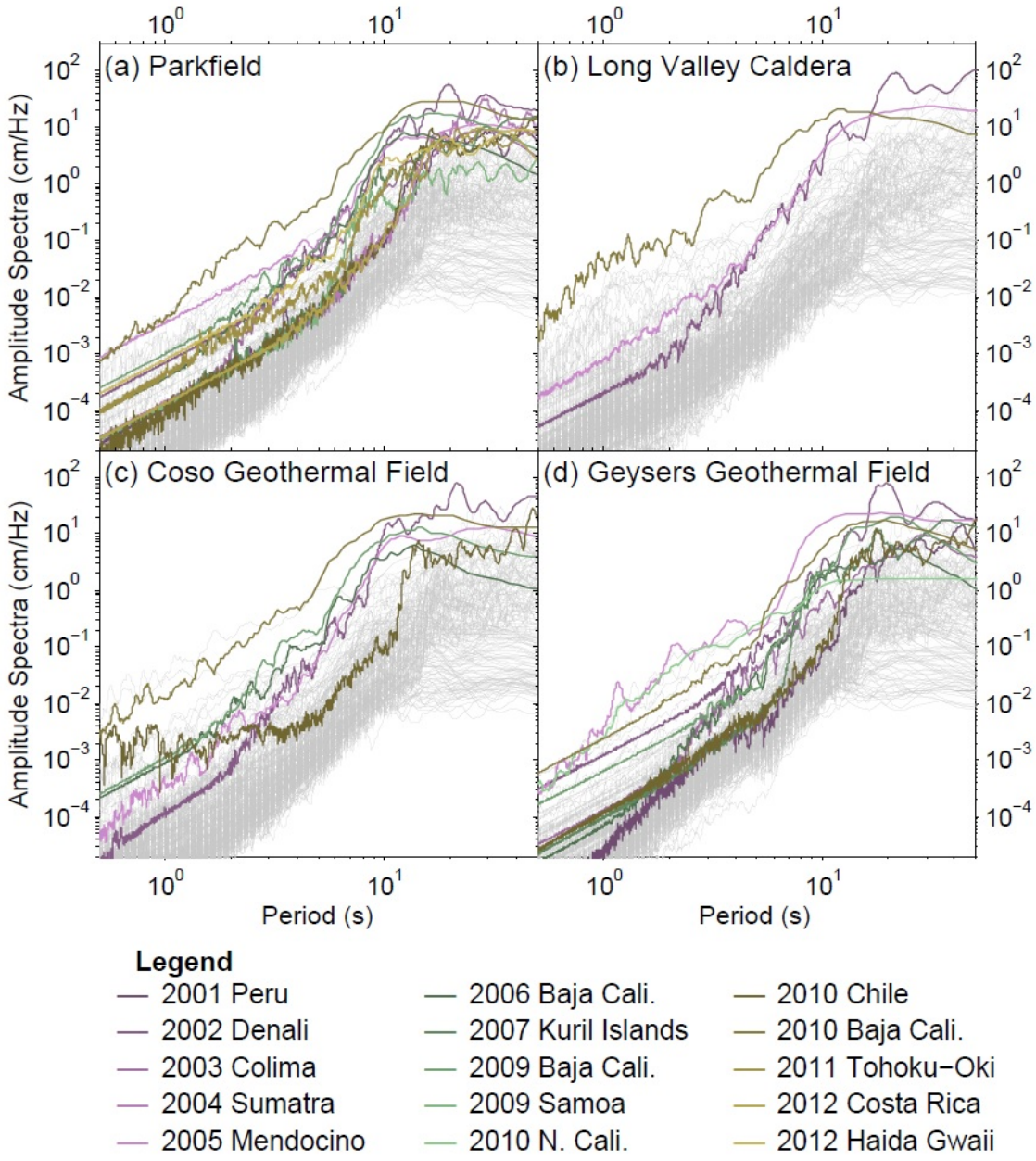

Figure S2.10 - Surface wave spectra of instrument-corrected transverse displacement waveforms for 4 regions of California. Colored lines = triggering and possible triggering earthquakes. Gray lines = non-triggering events. **(a)** Parkfield, **(b)** Long Valley, **(c)** Coso, **(d)** Geysers.

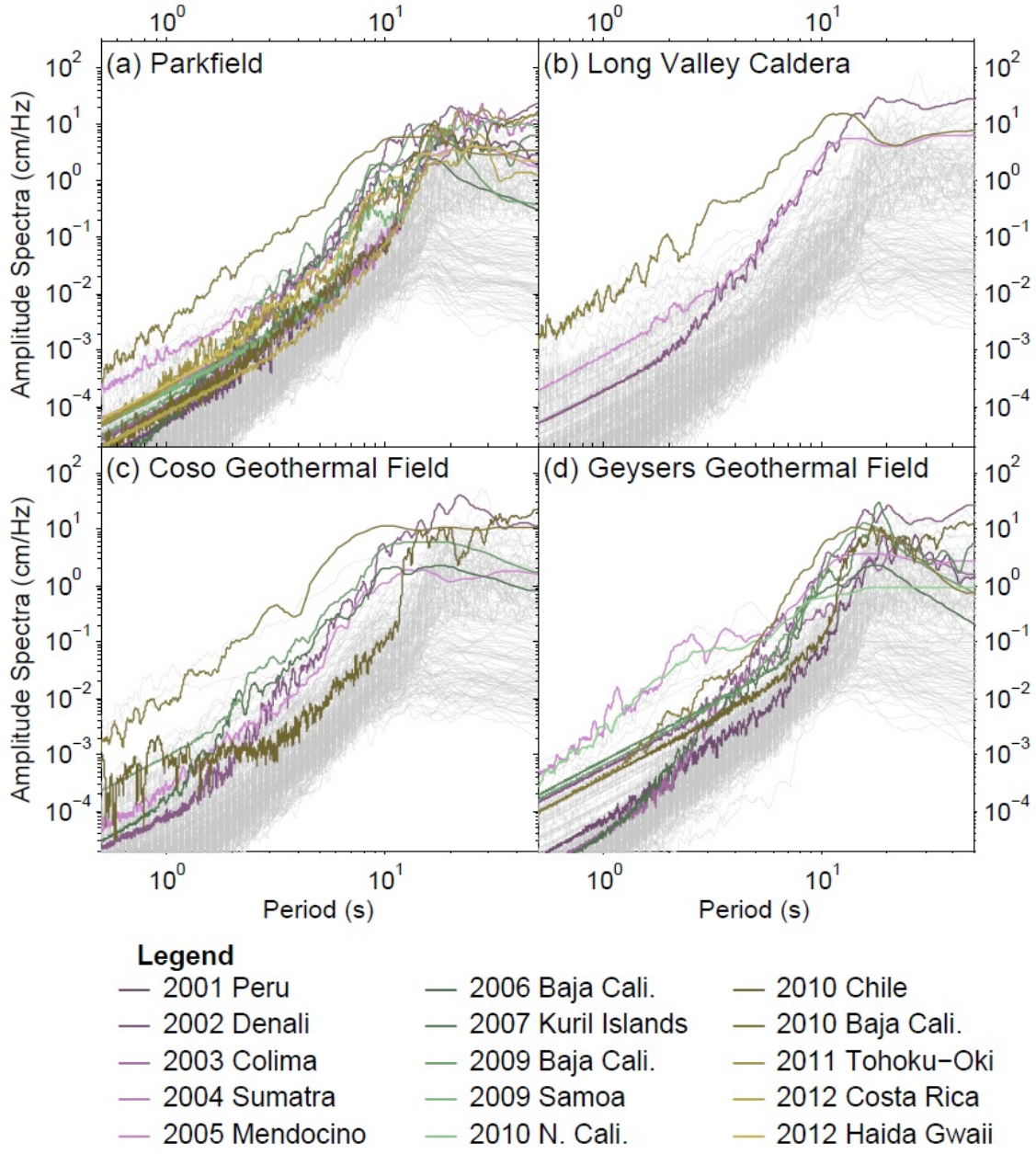

Figure S2.11 - Spectra of selected vertical displacement seismograms for 4 regions of California. Symbols and notation are the same as in Figure S2.10. **(a)** Parkfield, **(b)** Long Valley, **(c)** Coso, **(d)** Geysers.

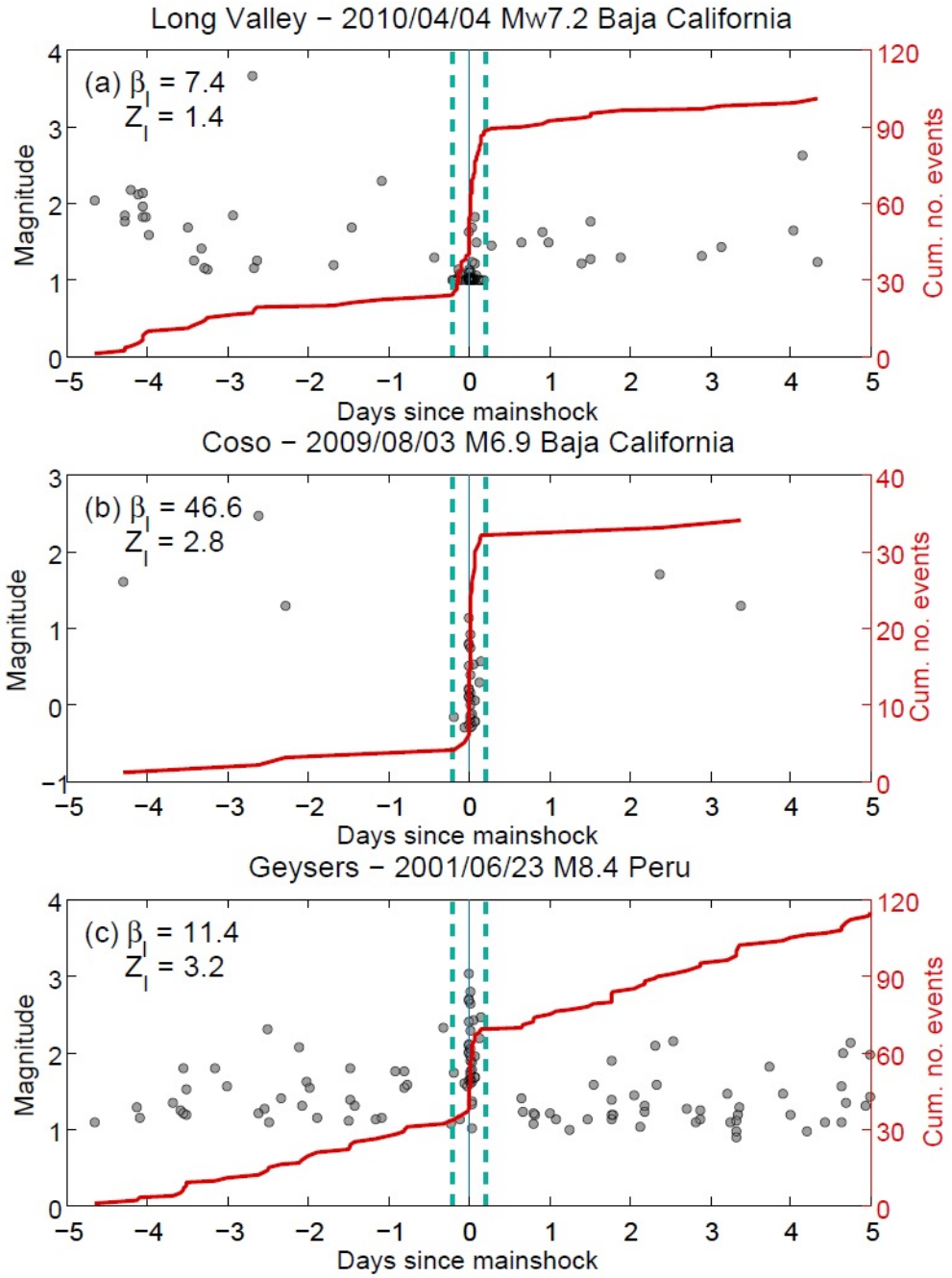

Figure S2.12 - Examples of statistically significant triggering ± 5 days around mainshocks. **(a)** 2010 *Mw*7.2 Baja California sequence in Long Valley. **(b)** 2009 *M*6.9 Baja California sequence in Coso. **(c)** 2001 *M*8.4 Peru sequence in Geysers. In each panel, circles represent earthquakes in the ANSS and our hand-picked earthquakes. For the ANSS catalog, we use only events above the Mc value (see Figure 2.12). For the hand-picked events, we estimated the magnitude as described in Section 2.3. Red line = cumulative number of earthquakes. β- and Z-values for instantaneous triggering are indicated.

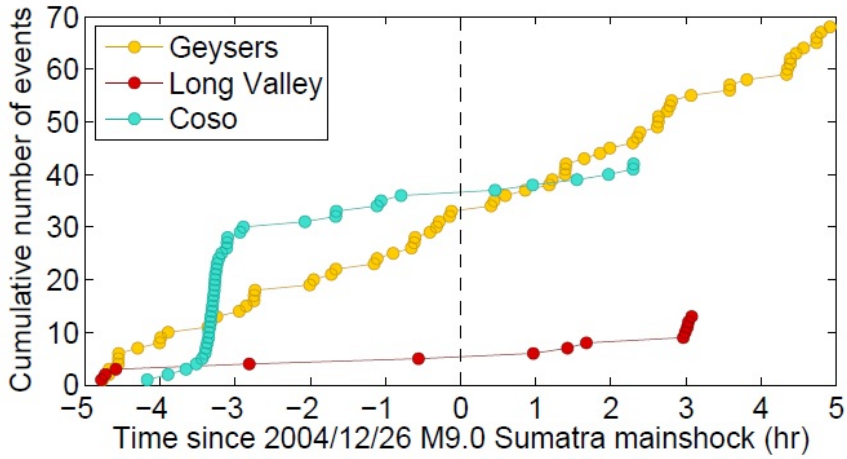

Figure S2.13 - Example of increased local earthquake activity in Coso Geothermal Field prior to the arrival of seismic waves of the 26 December 2004 *M*9.0 Sumatra earthquake. Color depicts region: Yellow = Geysers, red = Long Valley, and turquoise = Coso.

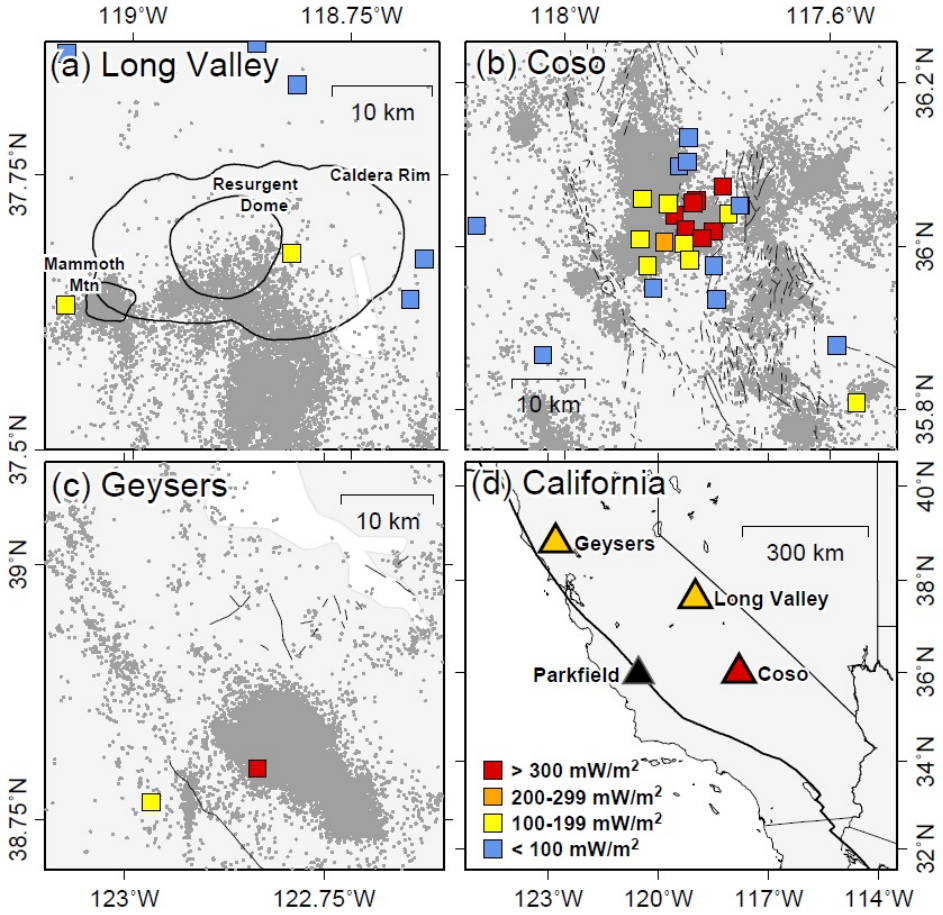

Figure S2.14 - Heat flow data for the three geothermal regions. In (a)-(c), colored squares = location and magnitude of the heat flow measurements. Legend for the heat

flow magnitudes is in (d). The triangles in (d) represent the main reference stations, as represented in Figure 2.1d.

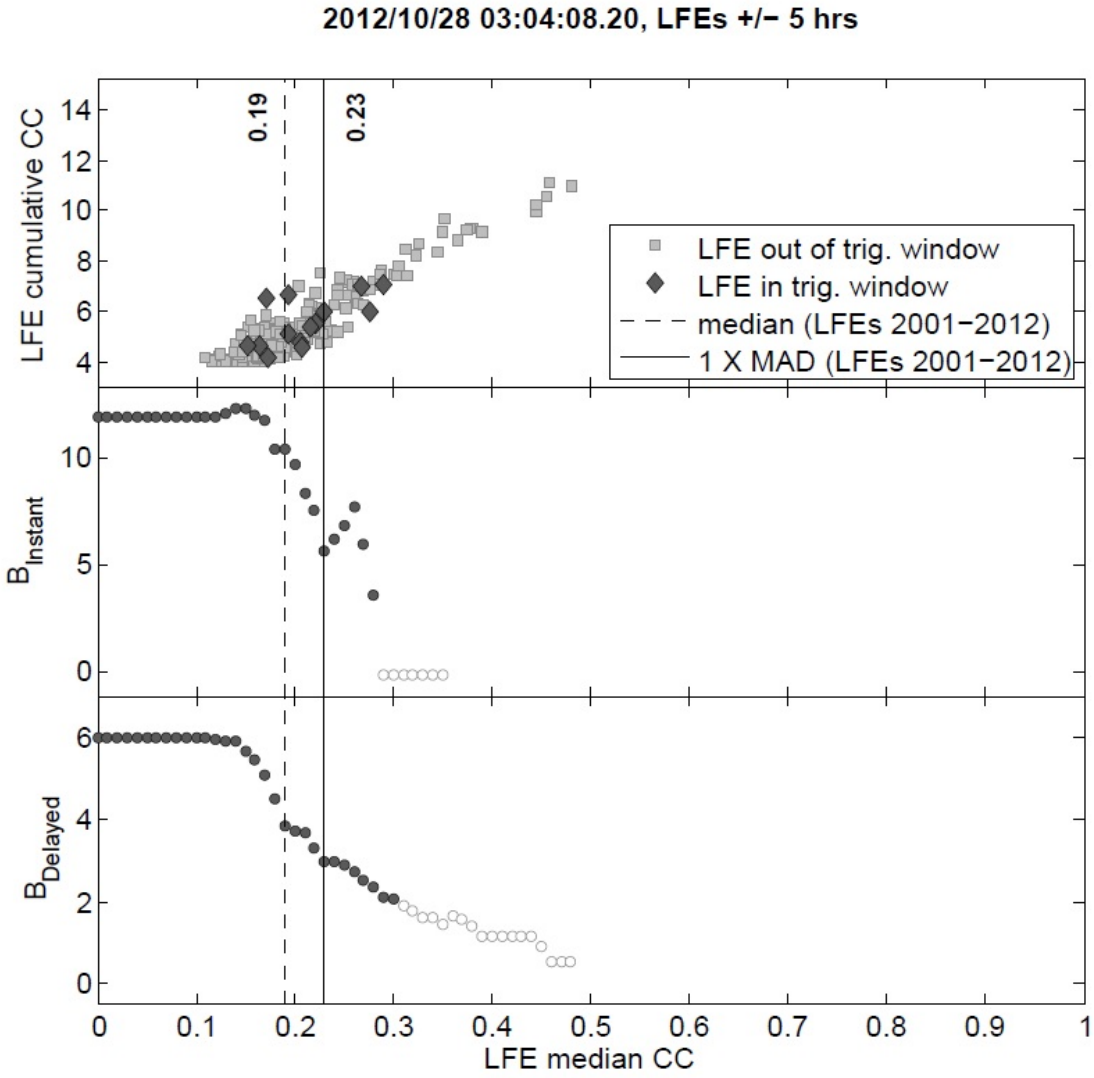

Figure S2.15 - Variation in β-value with CC value for tremor triggered by the 2012 Haida Gwaii earthquake. **(a)** Cumulative CC sum across all stations vs. median CC value of all stations used for LFE detection. Median of all median CC values from 2001-2012 and 1 times the median absolution deviation (MAD) are indicated. **(b)** Instantaneous β-value vs. changing median CC detection threshold. Filled = significant increase in activity; Open = insignificant. **(c)** Delayed β-value vs. changing median CC detection threshold.

2.9.2 Supplemental Tables

Supplemental tables of *Aiken and Peng* [2014] are quite large and not suitable for placement within this document. Therefore, they have been made available via

http://geophysics.eas.gatech.edu/people/cautry6/temp/supplementals/dissertationCh2/ (last accessed 11 March 2015). Below is a list of the table numbers and a brief description of their contents.

Table S2.1 – Event list for Long Valley Caldera

Table S2.2 – Event list for Coso Geothermal Field

Table S2.3 – Event list for Geysers Geothermal Field

Table S2.4 – Event list for Parkfield, CA

Table S2.5 - β-values for events that appear to trigger in Parkfield and the three geothermal regions

Table S2.6 – Z-values for events that appear to trigger in Parkfield and the three geothermal regions

CHAPTER 3

REMOTE TRIGGERING OF NON-VOLCANIC TREMOR ALONG THREE STRIKE-SLIP FAULTS

The results presented in this chapter are from the publish works of *Aiken et al.* [2013a] and *Aiken et al.* [2015b], as well as from the manuscript of *Aiken et al.* [2015a], which is in preparation for publication.

Summary

We conduct a systematic search of remotely triggered tremors along the Queen Charlotte Margin in western Canada [*Aiken et al.*, 2013a], the eastern Denali Fault in the western Yukon territory of northwest Canada [*Aiken et al.*, 2015b], and the Enriquillo-Plantain Garden Fault of the southern Haiti peninsula [*Aiken et al.*, 2015a]. In each region, we identify triggered tremor as non-impulsive, high-frequency signals coherent among several stations and coincident with passing surface waves. At least one distant earthquake is found to trigger tremor in each region (some times more), and we locate the triggered tremor sources via grid search using a *S*-wave velocity model unique to each region. Similar to the observations in other regions, the triggered tremors were often initiated by the Love waves and continued during the subsequent Rayleigh waves. In addition, we find that the triggering potential for each region is controlled by a combination of amplitude, period, and incident angle.

3.1 Introduction

Dynamic stresses from large earthquakes are capable of triggering a wide range of seismic/aseismic responses at remote distances by a process known as 'dynamic triggering' [*Hill and Prejean*, 2014]. These include instantaneous triggering of microearthquakes [e.g., *Velasco et al.*, 2008; *Jiang et al.*, 2010; *Aiken and Peng*, 2014],

deep tectonic tremor [e.g., *Peng and Gomberg*, 2010], earthquake swarms [*Gonzalez-Huizar et al.*, 2012], slow-slip events [*Hirose et al.*, 2012; *Zigone et al.*, 2012], and near-surface icequakes [*Peng et al.*, 2014]. Among these seismic/aseismic responses, tremor has been observed in a number of plate-bounding tectonic environments around the Pacific Rim [*Peng and Gomberg*, 2010; *Beroza and Ide*, 2011; and references therein].

Compared to earthquakes, tremor is a non-impulsive, emergent signal embedded with low-frequency earthquakes that are generated by shear slip, typically at depths greater than the seismogenic zone [e.g., *Shelly et al.*, 2007]. Icequakes, on the other hand, occur as a result of many physical processes, such as calving, crevassing, and basal shear slip at the bed of the ice sheet [*Nettles and Ekström*, 2010]. Although dynamic triggering of seismic activity has been widely observed, it is still not clear what local conditions are necessary for it to occur. Systematic studies of dynamic triggering not only help us to understand how large earthquakes affect seismic/aseismic processes at remote distances but also improve our understanding of the necessary physical conditions responsible for failure to occur.

In this chapter, the first evidence of triggered tremor along three transform faults will be presented, namely along the Queen Charlotte Margin in Haida Gwaii, Canada (Section 3.2)[*Aiken et al.,* 2013a], the eastern Denali Fault in the western Yukon Territory, Canada (Section 3.3) [*Aiken et al.,* 2015b], and the Enriquillo-Plantain Garden Fault in the southern Haiti peninsula (Section 3.4) [*Aiken et al.,* 2015a]. In each of these regions, we examine waveforms for possible high-frequency tremor signals triggered by the surface waves of teleseismic earthquakes. Searching for triggered tremor is relatively easier than searching for ambient tremor because the amplitude of triggered tremor is

generally larger [e.g., *Peng et al.*, 2008; *Rubinstein et al.*, 2007]. In addition to identifying triggered tremors, we also locate their sources. Finally, we examine the triggering potential of the teleseismic earthquakes by examining seismic wave amplitudes and frequencies, as well as their incidence on the faults.

3.2 Triggering Along the Queen Charlotte Margin, Canada [*Aiken et al.*, 2013a]

3.2.1 Tectonic Setting

The Queen Charlotte Margin (QCM) extends from the triple junction formed by the Juan de Fuca ridge, the Cascadia subduction zone, and the transform Queen Charlotte Fault (QCF) south of Haida Gwaii (Figure 3.1). The QCF connects to the Fairweather fault system further north along the Alaskan coast. The QCF is a transform boundary between the Pacific plate and the North American plate. These two plates move at a rate of ~ 5 cm yr^{-1} relative to each other [*DeMets et al.*, 2010]. In addition, motion along the QCF does not parallel the relative motion between the Pacific and North American plates, unlike the SAF where motion is mostly pure shear. The discrepancy between the direction of plate motion and the transform QCF is ~22º [*Rohr and Tryon*, 2010], which results in a transpressive environment (i.e., transform + compression) with predominant right-lateral strike-slip motion. Such a compressional environment is revealed by the 28 October 2012 M_w7.7 thrust earthquake and its aftershocks (Figure 3.1).

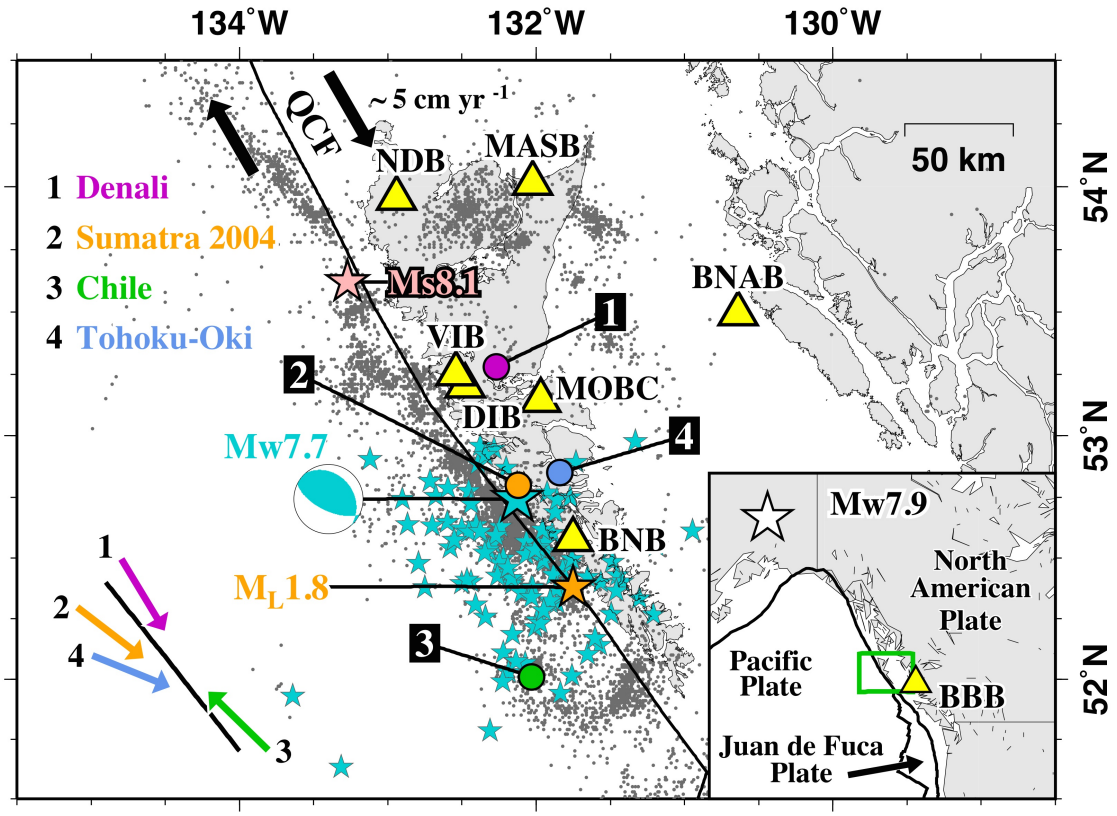

Figure 3.1 - Map view of Queen Charlotte Margin. Black lines = faults/plate boundaries. Black arrows = ~ 5 cm yr^{-1} relative plate movement along the QCF. Triangles = Canadian National Seismograph Network (CNSN) short-period and broadband stations. Numbered/colored circles = average triggered tremor locations from each triggering earthquake. Pink star = epicentral location of the 22 August 1949 M_s8.1 earthquake. Orange star south of the BNB station = location of M_L1.8 earthquake recorded close to the Love wave arrival time of the 26 December 2004 Sumatra earthquake. Turquoise star = recent 28 October 2012 M_w7.7 Queen Charlotte earthquake; its focal mechanism is indicated. Smaller turquoise stars = epicenters of its aftershocks. Bottom left inset depicts the incident angles of surface waves from each earthquake by number and color. Bottom right inset shows the location of the QCM, marked in green, with respect to western Canada and United States as well as the tectonic plates surrounding the QCM. White star in the inset = location of the 3 November 2002 M_w7.9 Denali Fault earthquake. Location of the BBB station is marked in the inset.

3.2.2 Analysis and Procedure

We first selected significant earthquakes from the Advanced National Seismic System (ANSS) worldwide catalog accessible from the Northern California Earthquake Data Center. We applied the following criteria to select the earthquakes [*Peng et al.*, 2009; *Guilhem et al.*, 2010]: the events must (1) have occurred during the 1990-2012

period, (2) have magnitude $M \geq 6.5$, (3) have occurred at depths ≤ 100 km, and (4) occurred at an epicentral distance $\geq 1{,}000$ km from the DIB station. Given these selection criteria, we obtained 745 earthquakes. We then estimated dynamic stresses generated by these earthquakes using surface-wave magnitudes, similar to *van der Elst and Brodsky* [2010] (see Appendix A). We only kept earthquakes that generated dynamic stresses greater than 1 kPa, which is approximately the minimum tremor triggering threshold identified in other regions [*Peng et al.*, 2009; *Rubinstein et al.*, 2009; *Guilhem et al.*, 2010; *Chao et al.*, 2012b]. Eventually, we find 51 such events (Table S3.1).

Next, we retrieved 5 hours of data following the origin times of these 51 earthquakes recorded at the short-period and broadband stations in the Canadian National Seismograph Network (CNSN). We then removed the instrument responses and applied a 5-15 Hz band-pass filter to capture local tremor activity that may have been triggered by the earthquake. We note that ambient tremor is mostly observed at the frequency range of 1-10 Hz [e.g., *Obara*, 2002]. Here we chose the 5-15 Hz band mainly because we would like to remove contaminations from the regional and teleseismic *P*-wave signals associated with both the mainshock and large early aftershocks [e.g., *Guilhem et al.*, 2010]. Because the signal-to-noise ratio of triggered tremor is generally higher than that of ambient tremor [*Rubinstein et al.*, 2007; *Peng et al.*, 2008], we can filter the data at slightly higher frequency band in order to separate local tremor and distant signals. Broadband waveforms without clipped or poorly recorded data were rotated to the great circle path (GCP, radial) and a clockwise 90° rotation (transverse) direction using the SAC (Seismic Analysis Code) command "rotate to GCP." After filtering the seismic data, we visually inspected the envelope functions and the three-component filtered seismic

data for tremors triggered by the large amplitude surface waves, similar to *Chao et al.* [2012a]. For broadband stations without clipped or poorly recorded data, we computed an average envelope by stacking the radial, transverse, and vertical component envelope functions and dividing by 3. We identified triggered tremors as non-impulsive, high-frequency signals observable among several stations and coincident with the surface waves of the earthquakes [*Peng et al.*, 2008].

Finally, we located the tremor bursts that were coherent among at least 3 stations in the QCM using an envelope cross-correlation method [*Chao et al.*, 2013]. Simply, we computed travel time differences based on cross-correlation of tremor envelopes and then searched for the minimum travel time residual for all possible station pairs using a *S*-wave velocity model for this region, e.g., Table 2 from *Bustin et al.* [2007]. Since the source depth is not well constrained with this method, we set the depth to be 25 km based on the location of tremor sources along the transform SAF [e.g., *Shelly et al.*, 2009] and the transpressional Alpine Fault in New Zealand [*Wech et al.*, 2012].

3.2.3 Triggering Observations

We observed tremors triggered by surface waves from 5 large, distant mainshocks (Table S3.1). Figure 3.2 shows an example of tremor triggered by the 26 December 2004 M_w9.2 Sumatra mainshock as recorded by several stations. Strong tremor bursts are triggered during the Love wave around 3100 – 3400 s and the subsequent Rayleigh wave around 4200 – 4500 s, with a few weaker tremors occurring during the longer period Rayleigh wave around 3500 s. We were able to identify at least 17 tremor bursts, coherent among 3 seismic stations. Similarly, surface waves from the 11 March 2011 M_w9.1 Tohoku-Oki earthquake triggered tremor, and the triggered tremor was recorded

by at least 3 stations (Figure 3.3 and S3.1). Strong tremor bursts are triggered during the Love wave around 1500-1600 s and the subsequent Rayleigh wave around 1700-1800 s, with a few weaker tremors occurring during the shorter period Rayleigh waves after 1800 s.

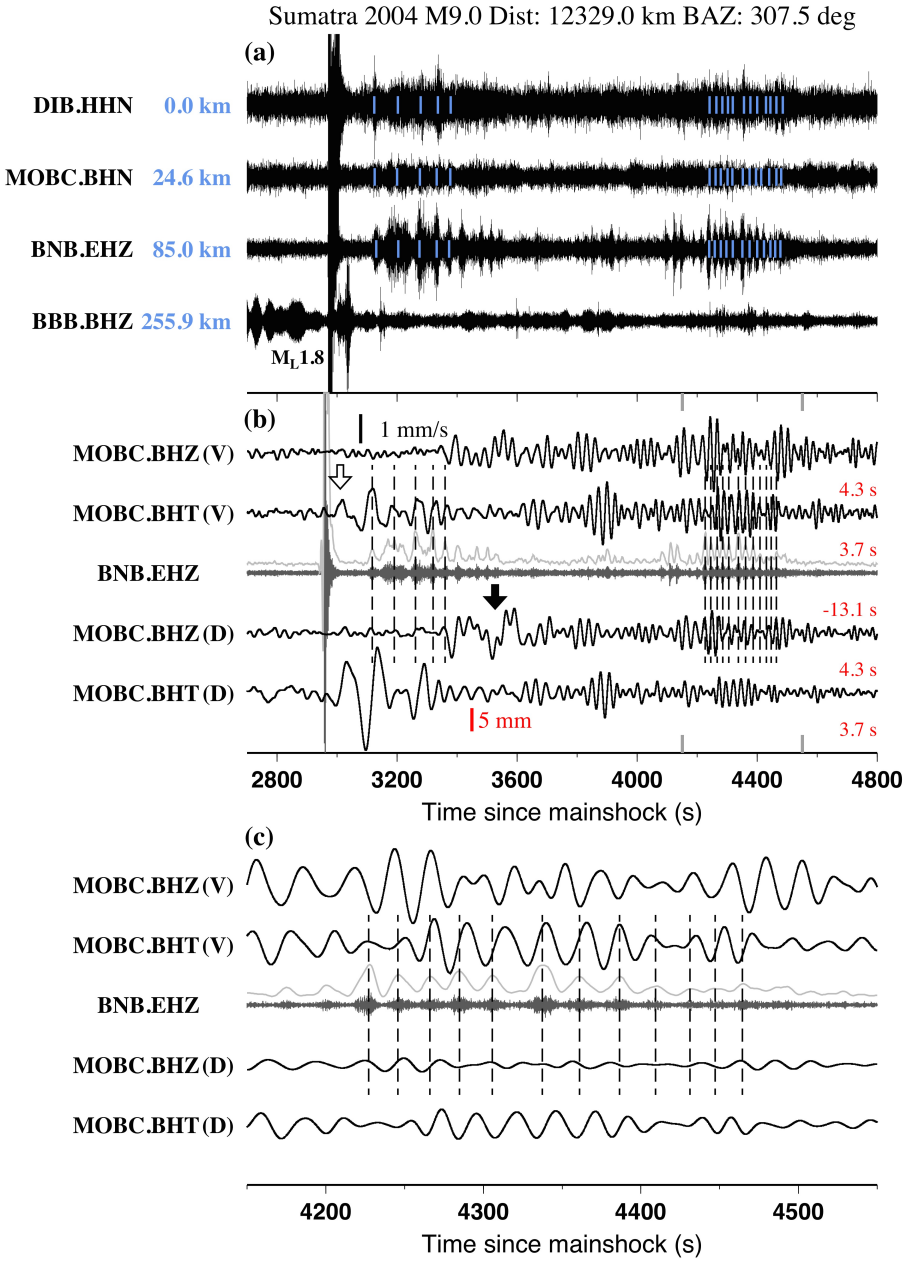

Figure 3.2 - Evidence of tremors triggered in QCM by surface waves from the 26 December 2004 M_w9.0 Sumatra mainshock as recorded at multiple stations. **(a)** 5-15 Hz band-pass filtered velocity seismograms with denoted station names, channels, along-strike distances with respect to the DIB station. Vertical blue lines = tremor burst peaks

hand-picked from the filtered envelope functions used for tremor location. **(b)** A detailed comparison between transverse (BHT) and vertical (BHZ) velocity (V) and displacement (D) seismograms and a 5-15 Hz band-pass filtered vertical seismogram. Zero-time is the 2004 Sumatra mainshock origin time. Seismograms are time-shifted back to the tremor occurrence time to reflect the relationship between surface waves and tremor at the source region. Adjusted times are marked in red. The 4.1 km s^{-1} Love and 3.5 km s^{-1} Rayleigh wave arrival times are marked by white and black arrows, respectively. Thick, vertical bars (black/red) mark the amplitude scale of the surface wave velocity and displacement, respectively. Vertical dashed lines = peaks of tremor envelope functions used for tremor location. **(c)** Zoom-in of tremors triggered by the subsequent Rayleigh waves.

To compare the relationship between surface waves and tremor signals, we shifted the transverse and vertical components back to the tremor source based on the 4.1 km s^{-1} Love and 3.5 km s^{-1} Rayleigh wave phase velocities [e.g., *Rubinstein et al.*, 2009; *Peng et al.*, 2009]. Similarly, we shifted a band-pass filtered waveform back to the tremor source based on predicted *S*-wave travel times. For a near strike-parallel incidence on a vertical strike-slip fault, the strike-parallel shear stress is proportional to the Love wave particle velocity [*Peng et al.*, 2008; *Hill*, 2012] for two reasons. First, the maximum inflection point of Love wave displacement gives rise to maximum dynamic stress with associated double-couple source that either promotes or inhibits shear on the vertical fault place. Second, the maximum inflection point of displacement is equivalent to the maximum velocity. However, for a strike-parallel incidence on a shallow thrust fault, the dip-parallel shear stress is proportional to the Love wave displacement [*Rubinstein et al.*, 2007, 2009]. This is because Love wave displacement is the greatest in the near surface and decreases exponentially with depth, creating a displacement gradient (strain) on a near-horizontal plane. Hence, when the Love wave displacement is in the seaward direction, the overriding plate moves more than the underlying plate, resulting in a positive shear strain that would load and promote thrust failure on the plate interface.

When the displacement is in the landward direction, a negative shear strain is induced, which would unload the thrust fault. Because both faulting styles are present at the QCM, we compare the tremor bursts to both velocity and displacement seismograms.

Figure 3.2 shows that the first 5 tremor bursts triggered by the 2004 Sumatra mainshock are coherent with the peaks in the Love wave velocity. The latter 12 bursts show a mixed correlation with the transverse velocity and vertical displacement seismograms, with the latter being proportional to the dilatational stress changes [*Rubinstein et al.*, 2009]. In addition to the tremor sequences triggered by the 2011 Tohoku-Oki and 2004 Sumatra earthquakes, we were also able to identify tremors triggered by surface waves of the 3 November 2002 M_w7.9 Denali Fault earthquake, and possibly by the 27 February 2010 M_w8.8 Maule, Chile and 11 April 2012 M_w8.6 Sumatra mainshocks (Figure 3.3). Tremors triggered by the 2002 Denali Fault earthquake are more coherent with the Love wave displacements (Figure 3.3a). However, for the 2011 Tohoku-Oki mainshock, the tremor first correlated with the Love wave velocity, and then later with the Rayleigh wave displacement (Figure 3.3c).

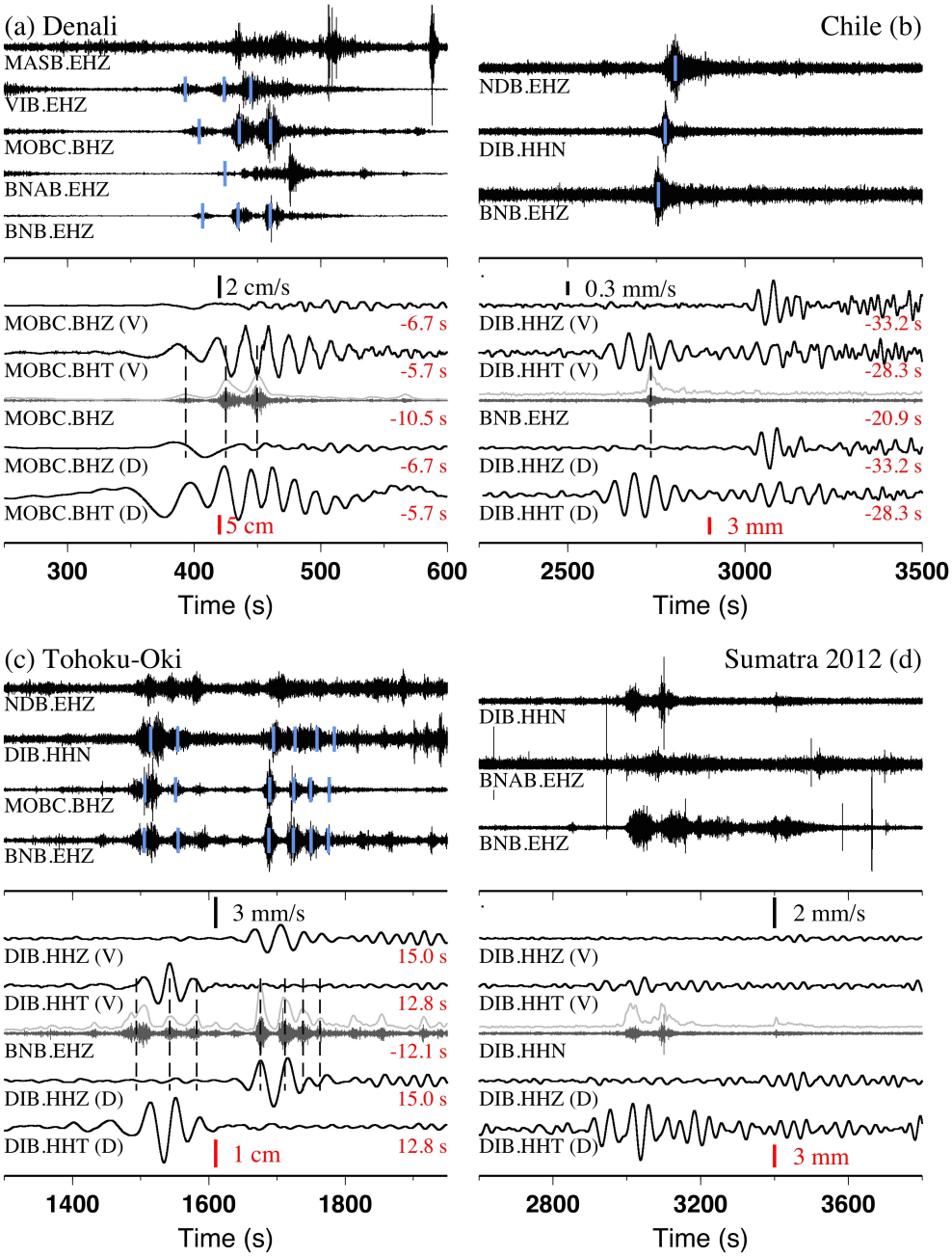

Figure 3.3 - Evidence of tremors triggered by surface waves from several mainshocks as recorded by multiple stations. Symbols and notations are similar to Figure 3.2. **(a)** 3 November 2002 M_w7.9 Denali Fault, **(b)** 27 February 2010 M_w8.8 Maule, Chile, **(c)** 11 March 2011 M_w9.0 Tohoku-Oki, and **(d)** 11 April 2012 M_w8.6 Sumatra earthquakes.

Locations of the triggered tremors are shown in Figure 3.1. In general, tremors occurred mainly in the southeastern portion of Haida Gwaii and around the QCM (Figure 3.1 and Table S3.2). It is also possible that some tremor occurred in the northwestern

portion of the island. For example, the tremor signals recorded at station NDB during the 2011 Tohoku-Oki earthquake did not match the move-out for a tremor source radiating from the southeast, which suggests a possible new source. However, we could not locate this source based on one recording. In addition, we were unable to determine accurate locations of tremors possibly triggered by the 2012 Sumatra earthquake because the tremor bursts were not coherently identifiable among at least 3 stations.

3.2.4 Characteristics of Triggering Waves

Similar to previous systematic studies of dynamically triggered tremors [e.g., *Peng et al.*, 2009], we examined the peak ground velocities (PGVs) of our earthquakes to determine a stress-triggering threshold. Figure 3.4a shows the transverse PGVs, dynamic stresses, and back-azimuths of all examined earthquakes. The transverse PGVs were measured at station MOBC for earthquakes occurring before 2004 and all others were measured at station DIB. PGVs of the 2002 Denali and 22 January 2003 Colima events were corrected as outlined in the Section 3.2.7 (e.g., Figure S3.2). In order to avoid contamination of the PGV measurements by high-frequency local seismicity, we low-passed filtered velocity seismograms 1-s prior to measuring the PGVs. In addition, we examined the surface wave amplitude spectra generated by each earthquake used in this study (Figure 3.4b). For the amplitude spectra, we first computed the arrival times of the 5 and 2 km s^{-1} wave velocity, cut the transverse velocity data between these times, and then computed the Fast-Fourier Transform (FFT). By computing the FFT between 5 and 2 km s^{-1}, the majority of the surface wave energy is captured. Finally, we smoothed the amplitude spectra with a sliding window of 5 points [*Peng et al.*, 2009].

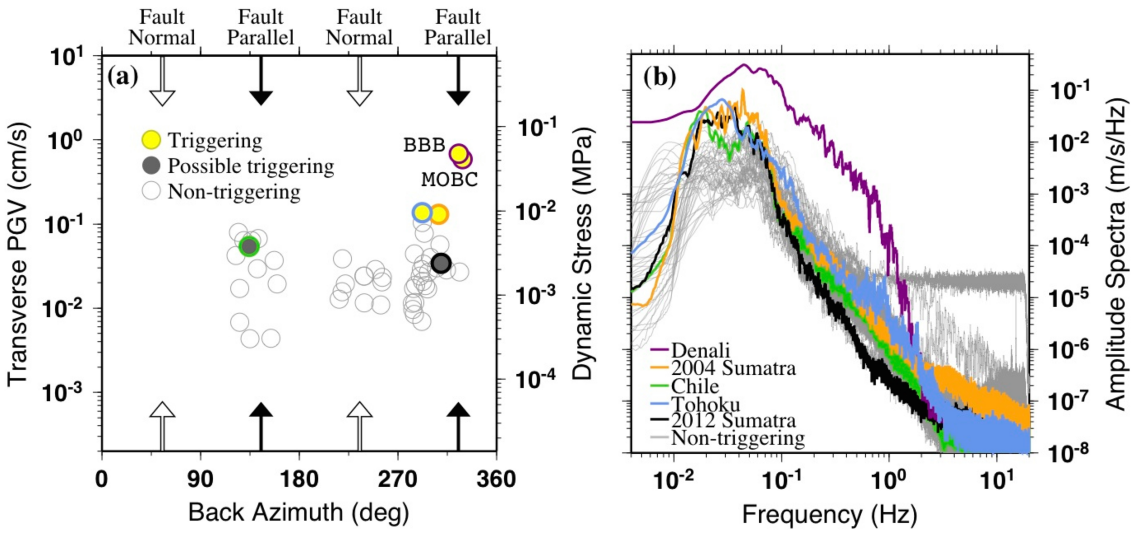

Figure 3.4 - Analysis of peak ground velocities (PGVs) and velocity amplitude spectra. **(a)** Transverse PGVs and dynamic stresses vs. back azimuths of all examined earthquakes. PGVs are low-pass filtered 1-s. Yellow circles = triggering earthquakes (i.e., 2002 Denali, 2004 Sumatra, and 2011 Tohoku-Oki), gray circles = possibly triggering earthquakes (i.e., 2010 Chile and 2012 Sumatra), and open circles = non-triggering earthquakes. **(b)** Transverse velocity amplitude spectra for all earthquakes examined in this study. Gray lines = non-triggering earthquakes, and colored lines = both triggering and possibly triggering mainshocks. Color indicates event name as used in Figure 3.1 and part (a) of this figure. Spectra that becomes linear at high frequencies is the 22 January 2003 Colima earthquake, and this anomaly is likely due to the recording error as mentioned in the Section 3.2.7.1.

The most promising cases of earthquakes triggering tremors around the QCM – the 2002 Denali, 2004 Sumatra, and 2011 Tohoku-Oki earthquakes – generated dynamic stresses > 7 kPa and large, long-period (>30 s) amplitude spectra (Figures 3.4 and S3.3). In addition, both the Love and Rayleigh waves from these earthquakes triggered tremors. The 2012 Sumatra earthquake, which also generated large, long-period amplitude spectra, may have triggered 2 tremor bursts with the Love wave. Similarly, the 2010 Chile earthquake possibly triggered 1 tremor burst with the Love wave. However, it is also possible that the observed tremor during the Chile mainshock could be a coincidence because only 1 clear burst occurred during the Love wave. In comparison, the long-period (>30 s) amplitude spectra of the Chile mainshock is lower than that of the 2002

Denali, 2004 Sumatra, 2011 Tohoku-Oki, and 2012 Sumatra earthquakes. In addition, after applying a low-pass 30s filter to the transverse velocity seismograms and measuring the PGVs, most of the earthquakes separate into a non-triggering and triggering group (Figure S3.4).

3.2.5 Discussion and Conclusions

In *Aiken et al.* [2013a], we provided clear evidence of remotely triggered tremors around the QCM. Despite the limited number of seismic stations in this region, we were able to locate the tremor sources of at least 4 triggered tremor episodes. We set the depth to be at 25 km because tremor source depth in other strike-slip regions is ~25-30 km [e.g., *Peng et al.*, 2009]. Setting the depth may not reflect the true depth of the tremor sources. However, we surmise that the tremors occur deep within the QCM due to the fact that the tremors were coherent at 3 or more stations within ~100 km of the DIB station, were coincident with surface waves from earthquakes, and contained relatively low frequencies as compared with regular earthquakes, similar to deep, triggered tremor observed elsewhere [*Peng and Gomberg*, 2010].

As shown in Figure 3.1, the tremor was triggered mainly to the east of the QCF beneath Haida Gwaii. Hence, it is tempting to conclude that tremor occurred around the underthrusting plate. Although the dip of the QCF is very close to vertical [*Kao et al.*, 2012], our average horizontal location errors are on the order of ~10 km. Thus, we cannot completely rule out the possibility that tremor occurred on the downward extension of the QCF. In addition, tremor correlated with Love wave displacement for the 2002 Denali Fault earthquake (Figure 3.3a) and with Love wave velocity for the 2004 Sumatra (Figure 3.2) and 2011 Tohoku-Oki earthquakes (Figure 3.3c). These observations also indicate

that we cannot rule out either low-angle thrust or vertical strike-slip mechanisms since the triggered tremors are modulated by both displacement and velocity seismograms, respectively [*Hill*, 2012]. In addition, we found that tremors correlated with dilatational Rayleigh wave stresses, suggesting pore pressure variation as a possible mechanism for tremor generation, which has been proposed in previous studies [e.g. *Miyazawa and Brodsky*, 2008; *Rubinstein et al.*, 2009; *Hill et al.*, 2013]. Therefore, we cannot make a conclusion on which single faulting style is responsible for the triggered tremor signals and leave this open for a future work.

Previous studies have also suggested that dynamic triggering may be dependent upon amplitude, frequency, and back-azimuth of incoming surface waves [*Brodsky and Prejean*, 2005; *Peng et al.* 2009, 2010; *Guilhem et al*., 2010; *Chao et al*., 2012b]. In our study, most of the earthquakes exhibited near strike-parallel incidence with relatively fewer earthquakes having strike-normal incidence. The five earthquakes that have triggered tremor all had near strike-parallel incidences. In most cases, tremors were triggered primarily by the Love waves, and additional tremors were triggered by the subsequent Rayleigh waves. This is consistent with the near strike-parallel incidence for many triggering earthquakes and tremor, which tends to produce maximum triggering potential for vertical strike-slip faults and low-angle thrust faults [*Hill*, 2012]. Moreover, four of the five triggering events produced higher-amplitude long-period (>30 s) surface waves than non-triggering events (Figure 3.4). In summary, the fact that these five earthquakes triggered tremor around the QCM could be due to a combination of high PGVs, long-period signals, and near strike-parallel incidence.

We note that none of the events with strike-normal incidence triggered tremor. This could be caused by the fact that not many large earthquakes from that direction (i.e., southern Pacific) produced large enough PGVs to trigger tremor. Alternatively, they may have triggered weak tremor signals but were undetected by the relatively sparse network in this region. This could also be used to explain that a relatively high peak dynamic stress is needed to trigger (5-7 kPa) in this region, as compared with the 2-3 kPa threshold found along the Parkfield-Cholame section of the SAF [*Peng et al.*, 2009].

Our observations suggest that triggered tremor could occur at many places along major strike-slip faults and subduction zones. Although the necessary conditions for tremor generation are still not clear at this stage, we note that tremor predominantly occurs either in the compressive [e.g., *Rubinstein et al.*, 2007] or transpressive [e.g., this study; *Wech et al.*, 2012; *Peng et al.*, 2009; *Peng et al.*, 2013] tectonic settings. Of course, this could be simply a sampling bias because not many regions with extensional and trans-extensional tectonic settings have been examined.

As mentioned before, the triggered tremor is not far from the epicenters of the recent 28 October 2012 M_w7.7 and 22 August 1949 M_s8.1 Queen Charlotte earthquakes [*Lamontagne et al.*, 2008], the latter of which ruptured a total length of ~500 km along the QCF. In addition, weak ambient tremor has already been detected beneath the QCM (H. Kao, personal communication, 2012). It is still not clear what role tremor plays in large earthquake cycles. Some recent studies suggest that ambient tremor patterns may change immediately before large earthquakes [*Shelly*, 2009] or may be absent [*Gomberg et al.*, 2012]. Thus, it is critical to improve the seismic instrumentation around the QCM (and elsewhere around the world) to better detect and locate both triggered and ambient

tremor. This will not only help to better understand the underlying physical mechanisms responsible for tremor generation along major faults but also has significant hazard implications.

3.2.6 Supplemental Information

This section describes the amplitude correction for the MOBC station north component in the 2002 Denali and 2003 Colima cases and also contains four figures and two tables that are referenced here and/or in previous sections.

3.2.6.1 Supplemental Text

The following describes the amplitude correction for the MOBC station north component in the 2002 Denali and 2003 Colima cases. For the 2002 Denali Fault event, we have marked the transverse PGV measurements for both the MOBC and BBB stations (Figure 3.4). The north component at the MOBC station for this event did not accurately record the amplitudes by 3 orders of magnitude and therefore required a correction. To do so, we first removed the mean and then divided by the measured north component PGV from the MOBC station. Next, we multiplied the MOBC data by the measured north component PGV from the BBB station. We then removed the instrument response from the MOBC north component data and rotated the components to the great circle path to obtain the transverse component. Figure S3.2 shows the corrected transverse component at station MOBC and the time-shifted transverse component from the BBB station using an apparent velocity of 4.1 km s^{-1}. The good correlation in the first few cycles of the Love wave indicates that our correction is acceptable. We also applied this to the 22 January 2003 Colima earthquake that exhibited a similar amplitude recording error.

3.2.6.2 Supplemental Figures

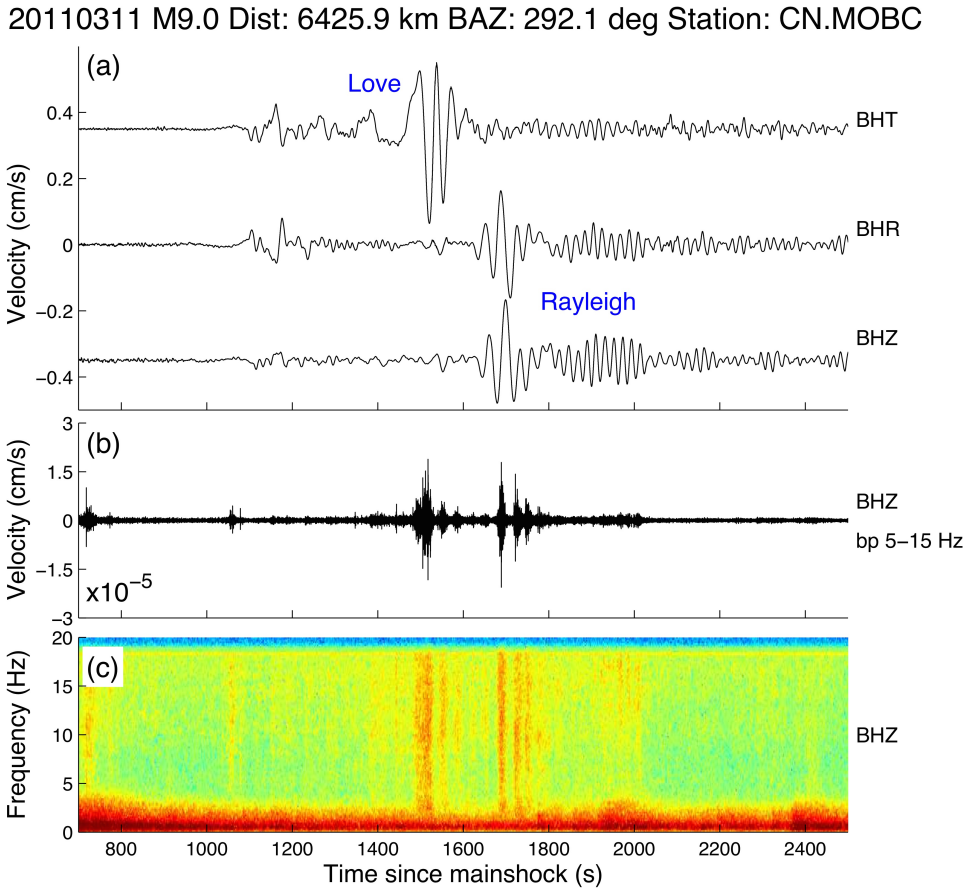

Figure S3.1 - Evidence of tremors triggered in QCM by surface waves from the 11 March 2011 M_w9.0 Tohoku-Oki mainshock as recorded at the MOBC station. **(a)** Instrument-corrected transverse, radial, and vertical component unfiltered velocity seismograms with Love and Rayleigh waves marked. **(b)** Band-pass filtered 5-15 Hz instrument-corrected velocity seismogram depicting tremors triggered by the Love and Rayleigh waves of the Tohoku-Oki mainshock. **(c)** Spectrogram showing the frequency contents of the triggered tremors.

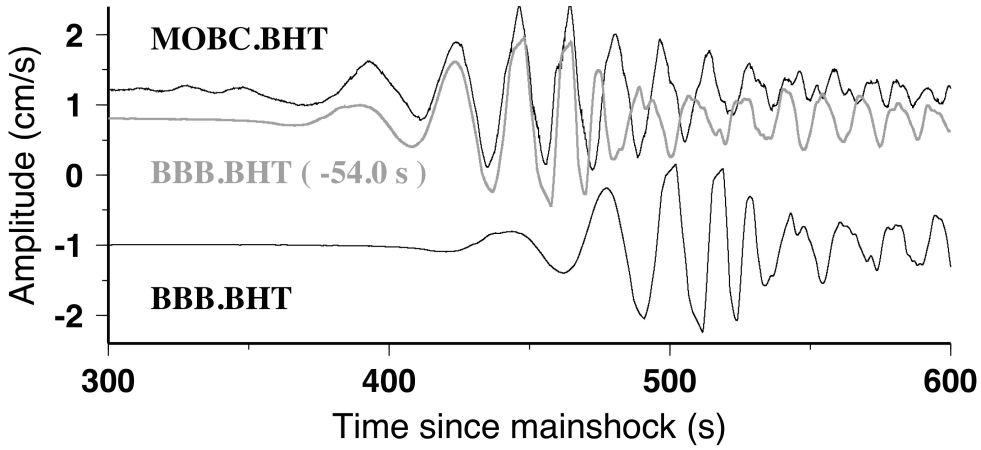

Figure S3.2 - Comparison of MOBC and BBB station transverse velocity components after correcting the amplitude of the MOBC station north component. The shifted BBB seismogram (gray) was shifted by the difference in 4.1 km s^{-1} Love wave arrival times at the MOBC and BBB stations.

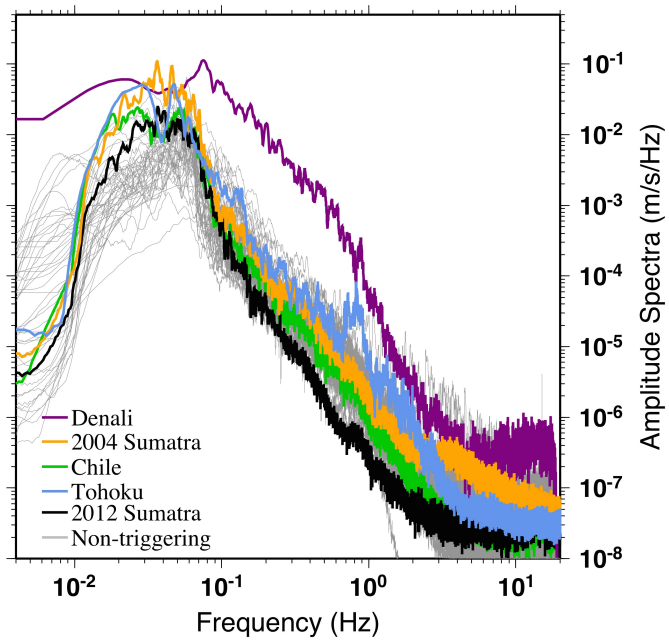

Figure S3.3 - Vertical velocity amplitude spectra for all mainshocks. Symbols are the same as in Figure 3.4b.

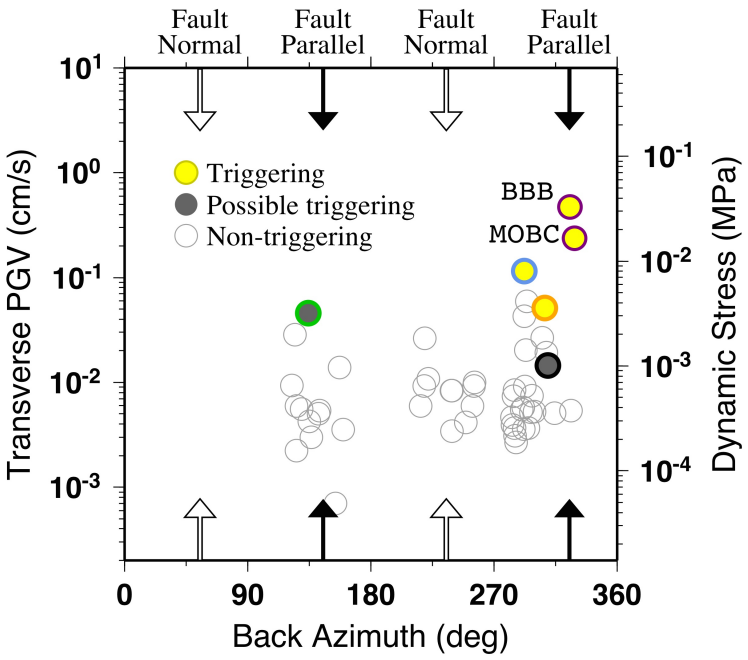

Figure S3.4 - Transverse PGVs and dynamic stress vs. back azimuth for earthquakes to the Queen Charlotte Fault region (low-pass filtered 30s). Symbols are the same as in Figure 3.4a.

3.2.6.3 Supplemental Tables

Table S3.1 – Event list for Queen Charlotte Margin, Haida Gwaii, Canada.

# evid	yr	mo	dy	hr	mi	sec	long.	lat.	depth	mag	dist.	BAZ	PGV_Z	PGV_T	Q
199606100403	1996	06	10	04	03	35.48	-177.6320	51.5640	33.00	7.90	3031.86	284.97	0.0442	0.0313	0
199606101524	1996	06	10	15	24	56.00	-176.8470	51.4780	26.30	7.30	2984.55	284.40	0.0172	0.0092	0
199611121659	1996	11	12	16	59	44.03	-75.6750	-14.9930	33.00	7.70	9286.43	125.53	0.0068	0.0063	0
199701112028	1997	01	11	20	28	26.02	-102.7560	18.2190	33.00	7.20	4654.33	135.07	0.0043	0.0055	0
199704211202	1997	04	21	12	02	26.43	166.6760	-12.5840	33.00	7.80	9285.01	239.11	0.0116	0.0073	0
199712051126	1997	12	05	11	26	54.69	162.0350	54.8410	33.00	7.80	4142.17	299.60	0.0401	0.0129	0
199803250312	1998	03	25	03	12	25.07	149.5270	-62.8770	10.00	8.10	14537.70	216.28	0.0128	0.0062	0
199903201047	1999	03	20	10	47	45.93	-177.6680	51.5870	33.00	6.90	3033.25	285.04	0.0084	0.0046	0
199909301631	1999	09	30	16	31	15.69	-96.9310	16.0590	60.60	7.50	5154.20	129.43	0.0636	0.0414	0
199910160946	1999	10	16	09	46	44.13	-116.2710	34.5940	0.02	7.10	2431.85	141.82	0.0296	0.0421	0
199912062312	1999	12	06	23	12	33.54	-154.3469	57.3424	43.64	6.80	1458.66	297.14	0.0169	0.0335	0
200011160454	2000	11	16	04	54	56.74	152.1690	-3.9800	33.00	8.00	9390.74	255.87	0.0232	0.0245	0
200011160742	2000	11	16	07	42	16.93	153.1020	-5.2330	30.00	7.80	9442.85	254.38	0.0109	0.0073	0
200011172101	2000	11	17	21	01	56.49	151.7810	-5.4960	33.00	7.80	9551.74	255.30	0.0206	0.0120	0
200101101602	2001	01	10	16	02	42.64	-153.2810	56.7744	36.38	6.93	1385.22	294.99	0.0186	0.0130	0
200101131733	2001	01	13	17	33	32.38	-88.6600	13.0490	60.00	7.70	5890.13	122.31	0.0421	0.0330	0
200106232033	2001	06	23	20	33	14.13	-73.6410	-16.2650	33.00	8.40	9518.72	124.48	0.0799	0.0336	0
200111140926	2001	11	14	09	26	10.01	90.5410	35.9460	10.00	7.80	9305.54	326.15	0.0270	0.0294	0
200211032212	2002	11	03	22	12	41.52	-147.4529	63.5141	4.20	7.90	1439.28	328.85	0.5940	2.4000	1
200301220206	2003	01	22	02	06	34.61	-104.1040	18.7700	24.00	7.60	4536.76	136.44	0.0637	0.0563	0
200309251950	2003	09	25	19	50	06.36	143.9100	41.8150	27.00	8.30	6060.70	294.15	0.0779	0.0441	0
200309252108	2003	09	25	21	08	00.03	143.5930	41.7740	33.00	7.40	6083.14	294.31	0.0046	0.0041	0
200311170643	2003	11	17	06	43	06.80	178.6500	51.1460	33.00	7.80	3289.26	286.02	0.0187	0.0131	0
200412231459	2004	12	23	14	59	04.41	161.3450	-49.3120	10.00	8.10	12945.54	221.95	0.0195	0.0070	0
200412260058	2004	12	26	00	58	53.45	95.9820	3.2950	30.00	9.00	12303.86	307.01	0.1310	0.1150	1
200503281609	2005	03	28	16	09	36.53	97.1080	2.0850	30.00	8.60	12359.85	305.33	0.0300	0.0264	0
200506150250	2005	06	15	02	50	54.19	-125.9530	41.2920	16.00	7.20	1412.76	157.09	0.0369	0.0513	0
200506170621	2005	06	17	06	21	42.59	-126.5740	40.7730	12.00	6.60	1452.64	159.79	0.0195	0.0163	0
200604202325	2006	04	20	23	25	02.15	167.0890	60.9490	22.00	7.60	3629.30	308.08	0.0564	0.0333	0
200605031526	2006	05	03	15	26	40.29	-174.1230	-20.1870	55.00	8.00	9059.77	219.14	0.0157	0.0155	0
200611151114	2006	11	15	11	14	13.57	153.2660	46.5920	10.00	8.30	5146.94	293.32	0.0332	0.0271	0
200701130423	2007	01	13	04	23	21.16	154.5240	46.2430	10.00	8.10	5092.55	292.21	0.1040	0.0703	0
200704012039	2007	04	01	20	39	58.71	157.0430	-8.4660	24.00	8.10	9484.50	249.32	0.0289	0.0103	0
200708152340	2007	08	15	23	40	57.89	-76.6030	-13.3860	39.00	8.00	9082.57	125.50	0.0172	0.0149	0
200709121110	2007	09	12	11	10	26.83	101.3670	-4.4380	34.00	8.50	12735.87	297.76	0.0267	0.0218	0
200712190930	2007	12	19	09	30	27.93	-179.5090	51.3600	34.00	7.20	3161.48	285.50	0.0117	0.0094	0
200805120628	2008	05	12	06	28	01.57	103.3220	31.0020	19.00	7.90	9247.18	314.33	0.0284	0.0313	0
200901151749	2009	01	15	17	49	39.07	155.1540	46.8570	36.00	7.40	5013.16	292.55	0.0207	0.0211	0
200909291748	2009	09	29	17	48	10.99	-172.0950	-15.4890	18.00	8.10	8497.70	219.23	0.0387	0.0199	0
200910072203	2009	10	07	22	03	14.47	166.5100	-13.0060	45.00	7.70	9334.11	239.02	0.0240	0.0083	0
200910072218	2009	10	07	22	18	51.24	166.3820	-12.5170	35.00	7.80	9295.62	239.39	0.0240	0.0082	0
201001100027	2010	01	10	00	27	39.32	-124.6925	40.6520	29.33	6.50	1514.80	154.05	0.0044	0.0095	0
201002270634	2010	02	27	06	34	11.53	-72.8980	-36.1220	22.90	8.80	11435.26	134.27	0.0544	0.0435	2
201004042240	2010	04	04	22	40	42.15	-115.2872	32.2587	10.00	7.20	2704.63	142.56	0.0669	0.0778	0
201103090245	2011	03	09	02	45	20.33	142.8420	38.4350	32.00	7.50	6386.05	291.89	0.0069	0.0181	0
201103110546	2011	03	11	05	46	24.12	142.3730	38.2970	29.00	9.10	6425.93	292.09	0.1360	0.2200	1
201103110615	2011	03	11	06	15	40.28	141.1110	36.2810	42.60	7.90	6663.95	291.28	0.0288	0.0360	0
201103110625	2011	03	11	06	25	50.30	144.5900	38.0580	18.60	7.70	6306.38	290.42	0.0241	0.0358	0
201106240309	2011	06	24	03	09	39.47	-171.8360	52.0500	52.00	7.30	2637.32	283.18	0.0114	0.0254	0
201109021055	2011	09	02	10	55	53.59	-171.7080	52.1710	32.00	6.80	2624.75	283.41	0.0097	0.0055	0
201204110838	2012	04	11	08	38	36.90	93.0780	2.2940	20.00	8.60	12553.15	309.27	0.0340	0.0589	2

Earthquake parameters of the 51 teleseismic events analyzed in this study.
The earthquake catalog information (origin time, location, and magnitude)
was obtained from the Advanced National Seismic System (ANSS) catalog.
The epicentral distance and back-azimuth (BAZ) were computed relative to
the broadband station DIB (stlo: -132.477, stla: 53.2025). The peak ground
vertical (PGV_Z) and transverse (PGV_T) velocities were measured from the
broadband recording by station MOBC before 2004 and by station DIB after
2004. The PGVs are in units of cm/s. The quality (Q) 1 marks events that
triggered tremor near the Queen Charlotte Fault (QCF), 2 marks those that
possibly triggered tremor the QCF, and 0 marks those that did not.

Table S3.2 – Average tremor locations by triggering earthquake.

```
# evid              long.             lat.        dep.
200211032212   -132.27 +/-0.25    53.28 +/-0.08   25.00
200412260058   -132.12 +/-0.11    52.80 +/-0.05   25.00
201002270634   -132.01 +/-0.10    52.01 +/-0.49   25.00
201103110546   -131.84 +/-0.14    52.85 +/-0.03   25.00
201204110838         n/a               n/a         n/a
# Average locations of the 5 triggered
# tremor episodes.  The depth was set
# to 25 km, the top of the Moho layer.
# We were not able to locate the tremor
# source for the 2012 Sumatra event.
```

3.3 Triggering along the Eastern Denali Fault, Canada [*Aiken et al.*, 2015b]

3.3.1 Tectonic Setting

The eastern Denali Fault (EDF) resides in northwest Canada, where relative motion between the Pacific Plate and North American Plate changes from transform/strike-slip in southeast Alaska to subduction in south-central Alaska (Figure 3.5). The Denali Fault is a major intraplate strike-slip fault that extends from central Alaska, US, to western Yukon Territory, Canada. It is composed of the central and eastern sections that are segmented by the splay Totschunda Fault. The 3 November 2002 *Mw*7.9 Denali Fault earthquake [*Eberhart-Phillips et al.*, 2003], which ruptured the Susitna Glacier, central Denali, and Totschunda Faults, was the largest strike-slip earthquake to have occurred in the United States since the great 1906 San Francisco earthquake. Along the EDF, earthquake activity since 1995 has been of small-to-moderate size ($Mw < 6$) with both thrust and strike-slip focal mechanisms (Table S3.3). These focal mechanisms indicate that the EDF is a transpressional environment.

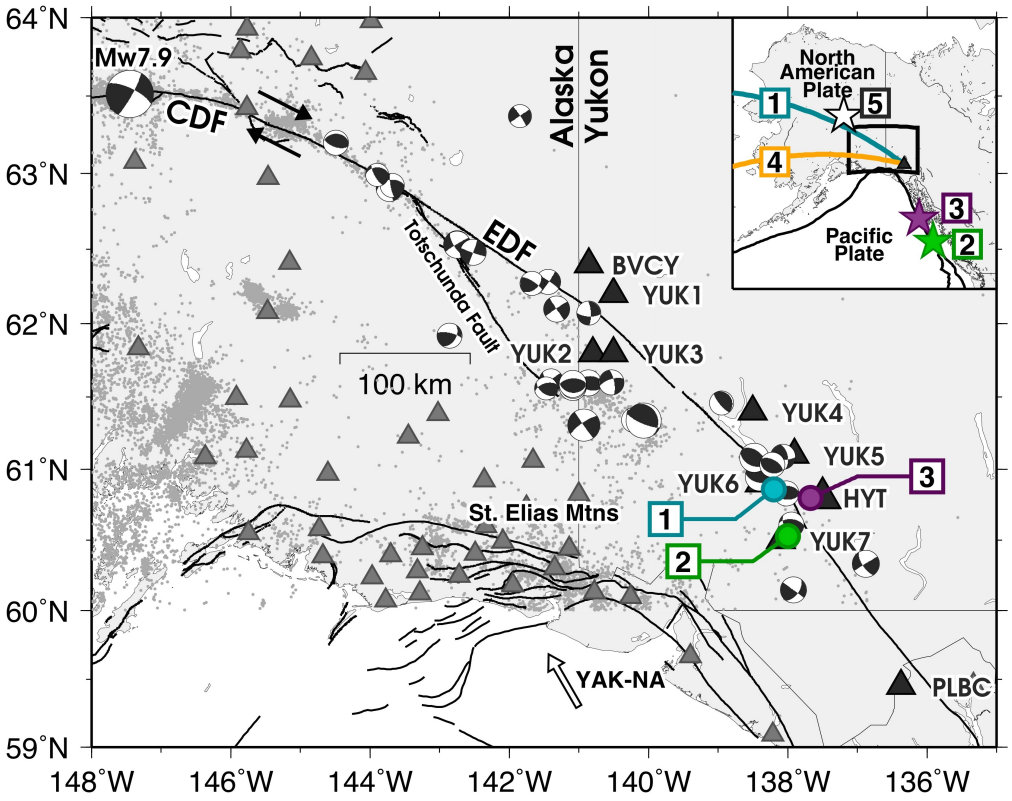

Figure 3.5 - Map view of study region. Black lines: fault traces. Gray dots: background seismicity during 2010-2013 from the ANSS earthquake catalog. Gray triangles: AK network stations. Black triangles: CN network stations. Focal mechanisms: moderate-size events (Mw > 3.8) occurring on or near the EDF since 1995 (see Table S3.3). Focal mechanism of the Mw7.9 Denali Fault earthquake is also marked. White arrow: relative Yakutat block – North American plate motion. Numbered circles: average location of tremor triggered by the Indian Ocean (1), Haida Gwaii (2), and Craig (3) earthquakes. *Inset:* Location of study region (black box) with the black triangle marking HYT station. Numbered lines: great circle path of the Indian Ocean (1) and Tohoku-Oki (4) earthquakes. Stars: locations of the Haida Gwaii (2), Craig (3), and Nenana (5) earthquakes.

3.3.2 Analysis and Procedure

Our analysis procedure generally follows that of *Aiken et al.* [2013a] previously detailed in Section 3.2.2 and is briefly described here. First, we searched the Advanced National Seismic System (ANSS) catalog for distant earthquakes that occurred between August 2010 and May 2013 and had magnitude $M \geq 5.5$, depth ≤ 100 km, and an

epicentral distance ≥ 100 km from station HYT. We select shallow, large magnitude earthquakes because these events generate large amplitude surface waves capable of triggering seismic activity on critically stressed faults. We also choose earthquakes over 100 km from the study region so that the triggered seismic activity we are searching for is not obscured by body wave coda. Using these parameters, we identified 1,369 distant earthquakes. Next, we estimated the dynamic stress of each selected earthquake at station HYT using a surface-wave magnitude M_s relationship [*van der Elst and Brodsky*, 2010; *Aiken et al.*, 2013a] (see Appendix A). The surface-wave magnitude M_s relationship assumes that the magnitude listed in the ANSS catalog is equivalent to M_s. Because earthquakes that generate > 1 kPa of dynamic stress are known to have triggered tremor in other transform environments [*Guilhem et al.*, 2010], we used this threshold to reduce the selected earthquakes from 1,369 to 19 events (Table S3.4).

After identifying earthquakes of interest, we obtained 12 hours of seismic data around the origin time of the distant earthquakes from the nine CNSN broadband stations. We removed the instrument response and rotated the horizontal components to the great circle path (radial) and a 90° clockwise rotation direction (transverse). The rotation was performed using the "rotate to GCP" command in Seismic Analysis Code with a normal polarity, which is based on a left-handed coordinate system, with vertical up, radial away from the source, and the left face of the transverse component along the positive radial component. For seismic data without clipped or poorly recorded data, we applied two band-pass filters (1-10 Hz, 5-15 Hz) to events that occurred > 1,000 km away to detect locally triggered activity and to avoid aftershock P-wave contamination. For events that occurred at distances < 1,000 km, we applied a high-pass (> 20 Hz) filter [*Guilhem et al.*,

2010] to avoid contaminating *P*-wave and *S*-wave signals of the mainshock and its early aftershocks (e.g., Figure 3.6). Finally, we visually inspected the filtered three-component data for seismic events triggered by surface waves of the distant earthquakes. We characterized long-duration (> 10 s) triggered tremor as emergent signals with no discernible *P/S* arrivals that are modulated by surface waves of distant earthquakes (Sections 3.3.3.1). In contrast, we characterized short-duration (< 5 s) triggered seismic events as bursts with sometimes sharp, distinguishable peaks that are modulated by surface waves of distant earthquakes (Section 3.3.3.2). We also compared the occurrence times of short-duration events with the ANSS catalog and the Natural Resources Canada (NRCan) earthquake catalog to check whether the short-duration events were local earthquakes.

If the triggered tremor was visible on at least three stations, we determined the location of the tremor bursts using an envelope cross-correlation method [*Chao et al.*, 2013]. For each station that recorded triggered tremor, we calculated the envelope of the filtered radial, transverse and vertical components, and then stacked and divided by three to create an averaged envelope function. From the averaged envelopes, we manually identified peaks of each tremor burst and then cross-correlated the envelopes to compute travel time differences between events and station pairs based on these picks. Using a simple two layer *S*-wave velocity model (Table S3.5) for this region [*Meighan et al.*, 2013], we computed the location of each tremor burst based on the minimum travel time residual for all possible station pairs. Because depth is not well constrained in the envelope cross-correlation method, we set the depth to be 25 km, a depth similar to previous studies of tremor on strike-slip faults [e.g., *Shelly*, 2009]. With our envelope

cross-correlation method, epicentral locations of the sources change only by ~5 km when focal depth is varied from 0-25 km.

3.3.3 Triggering Observations

3.3.3.1 Tectonic Tremor

For the 19 earthquakes examined in this study, we identified four (two clear, two possible) instances of tremor triggered by distant earthquakes (Table 3.1). Figure 3.6 is an example of tremor triggered by the 28 October 2012 *Mw*7.8 Haida Gwaii earthquake. The mainshock occurred relatively close to the EDF region (~960 km), so the amplitudes and frequency contents of the *P*-wave from the mainshock and its coda were quite high compared to other more distant events. Therefore, we applied a high-pass (> 20 Hz) filter to reveal local tremor signals, similar to *Guilhem et al.* [2010]. We found more than 10 tremor bursts at station HYT that occurred during the large-amplitude, long-period surface waves. These bursts have relatively long-duration (>10 s) and show no clear *P*/*S* arrivals, similar to triggered tremor observed in other tectonic settings [*Peng and Gomberg*, 2010]. A link to the corresponding animation with sound is provided in Section 3.3.7 (Movie S3.1).

Table 3.1 - Event information for triggering earthquakes.*

Date	Origin Time	Magnitude	Epicentral Distance (km)	Back Azimuth (degree)	Transverse PGV (cm s^{-1})	Vertical PGV (cm s^{-1})
March 11, 2011	05:46:24	9.0	5876	283	0.213	0.249 †
April 11, 2012	08:38:37	8.6	11790	307	0.195	0.079 †
October 28, 2012	03:04:09	7.7	953	157	1.090	1.310 ‡
January 5, 2013	08:58:19	7.5	626	163	2.500	1.570 ‡

*Distance, back-azimuth, and peak ground velocity (PGV) measured at station HYT.
†Possible triggering
‡Clear triggering

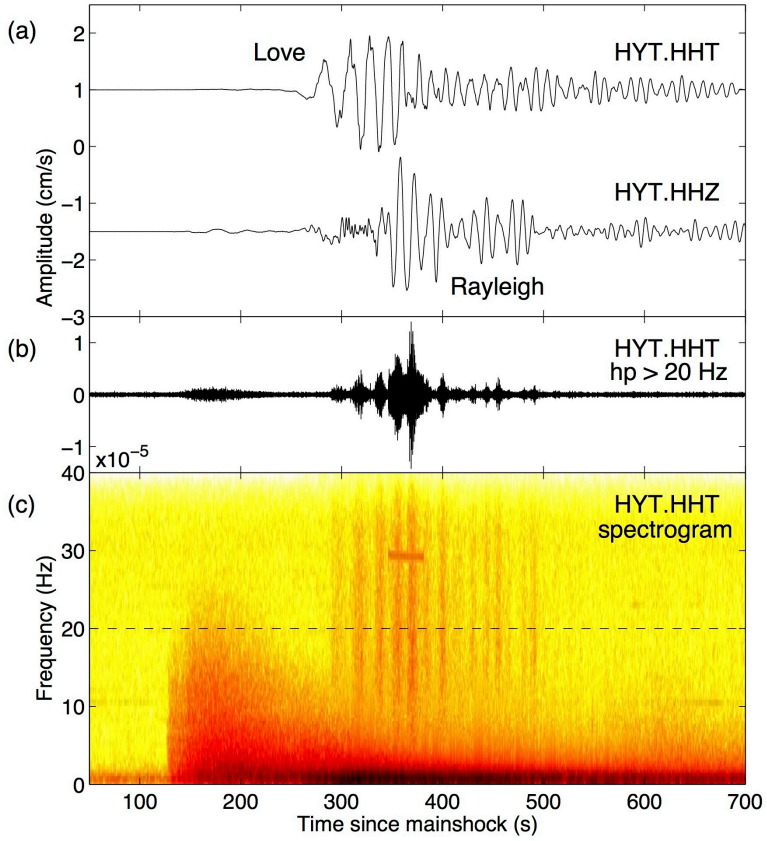

Figure 3.6 - Tremor triggered by the Haida Gwaii earthquake as recorded by station HYT. **(a)** Instrument-corrected broadband transverse (HHT) and vertical (HHZ) components. **(b)** High-pass filtered > 20 Hz transverse component. **(c)** Spectrogram. Dashed line: 20 Hz corner frequency used in the high-pass filter to remove the *P* and coda waves from the distant mainshock. The narrow frequency band near 30 Hz recorded from roughly 350 to 375 seconds after the mainshock could possibly be either instrumental or local noise. This same frequency band is recorded periodically and has the same duration throughout the 12-hour waveform retrieved for analysis.

Tremor occurred both during the Love and Rayleigh waves of the Haida Gwaii mainshock. For tremor triggered by the Love wave (~260-380 s after the mainshock), the bursts are clearly visible on stations HYT, YUK5, and YUK6 (Figure 3.7a). The average location for this tremor source appears to be near station YUK7 (Figure 3.5), but only short-duration (< 5 s) bursts (further examined in a later section) were visible at that station (Figure 3.7). No small magnitude local earthquakes were listed in the ANSS or NRCan catalogs during this time. We time-shifted the waveforms to our tremor location using the velocity model of *Meighan et al*. [2013] and phase velocities of the Love and Rayleigh waves to visualize how triggering occurs at the tremor source. After time-shifting the waveforms back to the tremor source, we find that these tremor bursts are coincident with Love wave velocity peaks, with the highest triggered tremor amplitude occurring around the onset of the large amplitude (velocity) Rayleigh wave (Figure 3.7b). Unfortunately, tremor triggered by the subsequent Rayleigh wave was only visible on the HYT station. Therefore, we were not able to locate those tremor sources.

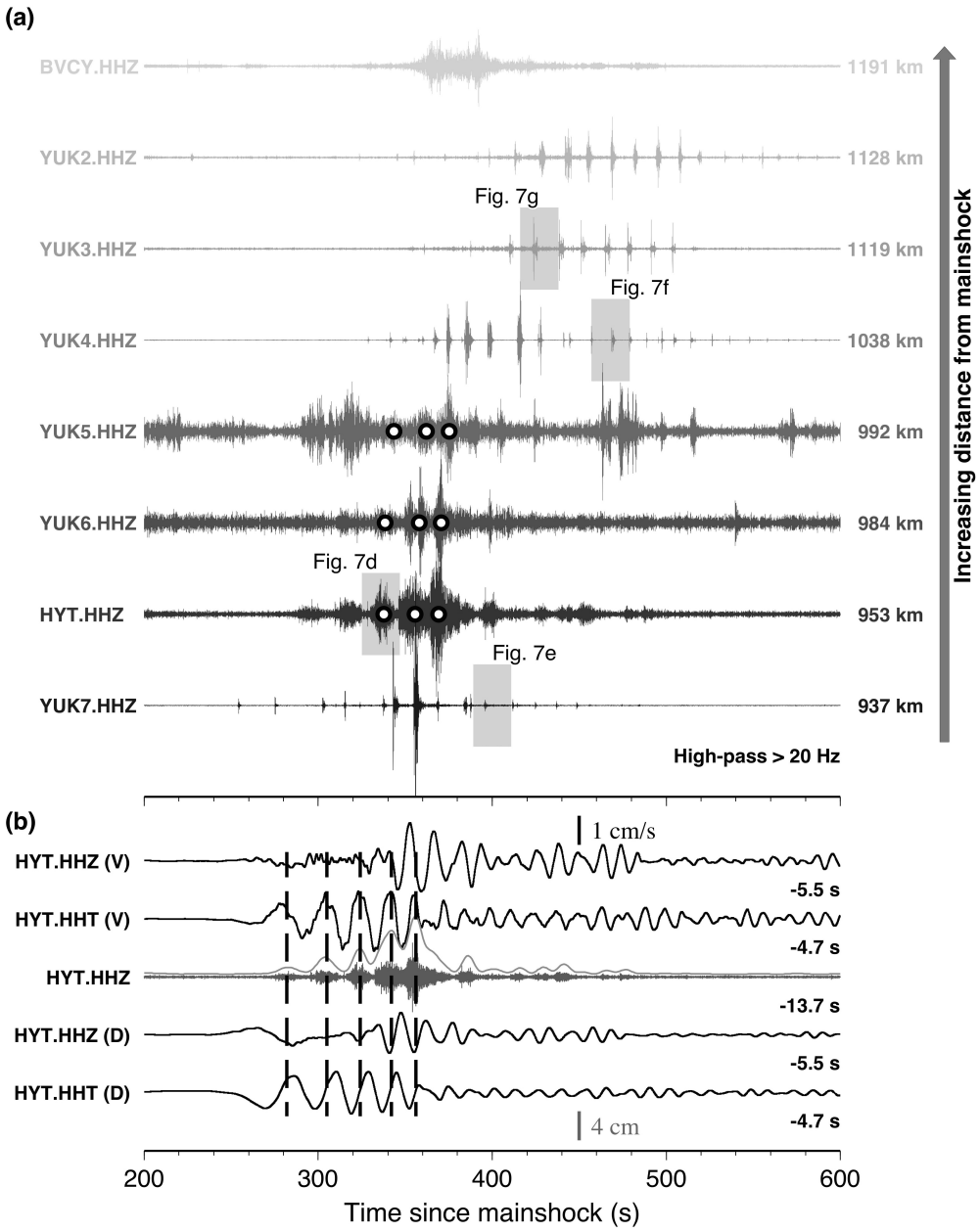

Figure 3.7 - Example of tremor and short-duration seismic events triggered by the Haida Gwaii earthquake. **(a)** 20 Hz high-pass filtered vertical (HHZ) waveforms at multiple stations. Circles: tremor phase picks used for location. Epicentral distance from the station to the tremor source is indicated. Gray boxes: examples shown in Figure 3.11. **(b)** Transverse (HHT) and vertical (HHZ) component velocity (V) and displacement (D) waveforms recorded at the HYT station with 20 Hz high-passed filtered waveform and envelope function. Waveforms are time-shifted to the average tremor source location. Dashed lines: peaks of the tremor bursts (based on the envelope function) and show their correlation with the surface waves. Black vertical bar: scale for broadband velocity waveforms. Gray vertical bar: scale for broadband displacement waveforms.

Figure 3.8 shows tremor triggered by the 5 January 2013 *Mw*7.5 Craig earthquake that occurred ~630 km away. Similar to the previous case (Figure 3.6), we applied a 20 Hz high-pass filter to broadband waveforms to identify locally triggered activity (Figure S3.5). Tremor is observed at station HYT during the Love and Rayleigh waves of the Craig mainshock. These tremor signals were also observable on stations YUK5 and YUK6, but the tremor signals can be seen most clearly on station HYT (Figure 3.8a). Unfortunately, there is no clear correlation of all tremor bursts among the three waveforms, and two earthquake-like bursts occurred immediately following the tremors (as seen on station YUK6). The first tremor burst, which occurred around 175 s, is located to be near the HYT station (Figure 3.5). By time-shifting the waveforms, the first 2 tremor bursts correlate well with Love wave velocity peaks (transverse component) generated by the Craig mainshock (Figure 3.8b).

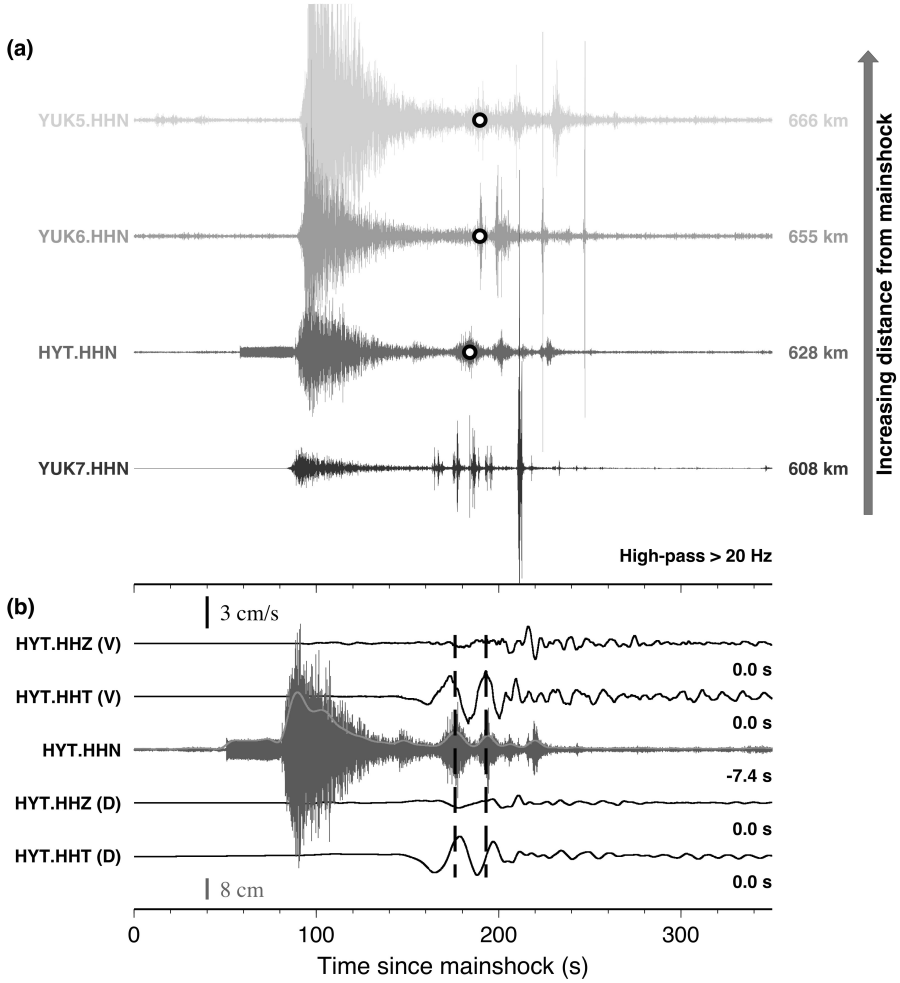

Figure 3.8 - Example of tremor triggered by the Craig, Alaska earthquake. **(a)** 20 Hz high-pass filtered waveforms at multiple stations. **(b)** Transverse (HHT) and vertical (HHZ) component velocity (V) and displacement (D) waveforms recorded at the HYT station with 20 Hz high-passed filtered waveform and envelope function. Symbols and notation are the same as in Figure 3.7.

We also observed tremor possibly triggered by two more remote earthquakes (Table 3.1). The first case is the 11 March 2011 *Mw*9.0 Tohoku-Oki earthquake recorded by the YUK1 and YUK3 stations (Figure 3.9). We filtered these recordings at the frequency range of 5-15 Hz, to avoid potential contaminations of the *P*-waves of early aftershocks. Most of the stations appear to be noisy, but tremor triggered by the Rayleigh wave of the Tohoku-Oki mainshock can be seen on stations YUK1 and YUK3 near the

United States-Canada border. Since these coherent tremor signals were observable on only two stations, we were not able to locate their sources. However, the tremor source must lie close to the YUK3 station due to its earlier arrivals. The tremor is arguably near the fault trace since a similar coherent signal was not observable on station YUK2, which is farther from the fault trace.

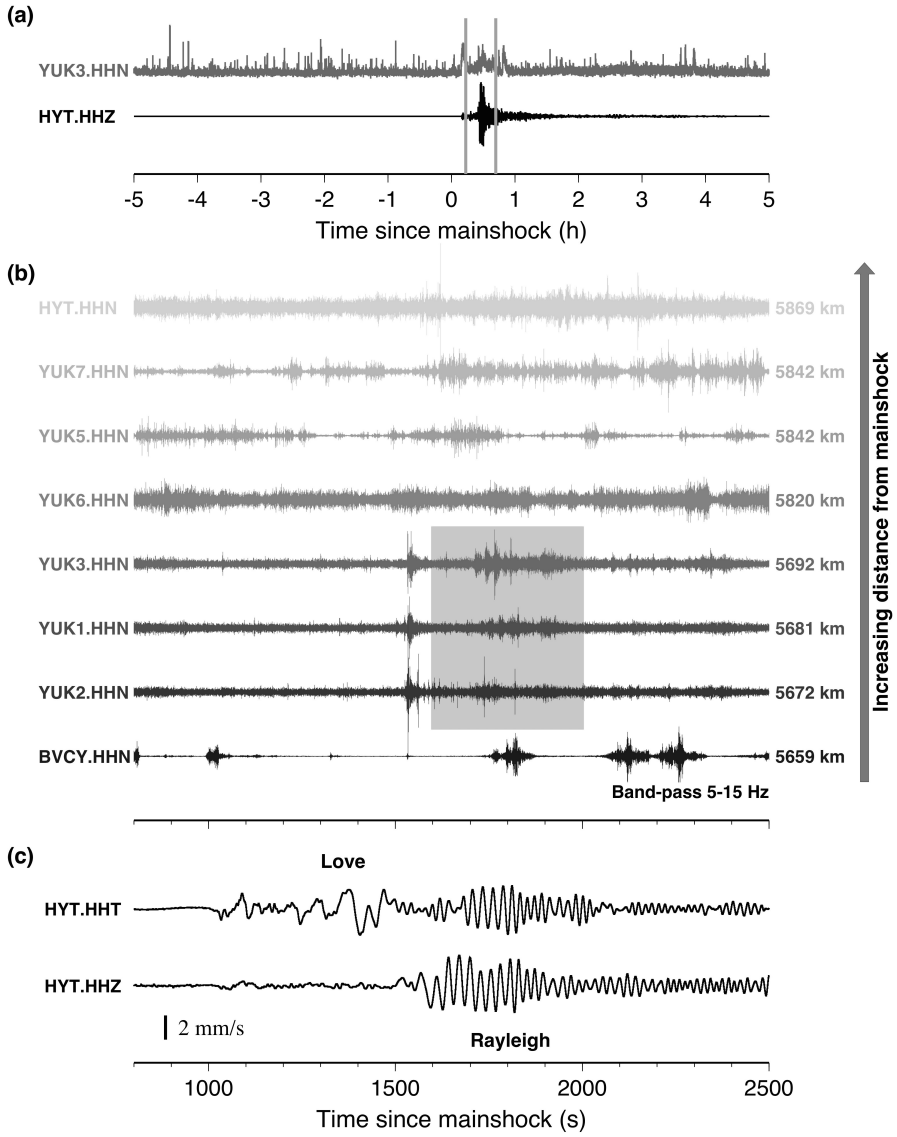

Figure 3.9 - Example of tremor triggered by the Tohoku-Oki earthquake. **(a)** Comparison between broadband and 5-15 Hz band-pass filtered envelope. Vertical lines: time window in (b)-(c). **(b)** 5-15 Hz band-pass filtered north (HHN) component waveforms recorded at all stations, order from most southern station YUK7 to most northern station BVCY.

Triggered tremor appears on stations YUK1, YUK2, and YUK3 during the Rayleigh waves. **(c)** Broadband transverse (HHT) and vertical (HHZ) components recorded at station HYT. Symbols and notation are the same as in Figure 3.7.

The second case is the 11 April 2012 *Mw*8.6 Indian Ocean earthquake recorded by stations YUK5, YUK7, and HYT stations (Figure 3.10). The Indian Ocean mainshock has triggered many microearthquakes and tremor around the world [e.g. *Wu et al.*, 2012], as well as a transient global increase of $Mw \geq 5.5$ earthquakes [*Pollitz et al.,* 2012]. Its Love wave also triggered a *Mw*3.9 earthquake in central Alaska [*Tape et al.*, 2013], which was recorded by stations in our study region at ~2700 s after the Indian Ocean mainshock. We observed consecutive bursts of tectonic tremor triggered by the long-period Rayleigh wave between 3500 and 4000 s after the Indian Ocean mainshock in the 1-10 Hz frequency band (Figure 3.10). The seismic waves of the *Mw*3.9 Nenana earthquake arrived in our study region around the arrival of the Love wave of the Indian Ocean mainshock, and thus we were not able to detect tremor triggered during the Love wave strictly by visual inspection of the waveforms. We examined the spectrogram of the Indian Ocean mainshock but found no evidence of triggered tremor signals during this time in a higher frequency band (Figure S3.6). We also compared the predicted Nenana earthquake *S*-wave amplitude attenuation with measurements at seismic stations along the ray path but did not find any increase in the amplitude due any additional local seismic source (Figure S3.7).

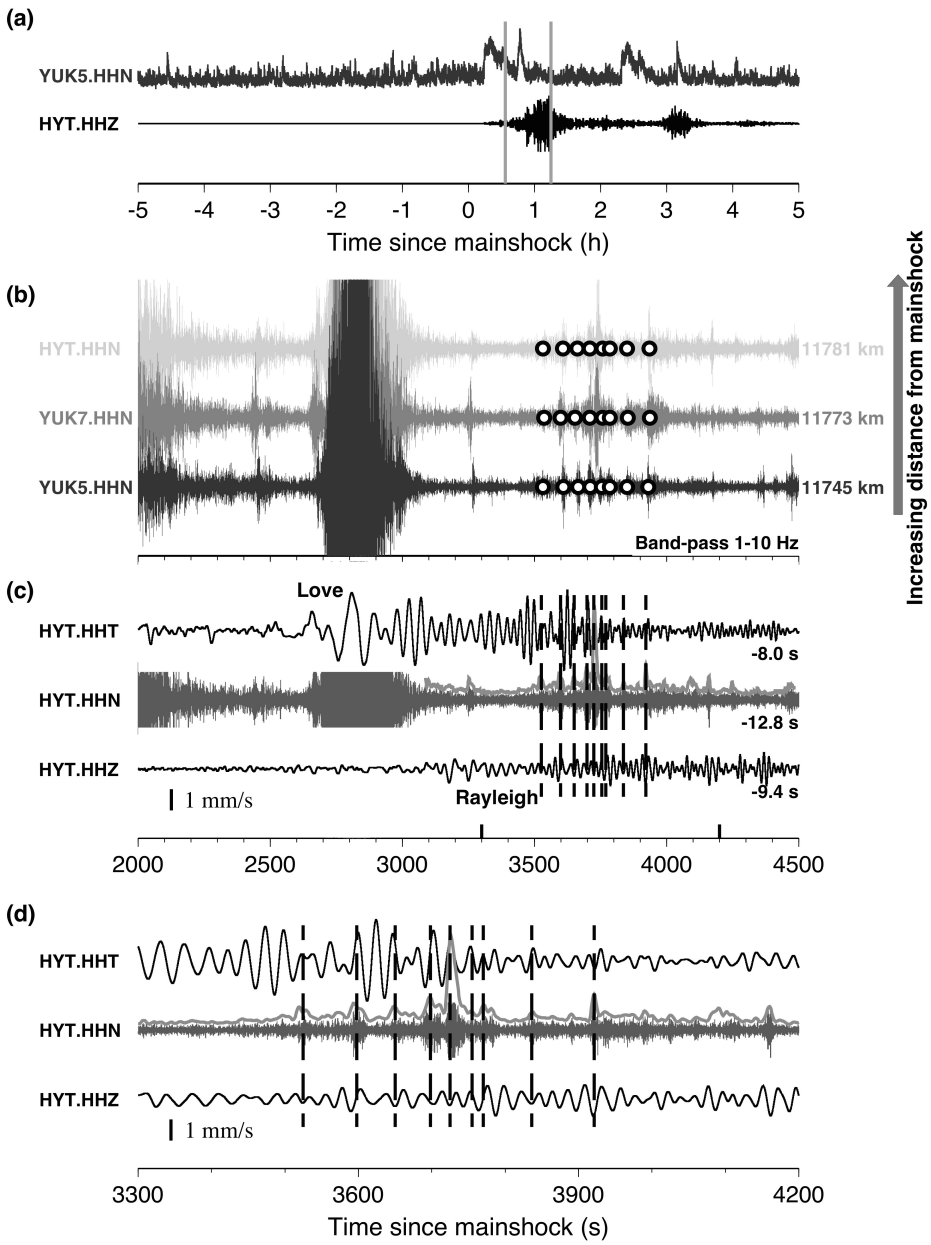

Figure 3.10 - Example of tremor triggered by the Indian Ocean mainshock. **(a)** Comparison between broadband and 1-10 Hz band-pass filtered envelope. Vertical lines: time window in (b)-(c). **(b)** 1-10 Hz band-pass filtered waveforms from multiple stations. **(c)** Transverse (HHT) and vertical (HHZ) component waveforms recorded at station HYT with 20 Hz high-pass filtered waveform and envelope. The filtered waveform is intentionally clipped so that weak tremor signals can be shown. **(d)** Zoom-in to show correlation between tremor bursts and surface wave peaks. Symbols and notation are the same as in Figure 3.7.

We located the tremor sources triggered during the Rayleigh wave to be near the YUK6 station, for which no data was available. However, after time-shifting to this location, these tremor bursts do not show consistent correlation during coda of the Love and Rayleigh waves on either the vertical or the transverse component of the broadband data. We did not observe tremor triggered by the *Mw*8.2 aftershock, which occurred ~2 hours after the *Mw*8.6 mainshock, despite having a similar focal mechanism and occurring at similar epicentral distance (Figure S3.8).

3.3.3.2 Other Seismic Phenomena

In addition to triggered tremor signals, we identified 3 distinct episodes of short-duration seismic events triggered primarily by Rayleigh waves of the Haida Gwaii earthquake. In comparison to the long-duration triggered tremor, these brittle events produced short-duration (< 5 s) signals and can be distinguished from tremor when converted to audio due to differences in their duration and power in higher frequencies (see Movies S3.1-S3.2 linked in Section 3.3.7.4). *Peng et al.* [2012] presented a similar analysis for distinguishing triggered events of the 2011 Tohoku-Oki mainshock by converting the seismic signals into audible sounds. One episode of short-duration triggered seismic events was recorded at station YUK7 (Figures 3.7 and 3.11a). At this station, nine consecutive short-duration events coincide with peaks of Rayleigh wave displacement. A few occurred during the Love waves, but they did not show temporal correlations with the Love wave velocity peaks. However, this could potentially be a result of propagation delays from the triggered source to the YUK7 station. We also note that the two larger amplitude short-duration events occurred during the first and largest two cycles of the Rayleigh wave.

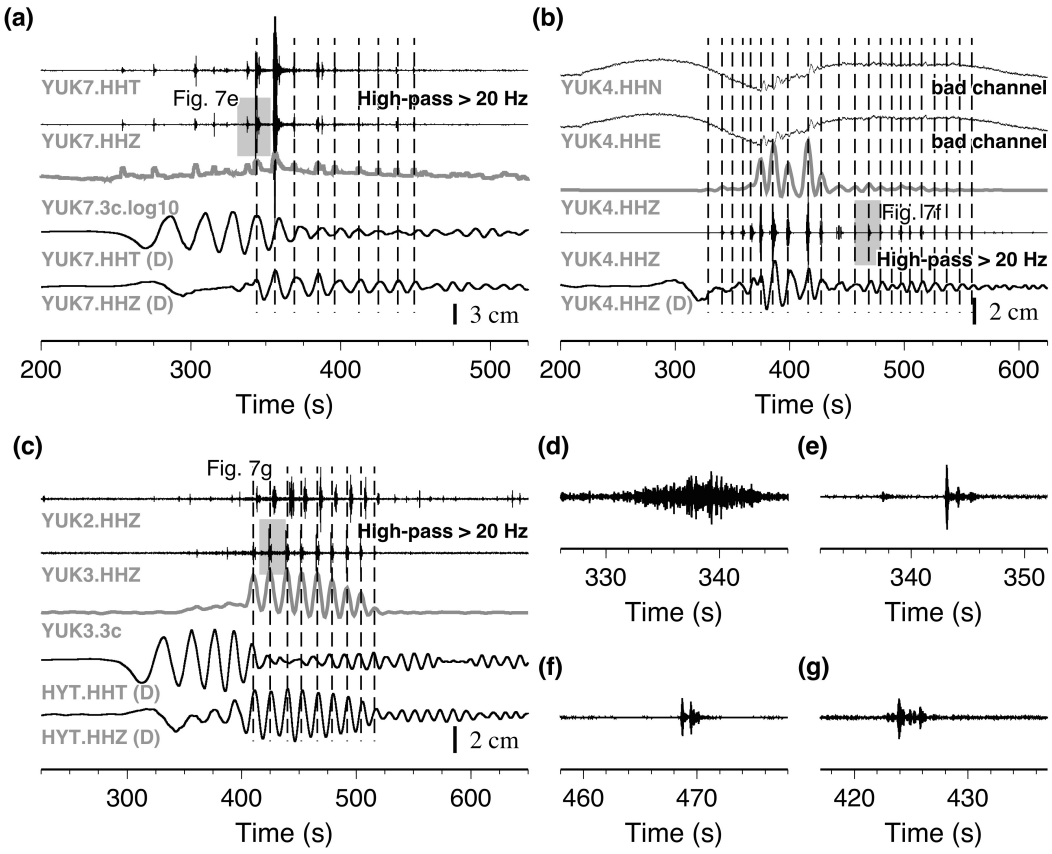

Figure 3.11 - Example of short-duration seismic events triggered by the Haida Gwaii earthquake. **(a)** Seismic activity recorded on station YUK7 on the southern end of the EDF. Top three traces show the 20 Hz high-pass filtered velocity seismograms and an envelope function (log10). Bottom two traces show the broadband transverse (HHT) and vertical (HHZ) displacement waveforms. Dashed lines: event peaks (based on envelope function). Amplitude scale indicated. **(b)** Seismic activity recorded on station YUK4 near the middle of the EDF. Traces are plotted in the same way as in (a), except that the envelope is in linear scale. Top two traces show poorly recorded horizontal channels. **(c)** Seismic activity recorded on stations YUK2 and YUK3 on the northern end of the EDF. **(d)** Tremor triggered near the southern end of the EDF. **(e)-(g)** Short-duration events triggered near the southern, middle, and northern portions of the EDF. Time windows are marked by gray boxes in (a)-(c) of this figure, as well as in Figure 3.7.

Figure 3.11b is the second example of short-duration seismic events triggered by the large amplitude Rayleigh wave starting at ~375 s, as observed on the YUK4 station located near the middle of the EDF in the Yukon territory. Five larger amplitude short-duration events occurred during the higher Rayleigh wave amplitudes, and several smaller short-duration events occurred just prior to (5 events) and just after the higher

Rayleigh wave amplitudes (12 events). Short-duration seismic events occurring after 375 s appear to be phase-related to the vertical component of the Rayleigh wave displacement, though we could only observe this correlation on that component due to significant instrumental noise on the horizontal components. Because this station is rather distant from the northern and southern cluster of stations (Figure 3.5), it is clear that these short-duration seismic events represent a different source from those observed on the southern YUK7 station. Similarly, we were not able to locate the short-duration seismic sources because these signals were only observable on the YUK4 station.

A final example of short-duration triggered events is shown in Figure 3.11c. Between 400-525 s, we identified short-duration signals visible on stations YUK2 and YUK3 located further north near the United States-Canada border. Specifically, we found 9 consecutive short-duration events (< 5 s) occurring during the Rayleigh waves, which are phase-correlated with the Rayleigh wave displacement (see Movie S3.2 linked in Section 3.3.7.4). These short-duration brittle events were recorded at station YUK3 ~3 seconds earlier than at station YUK2, indicating that their source is likely closer to station YUK3. Availability of only two stations limits our ability to ascertain an accurate location. However, the combination of Rayleigh wave polarization analysis and simple geometry (Section 3.3.7.1) suggests that the source may be south-southwest of station YUK3, near the Klutlan Glacier terminus (Figures S3.9-S3.10). These short-duration brittle events have similar characteristics to glacial tectonic sources (i.e., icequakes) detected in Antarctica that were also triggered primarily during Rayleigh waves of the 27 February 2010 *Mw*8.8 Chile earthquake [*Peng et al.*, 2014]. Furthermore, recent evidence suggests that Alaska network seismic analysts routinely identify glacial events in this

region, which are characterized by regionally observed signals deficient in high-frequency energy (higher than 3-5 Hz) [*West*, 2014]. However, in this region, there also exists significant ambient tectonic seismicity at the Canadian eastern extension of the Totschunda-Duke River Fault (Figures 3.5 and S3.10). We found no local earthquakes listed in the ANSS or NRCan earthquake catalogs that coincided with the occurrence times of any of these triggered short-duration seismic event episodes, and the region was relatively quiescent prior to the arrival of the surface waves (Figure S3.11). Despite the limited quality of data and paucity of stations, our Rayleigh wave polarization analysis and local seismic activity suggests the signals represent either small, shallow tectonic earthquakes or icequakes in the near surface.

3.3.4 Characteristics of Triggering Waves

Similar to previous studies [*Aiken et al.*, 2013a], we analyzed the peak ground velocities (PGVs), seismic wave incidence angles, and amplitude spectra of all earthquakes examined in this study to determine factors that promote triggering. When examining PGVs, we estimated the maximum dynamic stress each earthquake produced by

$$\sigma = \frac{(\mathrm{PGV})(\mu)}{\mathrm{v_{ph}}}. \tag{3.1}$$

where σ is estimated dynamic stress, μ is an assumed crustal shear rigidity of 30 GPa, *PGV* is peak ground velocity (PGV) measured from each earthquake's waveform, and v_{ph} is an assumed Love wave phase velocity of 4.1 km s^{-1}. Figure 3.12a shows dynamic stress σ computed from the measured PGVs of the instrument-corrected transverse component at station HYT as a function of back-azimuth for each event (i.e., wave incidence angle

on the EDF). To avoid contamination of the PGV measurement by local seismic activity, we applied a 1-s low-pass filter to the waveforms prior to measuring the PGV. We also examined the surface wave amplitude spectra for each earthquake in our study (Figure 3.12b). We cut the seismic data between the 5 km s^{-1} and 2 km s^{-1} arrivals to capture the surface wave energy and then computed the Fast Fourier Transform (FFT). Finally, these data were smoothed with a 5-point sliding window [*Peng et al.*, 2009].

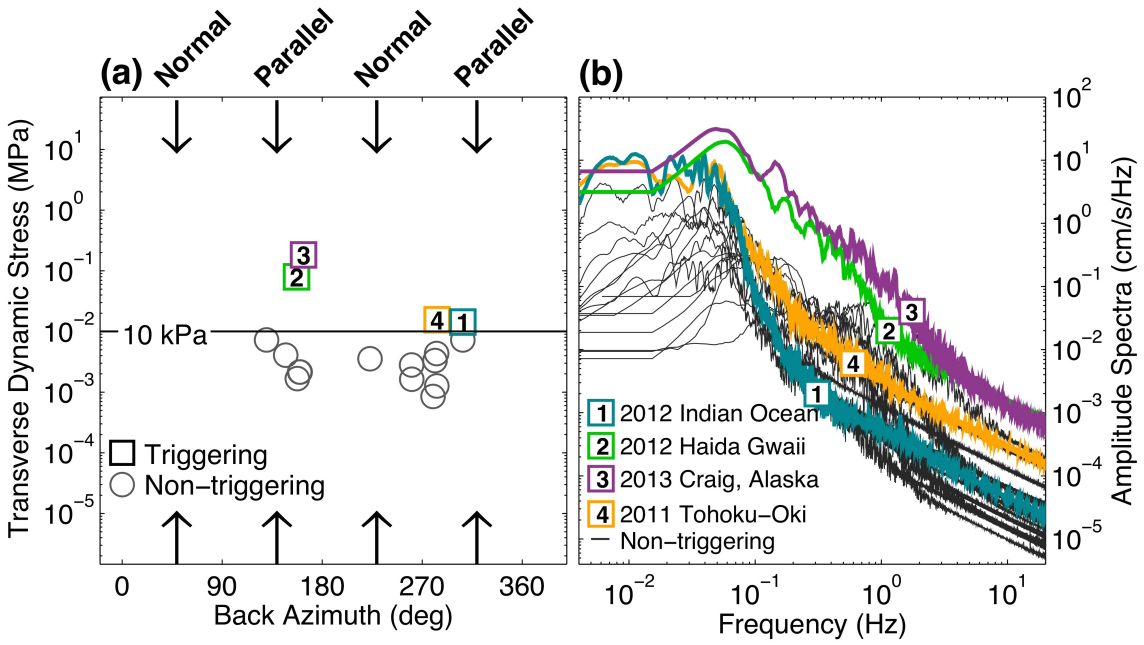

Figure 3.12 - Triggering potential (dynamic stress, wave incidence angle, and frequency dependence) of distant earthquakes. **(a)** Transverse dynamic stress versus back-azimuth for all earthquakes examined in this study. Squares: triggering and possibly triggering earthquakes. Circles: non-triggering earthquakes. Arrows indicate normal and parallel wave incidence on the fault. **(b)** Transverse velocity amplitude spectra for all earthquakes examined. Thin lines: non-triggering earthquakes. Thick numbered lines: triggering earthquakes. Number indicates event name and corresponds to the tremor locations in Figure 3.5 and squares in part (a) of this figure.

From our analysis of PGVs, wave incidence angle, and amplitude spectra, we find that large-amplitude (> 10 kPa), long-period (> 20 s) surface waves are responsible for triggering tremor and brittle seismic events along the EDF. We note that the 2012 Haida

Gwaii and 2013 Craig earthquakes triggered clear tremor with both the Love and Rayleigh waves, while we possibly observed tremors triggered by the Rayleigh wave for the more distant 2011 Tohoku-Oki and 2012 Indian Ocean earthquakes. In addition, it is notable that 2012 Haida Gwaii and 2013 Craig earthquakes exhibit similar amplitude spectra and dynamic stress, but only the 2012 Haida Gwaii earthquake triggered short-duration seismic events.

3.3.5 Discussion and Conclusions

In *Aiken et al.* [2015b], we provided clear evidence of surface waves triggering tremor along the EDF. Tremor sources with durations (> 10 s) appear to be localized in the southern cluster of CNSN stations on either side of the fault near the epicenters of moderate-sized earthquakes (Figure 3.5) and possibly near the northern cluster of stations (Figure 3.9). In comparison, short-duration (< 5 s) seismic events – signals with sharp peaks - triggered only by the Haida Gwaii mainshock were recorded by several stations in the northern (stations YUK2 and YUK3), middle (station YUK4), and southern (station YUK7) portions of the EDF in the Yukon territory (Figures 3.5 and 3.11). Because fewer than three stations recorded these signals, we were unable to locate these sources. However, short-duration seismic events recorded by stations YUK2 and YUK3 appear to radiate from the vicinity of on-going seismicity occurs along the eastern extension of the Totschunda Fault, as well as near the Klutlan Glacier terminus (Figure S3.10).

Triggered tremor has been observed along several strike-slip faults in the Western Hemisphere (Figure 3.13). It is evident that tremor triggered along the EDF has characteristics similar to that of tremor triggered in other regions [*Peng and Gomberg*, 2010; *Guilhem et al.*, 2010]. That is, they contain relatively long-duration (> 10 s) signals

with no clear *P*/*S* wave arrivals and are coincident with Love and Rayleigh wave peaks. We observed tremor triggered primarily by the Love wave of the Haida Gwaii (Figures 3.6 and 3.7) and Craig earthquakes (Figure 3.8) with both events generating surface waves with near strike-parallel incidence. This is consistent with the Coulomb triggering model - maximum left-lateral shear stress induced by a Love wave with strike-parallel incidence on a vertical strike-slip fault [*Hill*, 2012]. In contrast, it appears that tremor was triggered by only the Rayleigh wave for the Tohoku-Oki (Figure 3.9) and Indian Ocean (Figure 3.10) mainshocks, even though Love wave triggering is also predicted by the Coulomb triggering model because the waves from both earthquakes have near strike-parallel incidence on the EDF [*Hill*, 2012]. Specifically for the Indian Ocean mainshock, we could not confirm Love wave triggering visually due to overlapping seismic waves from the triggered *Mw*3.9 Nenana earthquake in central Alaska [*Tape et al.*, 2013]. Nor could we identify evidence for triggered tremor in a higher frequency band (Figure S3.6) or from comparisons of the predicted Nenana earthquake *S*-wave amplitude attenuation with measurements at seismic stations along the ray path (Figure S3.7).

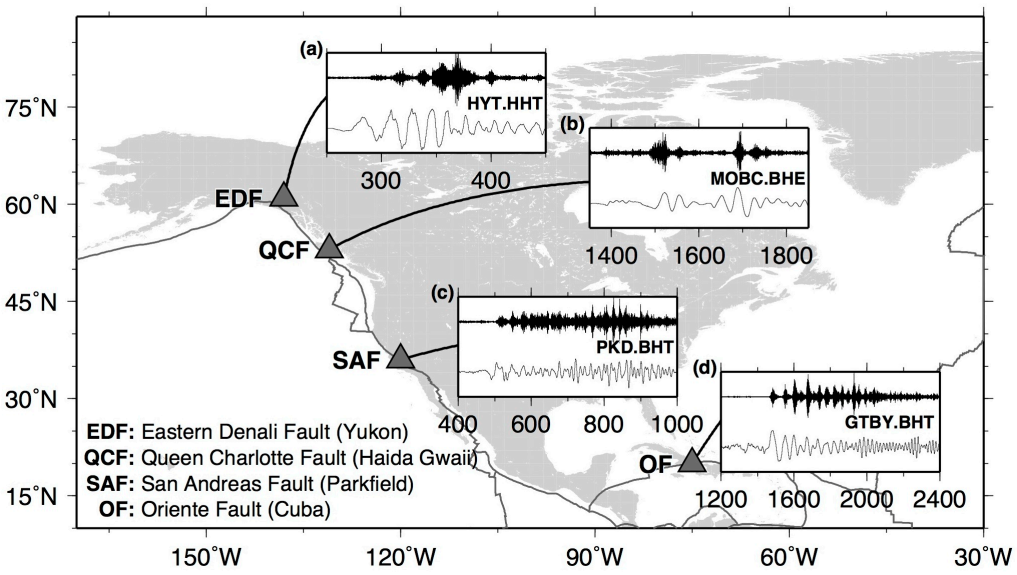

Figure 3.13 - Comparison of triggered tremor observations along 4 strike-slip faults. Each small panel shows surface waves of an earthquake (broadband) and of triggered tremor (filtered) with station and component marked. Triangles: station where earthquake and tremor was recorded. Gray lines: plate boundaries. **(a)** 2012 Haida Gwaii, Canada. **(b)** 2011 Tohoku-Oki, Japan. **(c)** 2012 Haida Gwaii, Canada. **(d)** 2010 Maule, Chile.

One may argue that the plate structure in this region is complex and that the triggered tremor could be radiating from the subduction interface rather than the Denali Fault (Figure 3.5). Recent studies have detected ambient and triggered tremor in south-central mainland Alaska [*Peterson and Christenson*, 2009; *Gomberg and Prejean*, 2013]. The tremor discovered in those studies lie where the Yakutat terrane is transitioning from flat-slab subduction in the west to a zone of collision in the east, resulting in a fold-thrust belt [*Worthington et al.*, 2012]. This region is more than 300 km away from where we observed triggered tremor in the southern portion of the EDF in the Yukon territory, and thus the low-amplitude tremor signals we observed cannot be radiating from this part of the complex subduction zone. This does not rule out the possibility that the observed tremor signals may be nucleating from the fold-thrust belt responsible for the St. Elias orogeny. In this region, the strike of the thrust faults mostly trend east-west, as the strike-

slip Fairweather Fault system transitions to subduction to the west. In this case, triggering waves would have a near strike-normal incidence on the thrust faults. *Hill* [2012] demonstrated that tremor triggered on low-angle thrust faults best correlates with strike-normal incident Rayleigh wave displacements. However, we found that the triggered tremor best correlates with the Love wave particle velocity, rather than Rayleigh wave displacements from the Haida Gwaii and Craig earthquakes (e.g., Figures 3.7 and 3.8), which previous studies have also observed on a vertical strike-slip fault [*Peng et al.*, 2008; *Hill*, 2012]. Moreover, the distance to the fold-thrust belt is still >100 km, which is likely too far to generate low-amplitude tremor observed in this study. Given these observations, we surmise that Love wave displacement gradients with strike-parallel incidence induce shear stress changes on the EDF, resulting in small, shear-failure events we recognize here as tremor.

The four triggering earthquakes (two clear, two possible) produced the greatest dynamic stresses at longer periods (> 20 s) than non-triggering events (Figure 3.12b). While the time period of our study is limited to a few years, it appears that ~10 kPa of dynamic stress is needed to trigger tremor in this region. This triggering threshold is greater than that observed in Parkfield, CA (e.g., 1-3 kPa) [*Peng et al.*, 2009; *Guilhem et al.,* 2010] but similar to that observed along the Queen Charlotte margin near Haida Gwaii [*Aiken et al.*, 2013a]. Because these regions are similar tectonically, the triggering threshold may reflect the current strength of a fault, which likely varies over time. However, because station density is sparse in Haida Gwaii and surrounding the EDF and because the data at EDF are only available since 2010, it is possible that such a disparity

in observed triggering thresholds between transform/strike-slip regions simply reflects differences in data quality and/or data availability.

Finally, we computed the static stress changes on the EDF based on the finite fault source slip distribution from *Lay et al.* [2013] for the 2012 Haida Gwaii and 2013 Craig earthquakes considering their proximity to the region. The resulting static stress changes are less than 0.03 kPa (Figures S3.12-S3.13) - two orders less than the corresponding dynamic stress changes (10-100 kPa). This indicates that the dynamic stresses from the surface waves of the Haida Gwaii and Craig earthquakes are more likely to trigger the tremor and short-duration seismic events, rather than the much smaller static stress changes.

In comparison to the Love and Rayleigh wave triggering of tremor, the short-duration seismic events were primarily triggered by the Rayleigh wave of the Haida Gwaii earthquake (Figure 3.11). These short-duration seismic events occurred during the upward motion of the Rayleigh wave displacement when the dilatation is positive [*Miyazawa and Brodsky*, 2008; *Rubinstein et al.*, 2009]. One could argue that the triggered, short-duration signals reflect single, LFE events known to partially comprise tremor [e.g., *Shelly et al.*, 2007]. While both the triggered tremor and short-duration signals are brittle, shear-failure events, their particle motions differ. For example, the deep tremor signal is dominated by the *S*-waves of many LFE events. However, the short-duration signals we observed here behave more like Rayleigh waves (Figure S3.9). Also, while the tremor bursts and short-duration signals have similar frequency contents (up to 30-40 Hz), triggered tremor has weaker power in the higher frequencies over a longer duration (Movies S3.1-S3.2). Although we were unable to accurately locate these short-

duration sources, their waveform characteristics and similarity to Rayleigh waves allow us to identify the source as south-southwest of station YUK3 (Figure S3.10c), near the Klutlan Glacier terminus where there is also a historical record of shallow (< 10 km depth) seismicity and regional events flagged as "glacial events" by Alaska Earthquake Center analysts [*West*, 2014]. Due to the poor data quality, it is difficult to distinguish whether the sources are icequakes similar to those observed in Antarctica triggered by the *Mw*8.8 Chile earthquake [*Peng et al.*, 2014] or shallow earthquakes like those triggered near active volcanoes or geothermal regions [*Prejean et al.*, 2004; *West et al.*, 2005]. Deducing which type of events actually occurred – icequakes or shallow earthquakes - would require more stations in the region, which are not available at this stage.

Previous observations of triggered and ambient tremor in this region were primarily associated with the Alaska-Aleutian subduction zone [*Peterson and Christensen*, 2009; *Chao et al.,* 2013; *Brown et al.*, 2013]. *Gomberg et al.* [2012] also conducted a systematic search but did not find any precursory tremor signals before the 3 November 2002 *Mw*7.9 Denali Fault earthquake and in several time intervals after the mainshock. Permanent stations near the central Denali Fault are predominately located near the initial rupture point of the Denali Fault earthquake (e.g., Figure 1 of *Gomberg et al.* [2012]). We searched for tremor on stations surrounding the central Denali Fault, and the triggered tremor generally arrives at station KLU prior to PAX (Figure S3.14), suggesting that they mostly occur further south in the south-central Alaska sweet spot [*Chao et al.*, 2013; *Gomberg and Prejean*, 2013]. No tremor signal was observed on station DDM (seismic data archived for only 1 year, from 2009-2010), located north of the central Denali Fault. While we did not find any tremor signals radiating from the

central Denali Fault in this short time frame, tremor may still occur there. However, it is also possible that the tremor-generating conditions are different in our study region surrounding the EDF than the central Denali Fault where the *Mw*7.9 earthquake occurred. Nevertheless, our observation of triggered tremor along the EDF provides additional evidence of tremor occurring in strike-slip environments. It is important to continue investigating tremor activity along this intraplate fault in the hope that we can better understand the physical mechanisms responsible for not only tremor generation but also its role in the seismic cycle of large earthquakes along the EDF.

3.3.6 Data and Resources

The Advanced National Seismic System earthquake catalog is made available by the Northern California Earthquake Data Center via www.ncedc.org (last accessed June 2013). The Natural Resources of Canada earthquake catalog is available via http://www.earthquakescanada.nrcan.gc.ca/stndon/NEDB-BNDS/bull-eng.php (last accessed July 2013). Seismic waveforms and response files recorded by the CNSN are accessible by the IRIS Data Management Center via www.iris.edu (last accessed June 2013) and by the Natural Resources of Canada AutoDRM via http://www.earthquakescanada.nrcan.gc.ca/stndon/AutoDRM/autodrm_req-eng.php (last accessed January 2014). Focal mechanism data in Figure 3.5 and Table S3.3 was provided by Honn Kao at the Natural Resources Canada. Figures were made using Generic Mapping Tools version 4.5.1 (www.soest.hawaii.edu/gmt, Wessel and Smith, 1998) and proprietary MATLAB software version 7.11.0.584 (R2010b).

3.3.7 Supplemental Information

This section describes the Rayleigh wave polarization detection used for locating the triggered short-duration events triggered by the Haida Gwaii earthquake. It contains ten figures, three tables and two movies (referenced here and/or in previous sections).

3.3.7.1 Supplemental Text

We use a Rayleigh-wave polarization analysis [e.g., *Stachnik et al.*, 2012] to determine the nature of the triggered waves. It utilizes the property that Rayleigh waves exhibit retrograde elliptical particle motion [e.g., *Lay and Wallace*, 1995], when the horizontal components are aligned parallel the seismic source. In our case of an unknown receiver-to-source direction, Hilbert-transformed vertical component seismograms are correlated with rotated horizontal seismograms to directions parallel (radial) and perpendicular (transverse) to a hypothetical seismic source. This horizontal rotation is based on a right-handed coordinate system, with vertical up, radial pointing to the source, and the right face of the transverse component along the positive radial component. Here, we test all possible source/receiver azimuths (j=1:360). The normalized correlation coefficient reaches its maximum for that azimuth that is plausibly the actual receiver-to-source azimuth [*Stachnik et al.*, 2012]. Ideally, the coefficient is nearly 1 for surface waves and the method provides a means of evaluating whether ambiguous seismic signals are indeed surface waves and quantifies their approximate azimuth relative to the station.

We examine the continuous time series around the triggered events at station YUK3. We apply a 5 Hz high-pass filter to each station's seismograms and perform the analysis described above in windows of 2 s length that progresses through the data with a

1 s time-step (effectively a 50% overlap). At each time-step, we record the maximum correlation coefficient and the corresponding back-azimuth. When the correlation coefficient crosses a threshold of 0.45, we mark a red dot on the bottom panel (Figure S3.9). The moving-window polarization analysis for YUK3 indicates a southerly source during the discrete signals with 180-200° directional azimuth (from north). The collapse of azimuths near a single value also suggests a repeating or close by source for the triggered events. The same analysis on the YUK2 seismograms was inconclusive, perhaps due to complex site effects at the installation site.

Since the repeating events arrive at YUK3 first, we can make a crude estimation of the source location(s) relative to the two stations using simple geometry and the observed 180-200° directional azimuth from the Rayleigh wave polarization analysis (Figure S3.10c). Based on the repeating event arrival times, the distance between station YUK2 and the source must be longer than the distance between station YUK3 and the same source by a distance Δx, such that

$$\sqrt{(x_1 - x)^2 + (y_1 - y)^2} - \sqrt{(x_2 - x)^2 + (y_2 - y)^2} = \Delta x \qquad \text{(S3.1)}$$

where x, x_1, and x_2 are the longitudinal coordinates and y, y_1, and y_2 are the latitudinal coordinates of the source, station YUK2, and station YUK3, respectively. The distance Δx can be approximated using the time delay of ~3.5 seconds (Δt) between the stations (moveout) and an assumed Rayleigh wave nominal group velocity (v) of 3.1 km/s, since the polarization analysis suggests the observed short-duration signals are mostly Rayleigh waves. This gives $\Delta x = v\,\Delta t$ = 11 km. We then performed a grid search for all possible (x,y) pairs that result in Δx = 11 km and use our range of back-azimuths (180-200°) from

Rayleigh wave polarization analysis to find all possible short-duration event locations (Figure S3.10a).

Given the paucity of stations in the area, it is impossible to ascertain an accurate location for the triggered short-duration events. However, our analysis suggests that the source is south-southwest of station YUK3. The Klutlan Glacier terminus is near this point. The waveforms have similar characteristics to glacial tectonic sources (i.e., icequakes) detected in Antarctica that were also triggered during Rayleigh waves of distant earthquakes [*Peng et al.*, 2014]. Furthermore, icequakes are routinely recorded in this area, though these have not been studied in detail [*West*, 2014]. In addition to a possible glacial source, significant ambient tectonic seismicity follows the trace of the Toschunda-Duke River Fault. Thus, the data may indicate two possible sources, small shallow, tectonic earthquakes and/or icequake events. Deducing which type of events actually occurred would require more stations in the region.

3.3.7.2 Supplemental Figures

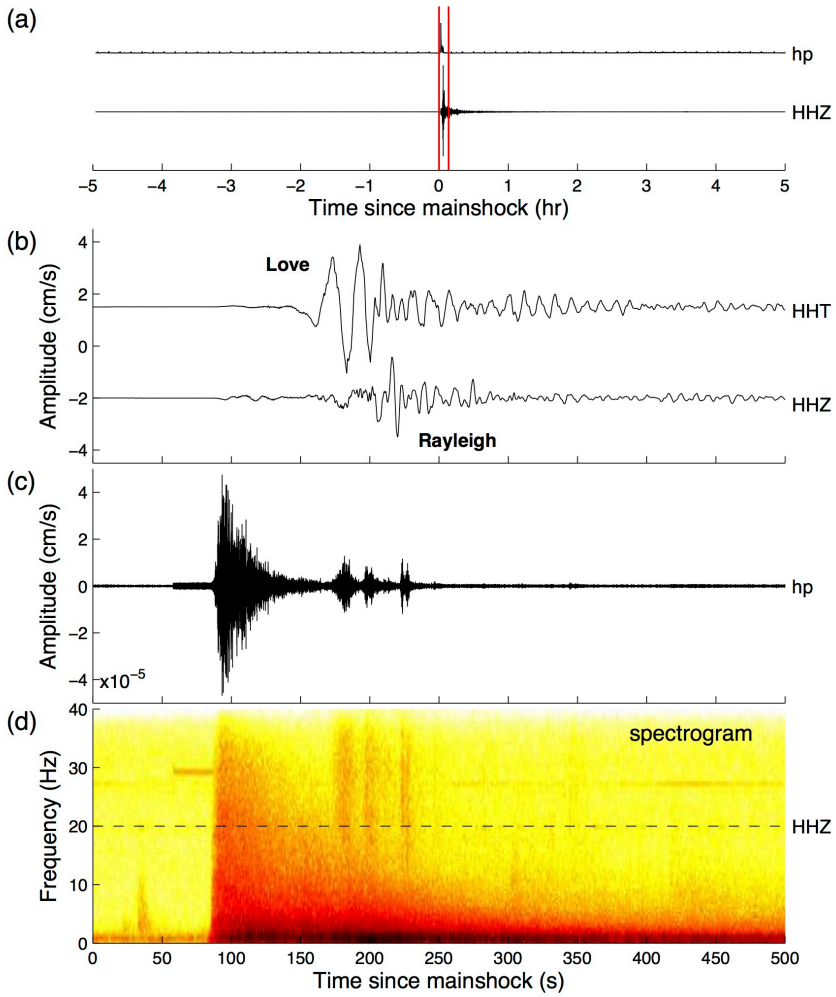

Figure S3.5 - Spectrogram of tremor triggered by the Craig earthquake as recorded by station HYT. **(a)** Comparison between broadband and high-pass filtered > 20 Hz vertical component 5 hours before and after the mainshock origin time. Red lines: times around the teleseismic waves of the mainshock. **(b)** Instrument-corrected broadband transverse and vertical components. **(c)** High-pass filtered > 20 Hz vertical component. **(d)** Spectrogram. Dashed line: 20 Hz corner frequency used in the high-pass filter to remove the *P* and coda waves from the distant mainshock.

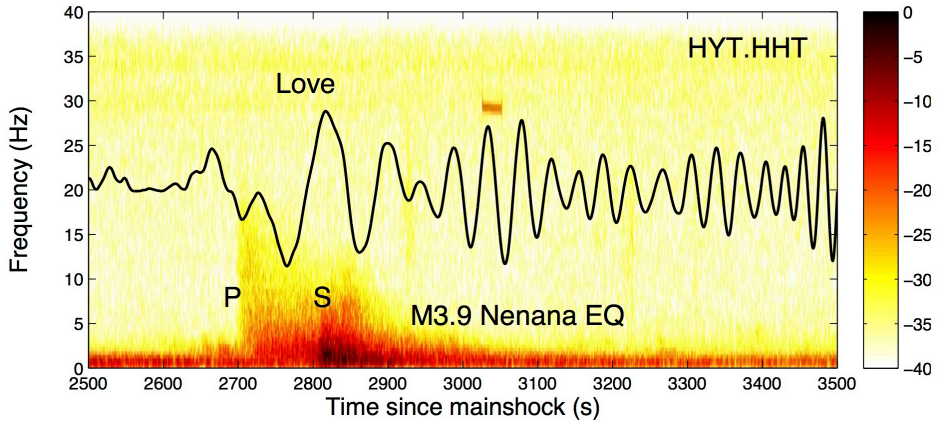

Figure S3.6 – Evidence that no dominant tremor signals triggered by the 2012 Indian Ocean earthquake can be seen at higher frequency bands. Spectrogram of transverse component at station HYT with broadband velocity transverse component plotted on top for reference. Love wave of Indian Ocean mainshock as well as *P* and *S* wave of the *Mw*3.9 Nenana earthquake are marked.

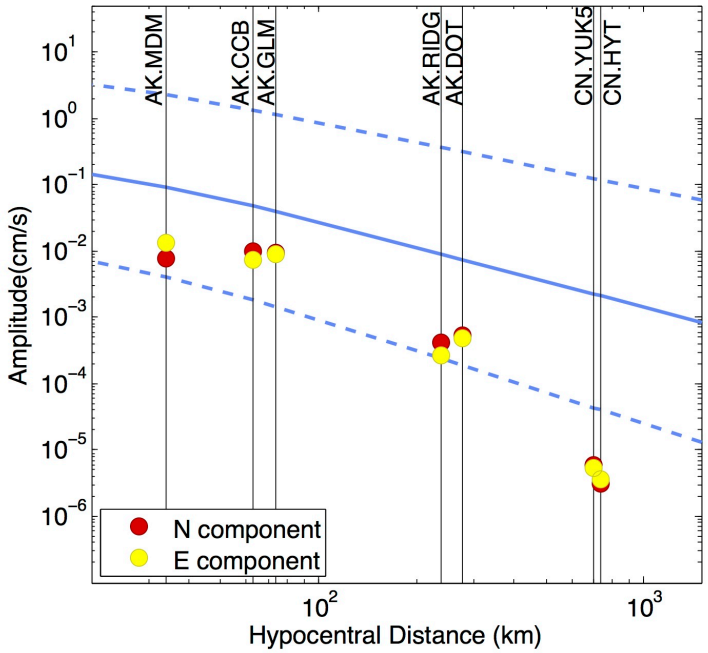

Figure S3.7 - *S*-wave attenuation of the *Mw*3.9 Nenana earthquake. *S*-wave amplitudes measured from high-pass filtered 5 Hz north and east component at multiple stations along the event's ray path to the study region. Network and station names marked by distance with solid black lines. Blue lines = empirical attenuation relationships accounting for event magnitude and distance, with the dashed lines marking 95% confidence. The empirical attenuation relationship and constants follow those of *van der Elst and Brodsky* [2010].

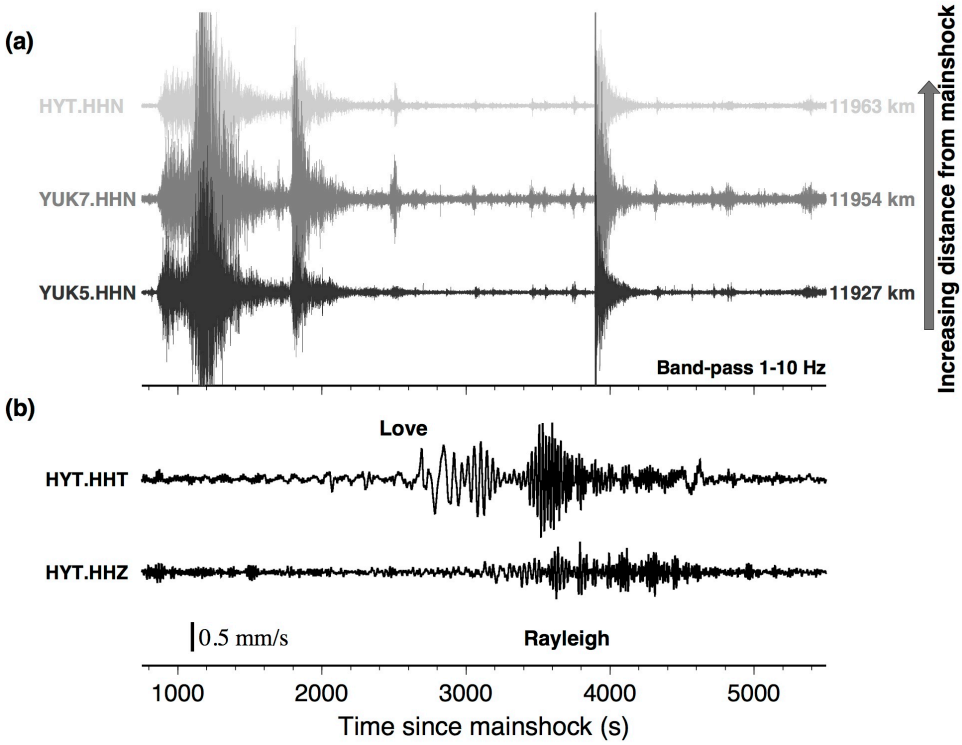

Figure S3.8 - Evidence that the *Mw*8.2 Indian Ocean aftershock did not trigger tremor on the EDF. Symbols and notation are the same as in Figure 3.7.

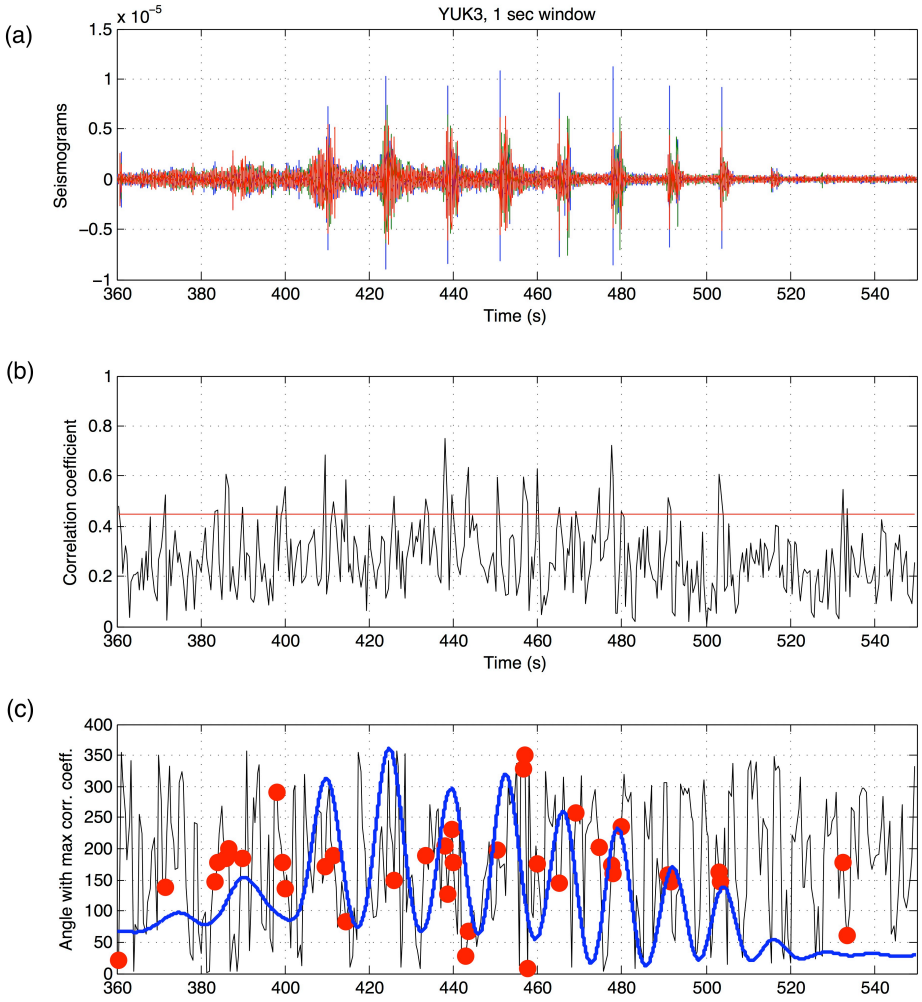

Figure S3.9 - Rayleigh wave polarization analysis for station YUK3. **(a)** High-passed (5 Hz) vertical component (blue), east component (green), and north component (red) seismograms. **(b)** Maximum correlation coefficient at the corresponding azimuth in (c). **(c)** Red filled circles indicate sample points when the correlation coefficient is greater than 0.45. Higher correlation coefficients occur during the triggered bursts and indicate a consistent source azimuth.

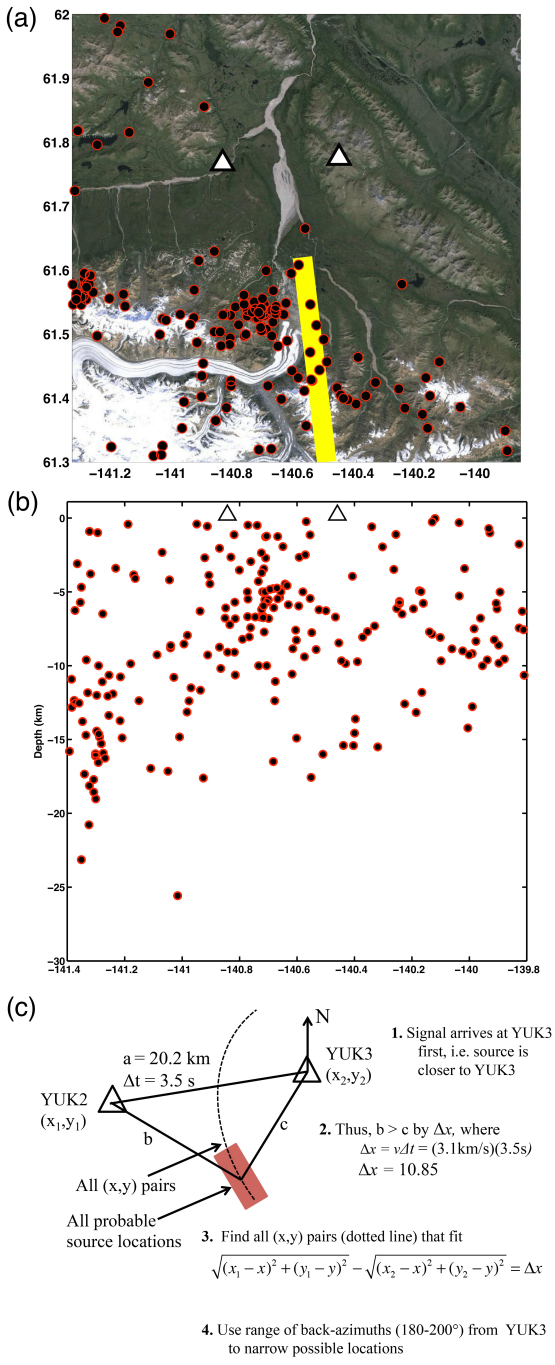

Figure S3.10 - Map of stations and seismicity with a schematic of source determination. **(a)** Satellite map, including YUK2 and YUK3 stations and ANSS seismicity (> *mL* 1.0 during 2010-2013). Yellow area marks possible locations of short-duration events. **(b)** Longitude versus depth plot, indicating relatively shallow depths for seismicity. The linear trend of seismicity indicates the approximate trace of the Duke River Fault. **(c)** Steps in determining approximate location of the source.

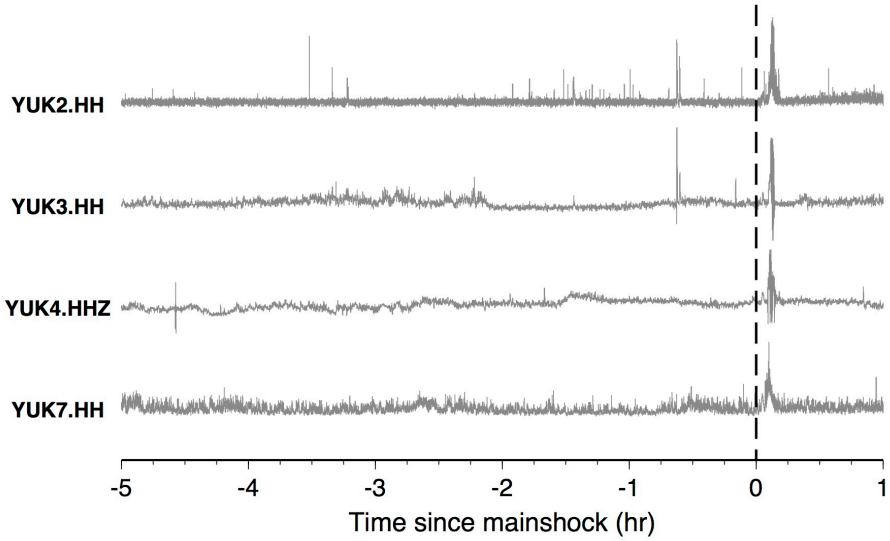

Figure S3.11 - Lack of seismic activity prior to the arrival of surface waves from the Haida Gwaii earthquake. Each trace is an average 3 component, high-pass 20 Hz filtered envelope ($\log_{10}$ scale), with the exception of station YUK4. As stated previously, station YUK4 has significant instrumental noise on the horizontal components. The dashed line marks the origin time of the Haida Gwaii mainshock.

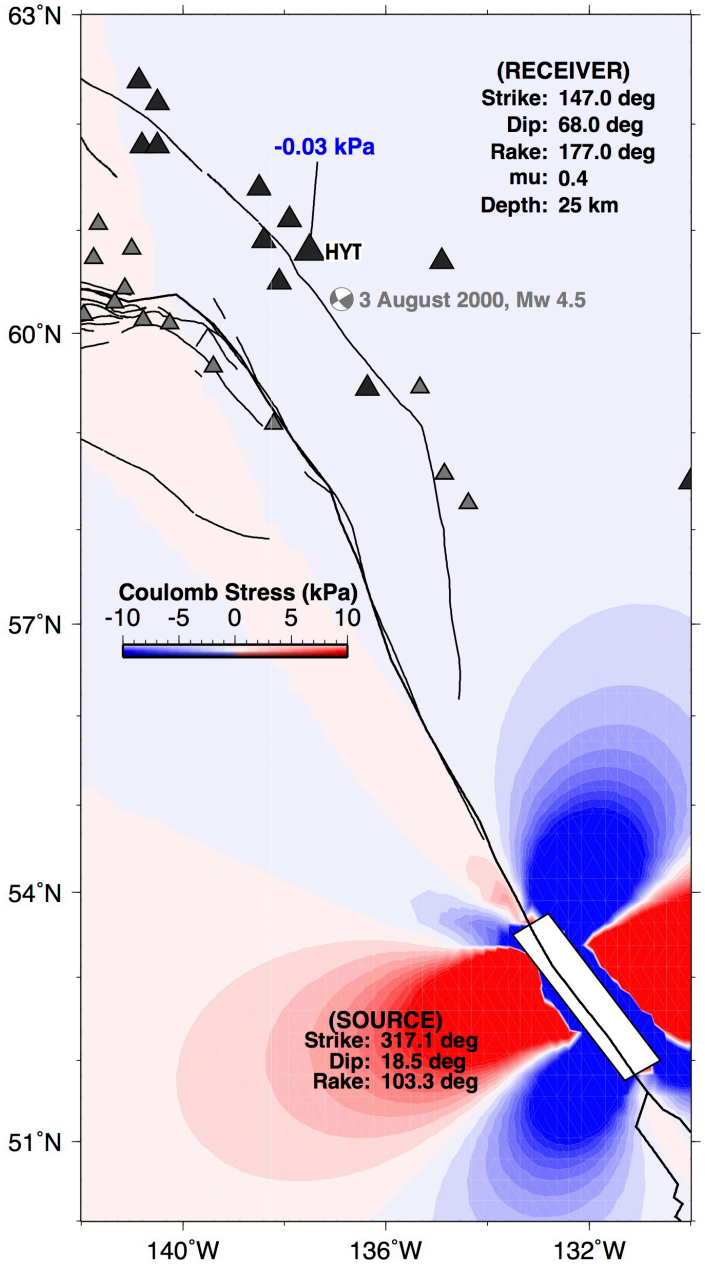

Figure S3.12 - Static stress changes caused by the Haida Gwaii earthquake. Faults and plate boundaries are black lines. Station symbols are the same as Figure 3.5, with the main reference station HYT marked. We utilized source information for the mainshock from *Lay et al.* [2013]. Receiver information is based on a local earthquake from *Kao et al.* [2012] (focal mechanism marked). We show the static stress changes at 25 km depth; this depth is the assumed tremor nucleation depth. There is -0.03 kPa static stress.

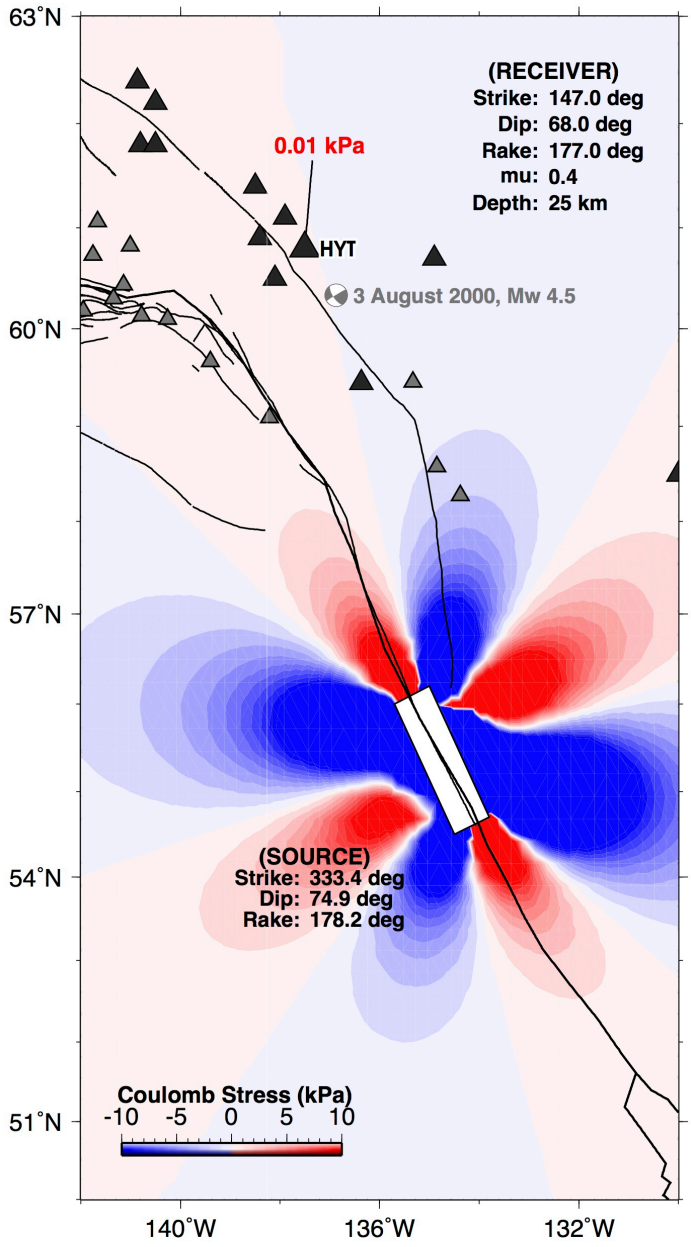

Figure S3.13 - Static stress changes caused by the Craig earthquake. Symbols and notation are the same as in Figure S3.12. We utilized source information for the mainshock from *Lay et al.* [2013].

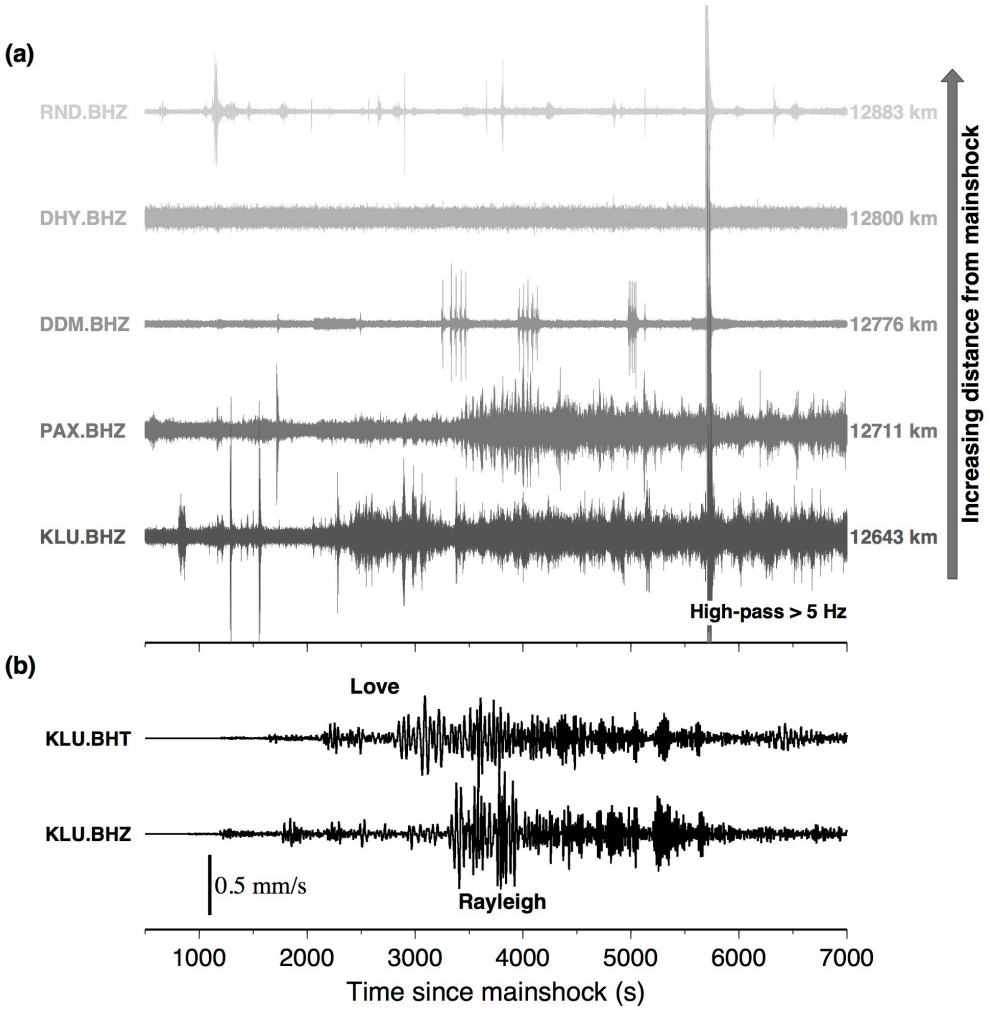

Figure S3.14 - Evidence that the 27 February 2010 *Mw*8.8 Maule, Chile earthquake did not trigger near the aftershock zone of the 2002 Denali Fault earthquake. Symbols and notations are the same as in Figure 3.7.

3.3.7.3 Supplemental Tables

Supplemental tables of *Aiken et al.* [2015b] have been made available via http://geophysics.eas.gatech.edu/people/cautry6/temp/supplementals/dissertationCh3/ (last accessed 17 March 2015). Below is a brief description for each table.

Table S3.3 - Moderate-size events occurring on or near the EDF since 1995.

Table S3.4 - Event information of examined earthquakes.

Table S3.5 - Velocity model for Northern Canadian Cordillera.

3.3.7.4 Supplemental Movies

Supplemental movies of *Aiken et al.* [2015b] have been made available via http://geophysics.eas.gatech.edu/people/cautry6/temp/supplementals/dissertationCh3/ (last accessed 17 March 2015). Below is the caption associated with each movie.

Movie S3.1 - Tremor around the eastern Denali Fault, Yukon, Canada, recorded at station CN.HYT triggered by the 28 October 2012 *Mw*7.8 Haida Gwaii earthquake. **(Top)** Broadband transverse-component seismogram recorded at the station HYT. **(Middle)** 20 Hz high-pass-filtered transverse-component seismogram showing the P wave of the distant mainshock and triggered tremor signals. **(Bottom)** Spectrogram of the transverse-component seismogram. A 0.5-Hz high-pass filter is applied to remove long-period signals before computing the spectrogram [*Peng et al.*, 2011]. The sound is generated by speeding up the seismic data by 100 times [*Kilb et al.*, 2012].

Movie S3.2 - High-frequency bursts in Yukon Canada recorded at station CN.YUK2 triggered by the 28 October 2012 *Mw*7.8 Haida Gwaii earthquake. Other symbols are the same as in Movie S3.1.

3.4 Triggering Along the Enriquillo-Plantain Garden Fault, Haiti [*Aiken et al. 2015a]*

This work presented in this section is in preparation for publication. In *Aiken et al.* [2015a], we examine the possibility of the 27 February 2010 *Mw*8.8 Maule, Chile earthquake triggering seismic activity along the Enriquillo-Plantain Garden Fault (EPGF) in the southern peninsula of Haiti, near the aftershock zone of the 12 January 2010 *Mw*7.0 Haiti earthquake. The Maule, Chile earthquake is the 6th largest earthquake that has occurred since 1900, and surface waves from this mainshock have triggered

microearthquakes and tectonic tremor in many regions of the Western Hemisphere [e.g., *Peng et al.*, 2010, 2011; *Zigone et al.*, 2012; *Gomberg and Prejean*, 2013; *Aiken et al.*, 2013b; *Aiken and Peng*, 2014]. Because of its widespread triggering, it is possible that it has triggered seismic activity along the EPGF, a transpressive left lateral fault. Here, we search for triggered tremor and earthquakes using seismic data recorded by 25 land and ocean-bottom seismometer (OBS) stations, a temporary network deployed to record aftershocks following the devastating *Mw*7.0 Haiti earthquake [*de Lepinay et al.*, 2011].

We investigate dynamic triggering of tremor and earthquakes for two reasons. Since large earthquakes are capable of occurring on this fault, it would be interesting if a relationship between ambient tremor activity and large earthquakes exists. However, to investigate this relationship tremor activity must first be identified. Therefore, we primarily search for dynamically triggered activity because we know when the triggering might occur - during or immediately following the large amplitude surface waves of the 2010 Chile mainshock [e.g., *Brodsky*, 2006; *Peng et al.*, 2008; *Peng et al.*, 2011]. After identifying triggered seismic activity, we locate the triggered sources and test the Coulomb-failure criterion for the surface waves of the Chile earthquake inducing failure on the EPGF.

3.4.1 Tectonic Setting

The EPGF of the southern Haiti peninsula acts as a left lateral transform boundary between the Caribbean plate and Gonâve microplate, which move at a rate of ~7 mm yr^{-1} relative to one another (Figure 3.14) [*Manaker et al.,* 2008]. In addition, the EPGF has a minor thrust component [*Calais et al.*, 2010], resulting in a transpressive environment, similar to the Alpine Fault in New Zealand and the Queen Charlotte Fault near Haida

Gwaii, Canada where tectonic tremor has recently been discovered [*Wech et al.*, 2012; *Aiken et al.*, 2013a]. The region surrounding the EPGF has experienced a series of *M*6 and *M*7 (*M*, magnitude) earthquakes since the start of the 18th century until the 12 January 2010 *Mw*7.0 Haiti mainshock, which ended a 240-year quiescence of moderate-sized earthquakes [*Bakun et al.*, 2012]. The Haiti mainshock was originally thought to have occurred on the EPGF [*Hayes et al.*, 2010]. However, a subsequent analysis found that the mainshock initiated on a secondary thrust fault north of the EPGF, the Léogâne fault, and later the rupture continued onto the EPGF [*Calais et al.*, 2010]. Aftershocks of the *Mw*7.0 Haiti earthquake predominately occurred on secondary overlapping reverse faults, located north of the EPGF (Figure 3.14) [*Douilly et al.*, 2013].

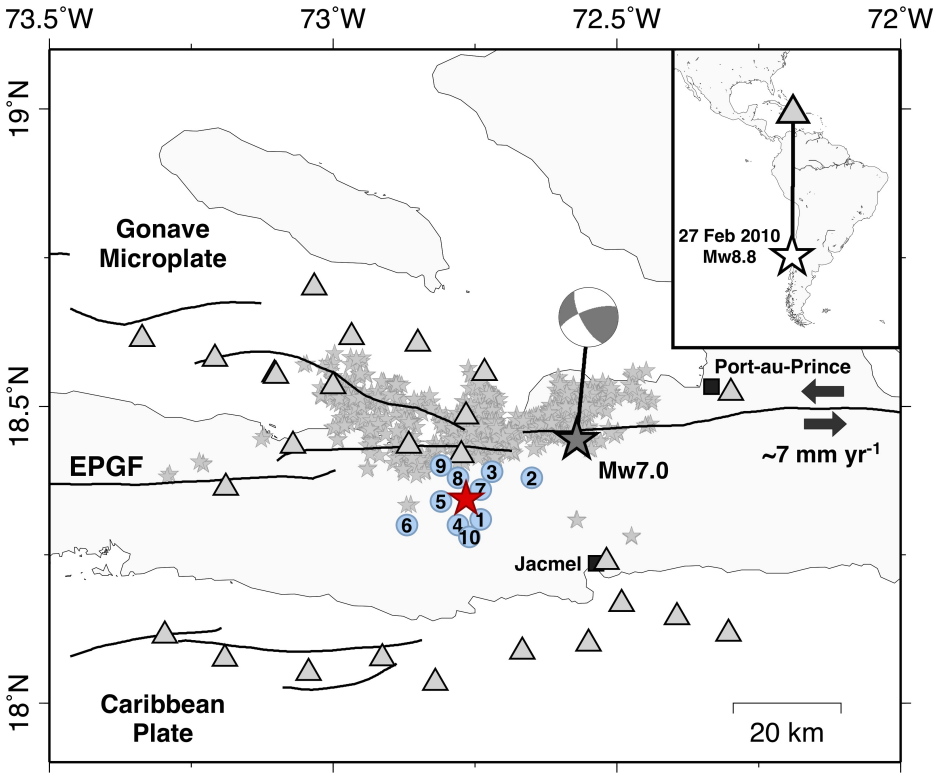

Figure 3.14 - Map of the southern Haiti peninsula. Black lines = fault traces. Enriquillo-Plantain Garden Fault marks the boundary between the Caribbean Plate and Gonâve microplate. Triangles = seismic stations. Gray stars = Haiti mainshock and its aftershocks. Focal mechanism of the 12 January 2010 *Mw*7.0 Haiti earthquake is

indicated. Squares = major cities. Circles = tremor bursts triggered by the *Mw*8.8 Maule, Chile earthquake (white star in inset). Red star = average location of the 10 tremor bursts.

3.4.2 Analysis and Procedure

Several research institutions deployed seismometers to record aftershocks of the Haiti earthquake, and we utilized recordings on 27 February 2010 from some of these stations for our investigation (Figure 3.14). Research groups from Géoazur and the Institut Français de Recherche pour l'Exploitation de la Mer (IFREMER) installed short period and broadband ocean bottom seismometers (OBS), which have four components including a hydrophone. The Institut de Physique du Globe de Paris (IPGP) also deployed four 3-component broadband seismometers near the EPGF trace, and the Natural Resources Canada (NRCan) agency installed 2 broadband seismometers near Jacmel (station JAKH) and Port-au-Prince (station PAPH). Station JAKH and PAPH are part of the Canadian National Seismograph Network (CNSN). A summary of the station information can be found in Table 1 of *Douilly et al.* [2013].

Seismic data from the permanent JAKH and PAPH stations were processed similar to *Aiken et al.* [2013a] (Section 3.2.2) and any differences are briefly described here. Instrument responses for the temporary short-period and OBS stations from IFREMER and IPGP were not removed since amplitude is not an important factor in this study, i.e. we are mostly interested in the timing of events surrounding the arrival of the surface waves. Prior to our analysis, we applied station corrections to the OBS data to adjust for travel times through the thick ocean sediments and other near surface effects, similar to *Douilly et al.* [2013]. After correcting the travel times, we filtered the seismic data using a 2-16 Hz band-pass filter to detect local seismic activity. Applying a 2-16 Hz band-pass filter avoids contamination by the *P*-wave of the Chile mainshock as well as

early aftershocks radiating from the Chile mainshock region. The 2-16 Hz frequency band is also the dominant frequency band for deep tremor and local earthquakes [e.g., *Aiken et al.,* 2015b; *Aiken and Peng*, 2014].

3.4.3 Triggering Observations

3.4.3.1 Tectonic Tremor

Using the 2-16 Hz band-pass filter, we observed tremor triggered by the large amplitude surface waves of the Chile mainshock. Figure 3.15 shows an example of the triggered tremor recorded by the JAKH and PAPH stations. Amidst the continuing aftershock activity of the Haiti mainshock, strong triggered tremor signals can be identified beginning around the arrival time of the surface waves of the Chile mainshock, i.e., ~1400 s after the mainshock origin time. From this initial visual inspection of the broadband spectra, 3 distinct tremor-like signals containing frequencies of ~1-10 Hz can be clearly seen. These tremor signals can be easily distinguished from the on-going aftershock activity, since the tremor bursts have long-duration, emergent signals without the distinct *P*- or *S*-waves reminiscent of regular earthquakes. Furthermore, when the seismic data is sonified the tremor bursts sound like a starting steam engine and can be audibly distinguished from teleseismic *P*-waves of the Chile mainshock that sound like distant thunder and local aftershocks that sound like firecrackers [*Peng et al.*, 2012] (Movie S3.3).

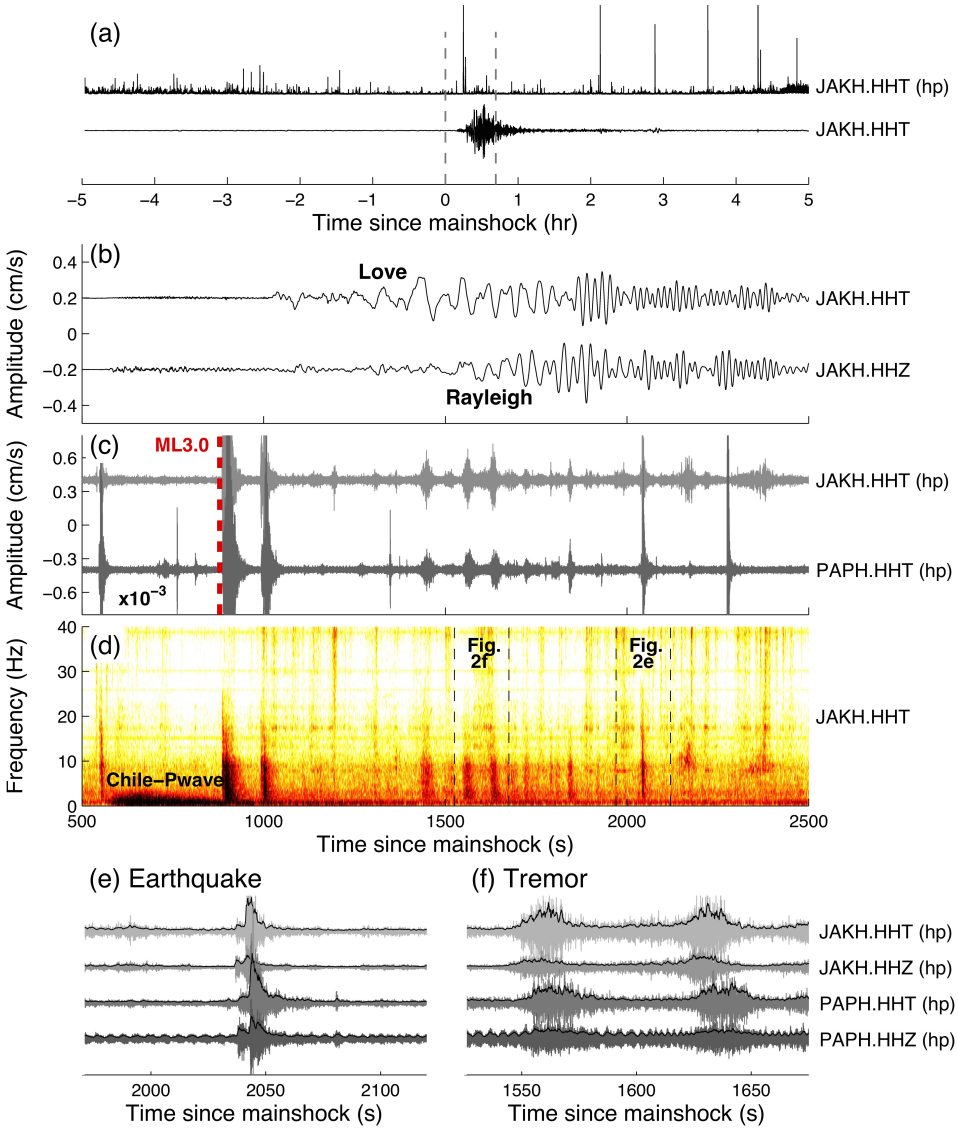

Figure 3.15 - Example of tremor triggered by the Maule, Chile earthquake. **(a)** High-passed filtered 5 Hz envelope and broadband transverse velocity component from station JAKH ±5 hours around the Chile mainshock. Dashed lines = time window plotted in (b) thru (d). **(b)** Broadband transverse and vertical velocity components from station JAKH. **(c)** High-passed filtered 5 Hz transverse velocity waveforms from stations JAKH and PAPH. Red dashed line = M_L3.0 earthquake recorded in the ANSS catalog. **(d)** Spectrogram of station JAKH transverse velocity component. Part (e) and (f) of this figure are outlined by dashed lines, highlighting spectral differences between an aftershock and triggered tremor, respectively. **(e)** Aftershock with distinct *P*- and *S*-waves, as recorded on the transverse and vertical velocity components of stations JAKH and PAPH. **(f)** Triggered tremor recorded as an emergent signal on the transverse and vertical velocity components of stations JAKH and PAPH.

While these tremor signals can be distinguished on a smaller time scale, over a longer time scale (e.g., ± 5 hours around the Chile mainshock) these tremor signals are dominated by the higher amplitude Haiti aftershocks (Figure 3.15a). Of the 25 stations we examined, we were able to observe these 3 stronger tremor-like signals on all stations (with the exception of station HA15) after applying a 2-16 Hz band-pass filter (Figure 3.16). In addition to the stronger tremor bursts, we observed a couple of weak tremor-like signals between the strong tremor signals and several more weak tremor-like signals after ~1650 s. These weaker signals were not as visible in the broadband spectra (Figure 3.15) and also are not as coherent among all the stations (Figure 3.16). In total, we identified 10 tremor bursts occurring during the surface waves of the Chile mainshock. After randomly sampling the background activity in a 5 hour window prior to the Chile mainshock and using a point summation technique [e.g., *Jiang et al*., 2010; *Wu et al.*, 2012], we detected a significant increase in the tremor activity, such that $\beta \geq 2$ when using a threshold of 2 times the median absolution deviation (MAD) (Figure S3.15). In general, a β-statistic ≥ 2 indicates a significant increase in seismic activity as compared to background seismic activity at ~95% confidence level [e.g., *Hill and Prejean*, 2007].

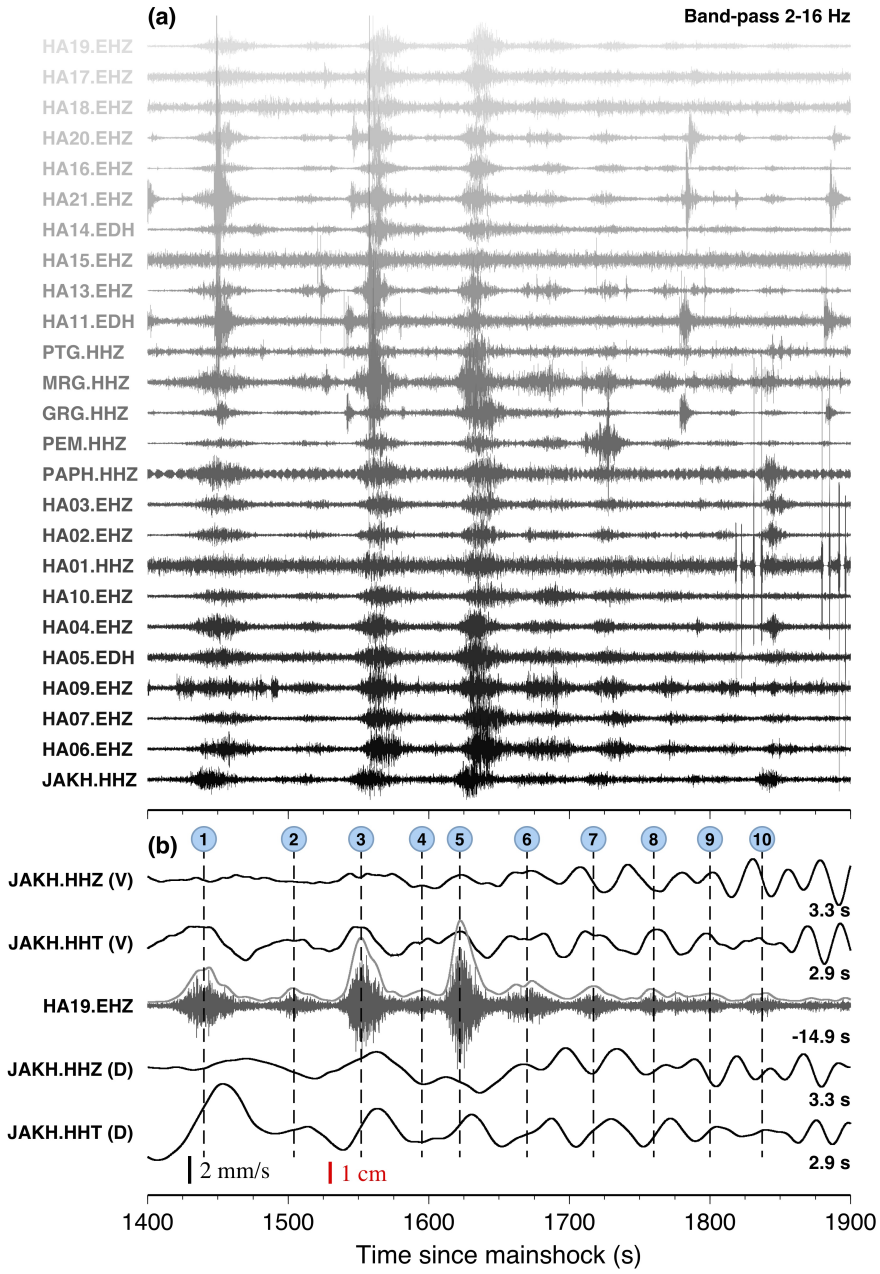

Figure 3.16 - Evidence of triggered tremor recorded on 25 seismic stations and its correlation with surface waves of the Chile mainshock. **(a)** Band-passed filtered 2-16 Hz vertical velocity waveforms from the 25 stations used in this study. Where the vertical component is not available or has poor quality, we substitute the hydrophone component (EDH). **(b)** Transverse and vertical velocity (V) and displacement (D) waveforms recorded at station JAKH with band-pass filtered 2-16 Hz waveform and envelope recorded by station HA19. Waveforms are time-shifted to the average tremor source location (red star in Figure 3.14). Dashed lines = peaks of the tremor bursts (based on the envelope); Dashed lines show correlation with the surface waves of the Chile mainshock. Circles = tremor burst number and correspond to locations to Figure 3.14. Black vertical bar = scale for broadband velocity waveforms. Red vertical bar = scale for broadband displacement waveforms.

For triggered tremor signals we observed among several stations, we located their sources using an envelope cross-correlation technique, similar to *Chao et al.* [2013]. Most of the tremor sources are located south of the EPGF surface trace (Figure 3.14), but the depths are not well constrained with this method due to the lack of a *P*-wave arrival (e.g., Figure S3.16). Therefore, we set the depth of the average tremor source location to be 25 km, as this is approximately the depth of tremor sources identified along similar transform boundaries, like the Parkfield-Cholame segment of the SAF in California [*Shelly et al.,* 2009] and Alpine Fault in New Zealand [*Wech et al*., 2012]. Using the depth of 25 km, we shifted the waveforms to this average location to examine the correlation between the tremor and the arrival of the surface waves from the Chile mainshock at the place from which the tremor emerges [*e.g.*, *Rubinstein et al.*, 2007; *Peng et al.*, 2009]. As shown in Figure 3.16b, the tremor bursts correlate well with the positive peaks of the Love wave velocity, i.e. the transverse component.

3.4.3.2 Aftershocks of the 2010 Mw7.0 Haiti Earthquake

To investigate earthquake activity around the Chile mainshock, we used two catalogs – our own hand-picked earthquake catalog (from the day of seismic data, i.e. 27 February 2010) and the Haiti aftershock catalog of *Douilly et al.* [2013] for earthquakes occurring from February to June 2010. We hand-picked earthquakes occurring on 27 February 2010 because many aftershocks were visible when inspecting the waveforms but were not always listed in the Haiti aftershock catalog [*Douilly et al.*, 2013]. Thus, hand-picking earthquakes identified more events around the time of the Chile mainshock, allowing us to verify whether or not there was a significant change in Haiti aftershock

activity in the few hours surrounding the arrival of seismic waves from of the Chile mainshock.

We used envelope functions of the band-pass filtered waveforms to construct our hand-picked earthquake catalog [*e.g.*, *Peng et al.*, 2007]. In particular, we identified earthquakes with distinct *P*- and *S*-waves visible on stations GRG, MRG, and HA17, as well as stations JAKH and PAPH. We then measured the *S*-wave amplitude peaks of these earthquakes. We chose stations GRG, MRG, and HA17 because these stations have lower noise levels than other stations and because these stations surround the aftershock region. We utilized *S*-wave amplitude measurements at stations JAKH and PAPH to estimate each hand-picked earthquake's magnitude, as we removed the instrument response from the waveforms recorded by these stations. To estimate the magnitude of each hand-picked earthquake, we assumed a tenfold increase in displacement amplitude (A, measured in μm) corresponds to an increase in one unit magnitude (M) [*Peng et al.*, 2007], such that

$$M = a\log_{10}(A) + b \tag{3.2}$$

where a = 0.8964 and b = *3.1964*. Constants a and b were determined from a least square fit using *S*-wave amplitudes from stations JAKH and PAPH for 8 earthquakes listed in the CNSN catalog occurring on 27 February 2010 (Figure S3.17, Table S3.6). Next, we used the *S*-wave displacement amplitudes of all hand-picked earthquakes, the a and b values, and equation 3.2 to estimate the magnitude of events not listed in the CNSN catalog. We note that this simple estimation of earthquake magnitude does not account for amplitude attenuation due to source distance.

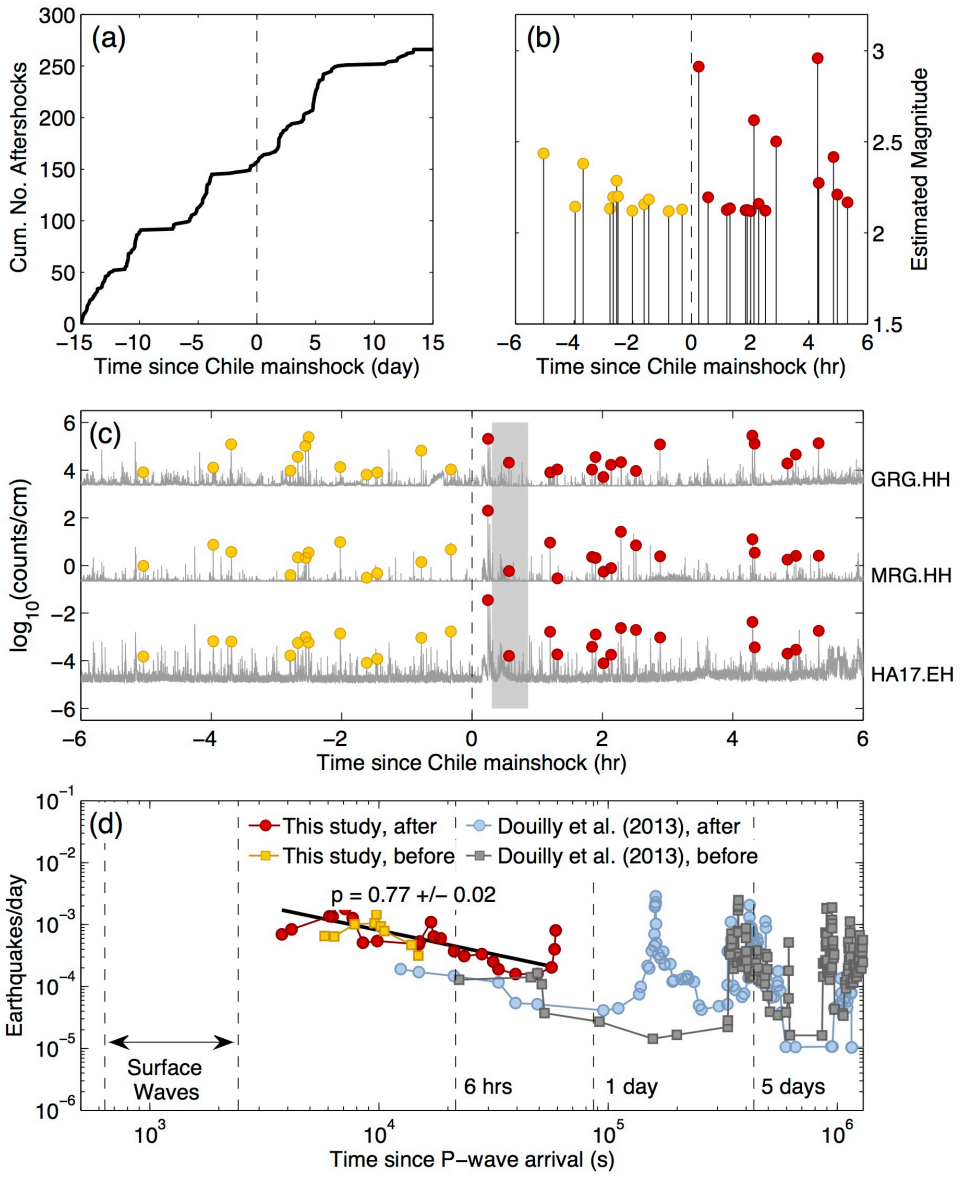

Figure 3.17 – Summary of Haiti aftershock activity around the Chile mainshock. **(a)** Aftershocks detected by *Douilly et al.* [2013] ± 15 days around the Chile mainshock. Dashed line = origin time of Chile mainshock. **(b)** Estimated magnitudes of hand-picked earthquakes 6 hours before (yellow circles) and after (red circles) the Chile mainshock. Magnitudes are estimated using amplitudes measured from station JAKH. **(c)** Band-pass filtered 2-16 Hz envelopes from stations GRG, MRG, and HA17. Hand-picked earthquakes are marked. Gray box = time window of the Love and Rayleigh waves, i.e. between the 5 km s^{-1} and 2 km s^{-1} arrival. **(d)** Seismicity rates using our hand-picked earthquake catalog and the Haiti aftershock catalog of *Douilly et al.* [2013]. We perform a least-squared fit of a simple Omori law aftershock decay to our hand-picked earthquakes occurring after the Chile mainshock. Note there is no rate during the surface waves because only 1 earthquake was identified during this time (part (c) of this figure).

Figure 3.17 shows a summary of our analysis of local earthquake activity around the time of the Chile mainshock. Using the standard Haiti aftershock catalog of *Douilly et al.* [2013], we did not observe any obvious increase in aftershock activity following the surface waves of the Chile mainshock over a 30-day period (Figure 3.17a). Indeed, a simple β calculation computed using the Haiti aftershock catalog confirms that there is no significant increase in Haiti aftershock activity in the several days following the Chile mainshock (Table 3.2).

Table 3.2 - β-values for varied Haiti aftershock triggering windows*

Time window	Beta value (median)
+/- 0.5 day	+0.45
+/- 1 day	-0.12
+/- 2 days	-0.43
+/- 4 days	-0.15
+/- 8 days	+0.04
+/- 15 days	-1.42

* Background window for the β-value calculation was randomly sampled 100 times from 15 days of aftershock activity occurring before the *P*-wave of the Chile mainshock, with the exception of the '+/- 15 days' calculation.

A simple moving window seismicity rate calculation [e.g., *Ziv et al.,* 2003; *Felzer and Brodsky*, 2006] of our hand-picked catalog and the standard Haiti aftershock catalog [*Douilly et al.*, 2013] also indicates that seismic activity rates before and after the Chile mainshock are similar. A least square fit of a simple Omori Law aftershock rate decay of $r(t) \sim t^{-p}$ to our hand-picked Haiti aftershocks occurring after the Chile mainshock leads to a *p*-value of 0.77 +/- 0.02, where typically $p = 1$. Thus, from our analysis of aftershock activity over both long and short time frames, it appears that there is no significant

increase in the aftershock activity rate due to the surface waves of the Chile mainshock. In addition, the 41 hand-picked Haiti aftershocks have magnitude ranging from 2.1 to 4.0. Just before the Love wave of the Chile mainshock arrives in Haiti, a *M*3.0 aftershock occurred (Figure 3.15c) as well as a *M*2.2 (estimated). After the surface waves pass through the region, the Haiti aftershocks appear to have slightly higher magnitude (Figure 3.17b-c) compared to 6 hours before the Chile mainshock. However, it is unclear whether the increase in magnitude is due to the passing seismic waves or if it is just part of random fluctuations in the Haiti aftershock processes.

3.4.4 Characteristics of Triggering Waves

We model how transient stresses due to the passing Love and Rayleigh waves act on the EPGF, i.e. the triggering potential of the surface waves. The triggering potential model is based upon the change in the Coulomb failure function, fault geometry, amplitude and frequency of the surface waves, and depth of interest (i.e., source of triggered tremor). The change in the Coulomb failure function (δCFF) depends upon the change in a fault plane's shear ($\delta\tau$) and normal ($\delta\sigma_n$) stresses due to the surface waves, as well as the coefficient of friction on the fault plane (μ) such that

$$\delta CFF = \delta\tau + \delta\tau + \mu\delta\sigma_n. \quad (3)$$

That is, the stress tensor can be rotated such that the two components are in the fault plane (shear; in the strike and dip directions) and one is perpendicular to the fault plane (normal). Details on how to compute the change in the Coulomb failure function can be found in *Gonzalez-Huizar and Velasco* [2011].

Figure 3.18 illustrates our model of how stresses change on the EPGF during the Chile mainshock surface waves at the triggered tremor source depth, which we set to be

25 km (Section 3.4.3.1). For the triggering potential model, we assumed the EPGF is a vertical fault with a dip of 90° and a strike of 0° that has a coefficient of friction (μ) of 0.3. After computing the shear and normal dynamic stresses acting on the EPGF, it is clear that shear stress changes caused by the Love wave are greater than normal stress changes caused by the Rayleigh wave. Indeed, when we cross-correlated the envelope function of the tremor signals with the dynamic stress functions, we obtained correlation coefficients (c.c.) of 0.78 and 0.12, for the Love and Rayleigh waves respectively. Thus, the Love waves of the Chile mainshock are predominately responsible for the triggering of the tremor we observed.

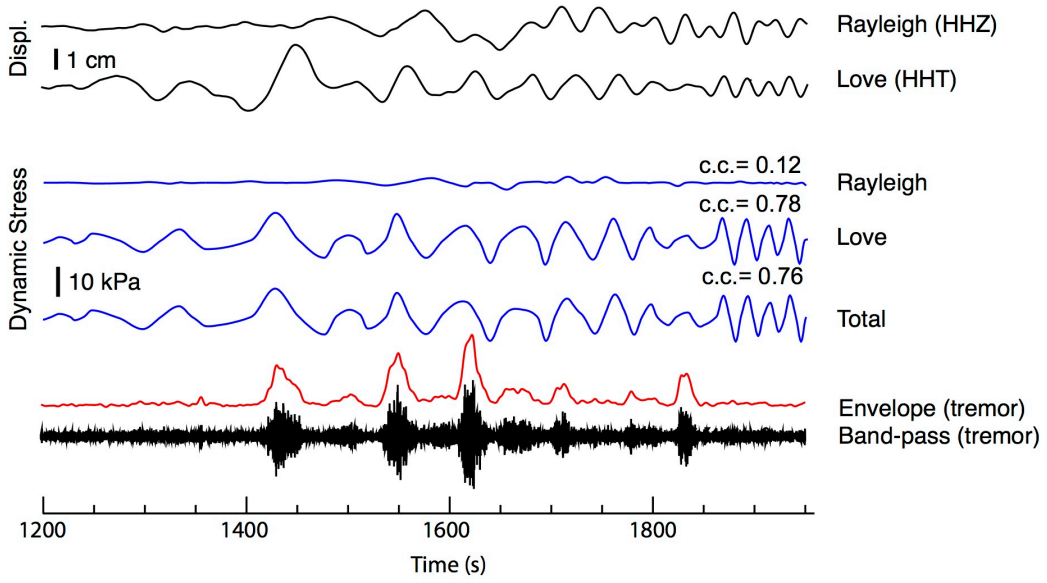

Figure 3.18 - Triggering potential model of surface waves from the Chile mainshock. Black traces at top = broadband vertical and transverse displacement waveforms from station JAKH. Blue traces = computed dynamic stressgrams with correlation coefficient (c.c.) marked. The correlation coefficient is ascertained by cross-correlating a stressgram with the filtered envelope function of the tremor signal. Black trace at bottom = band-pass filtered 2-16 Hz waveform from station GRG. Red trace = its envelope function.

3.4.5 Discussion and Conclusions

In this study [*Aiken et al.*, 2015a], we investigated the impact of seismic waves from the 27 February 2010 *Mw*8.8 Maule, Chile earthquake on the Enriquillo-Plantain Garden Fault and surrounding faults affected by the 12 January 2010 *Mw*7.0 Haiti earthquake. We examined seismic data from 25 temporary land and OBS stations in search of tremor and/or Haiti aftershocks induced by the surface waves of the Chile mainshock. We observed ~10 tremor bursts triggered instantaneously by the long period surface waves of the Chile mainshock (Figure 3.16), the first observation of tremor in southern Haiti peninsula. The triggered tremor sources radiate in the ~1-10 Hz frequency band (Figure 3.15) and appear to nucleate just south of the EPGF fault trace (Figure 3.14). While we found clear evidence of triggered tremor, no clear increase in Haiti aftershock activity was identified either in the short or long term (Figure 3.17).

As illustrated in Figure 3.15, the tremor-like signals are distinctly different from that of local earthquakes, which have impulsive arrivals. One may argue that the tremor-like signals we observe are not tremor but rather *P*-waves of earthquakes occurring at regional distances. However, we found no record of earthquakes that are consistent with the arrival times of the tremor bursts in either the CNSN or ANSS global catalogs. Also, when we examine how the tremor signal radiates from the source over time, it is clear that the tremor bursts have a speed of ~3.5 km/s, i.e. the speed of an *S*-wave (Figure S3.18). Because the tremor signal travels at the speed of an *S*-wave, we surmise that the tremor represents deep, shear slip on the EPGF, as has been observed along the SAF in Parkfield, CA [*Shelly et al.*, 2011]. However, unlike *Shelly et al.* [2011], we did not

observe any clear migration of the triggered tremor activity that would evidence an episodic creep occurring deep within the fault (Figure 3.14).

Recently, dynamic triggering studies have focused on identifying the relationship between fault geometry and the amplitude and frequency of a seismic wave, with regard to the depth of the tremor source, since amplitudes of surface waves decay with depth [e.g., *Hill*, 2012 and references therein; *Gonzalez-Huizar and Velasco*, 2011]. While we were not able to conduct a systematic study of earthquakes triggering tremor in this region like that of *Aiken and Peng* [2014], our triggering potential model of the dynamic stress changes caused by the Love and Rayleigh waves indicates that the Love wave is the dominant driving force for triggering tremor, generating dynamic stress $\geq$ 10 kPa at 25 km depth (Figure 3.18). The Love wave propagates as a surface wave with horizontal displacements perpendicular to the direction of propagation, and given the location of the Chile mainshock and East-West strike of the EPGF, it is clear that the transient stresses caused by the Love wave act in the same direction as the local stresses on the fault (Figure 3.14). Based on the fault orientation and direction of propagation, the Coulomb failure criterion predicts that vertical transform faults will be triggered mainly by the Love wave with an incidence perpendicular to the fault strike [*Hill*, 2012].

Our triggered tremor locations have small horizontal errors, but the depths are not well resolved (e.g., Figure S3.16). *Aiken et al.* [2013a, 2015b] used a similar envelope cross-correlation technique to locate triggered tremor. However, in those studies, the source depth was also not well constrained, and the depth was set to 25 km – a depth at which tremor has been observed along the Parkfield-Cholame segment of the SAF [*Shelly et al.,* 2009]. When we similarly set the depth of the tremor sources to be 25 km, we

observed a clear correlation between the Love wave and tremor bursts (Figure 3.18). We note that the correlation coefficient between the Love wave dynamic stresses and tremor envelope function is high (c.c. = 0.76), but not exactly equal to 1. Therefore, it is possible that the dip of the fault is not 90°, as *Prentice et al.* [2010] inferred from their field studies. In their study, they ascertained from surface ruptures from the 12 January 2010 *Mw*7.0 Haiti mainshock that the EPGF is a high-angle (> 60°) south-dipping fault, at the very least nearest to the Haiti mainshock. A high-angle south-dipping EPGF is in agreement with our locations of the triggered tremor sources (Figure 3.14).

Tremor appears to be more easily triggered than earthquakes, as has been observed in a comparison study of earthquake and tremor triggering stress thresholds in California [*Aiken and Peng*, 2014], as well as in the laboratory [*Bartlow et al.*, 2012]. In Haiti, most of the aftershock activity occurred on secondary high-angle (>65°) reverse faults (Figure 3.14) [*Douilly et al.,* 2013]. High-angle (>60°) reverse faults are typically locked and not easily reactivated because they are not optimally oriented [*Sibson*, 2012]. This fact may explain why we did not observe an increase Haiti aftershock activity in response to surface waves from the Chile mainshock. In addition, small earthquakes triggered by surface waves of larger earthquakes are typically observed in fluid-rich geothermal regions [*Aiken and Peng*, 2014] and triggering in non-geothermal regions is rare [*Sullivan et al.*, 2012]. For example, *Sullivan et al.* [2012] showed that an aftershock region can be loaded by long-period surface waves that propagated 360° back to the mainshock epicenter, resulting in increased aftershock activity. However, we did not observe any influence of the Chile mainshock on Haiti aftershock activity - only a standard Omori decay for the Haiti aftershocks (Figure 3.17d). Surfaces waves generated

by large magnitude earthquakes, like the Chile mainshock, are also capable of circling the Earth multiple times and triggering earthquake activity upon returning to region [*Peng et al.,* 2011], but we found no evidence of such a triggering process (e.g., Table 3.2). Another possible explanation for no observed aftershock triggering is that the amount of transient stress needed to push a fault closer to failure likely varies in time. It is difficult to accurately describe the stress state of those secondary faults where the Haiti aftershocks occur. A fault's stress state can fluctuate due to earthquake activity, variations in regional stressing, and even fluid migration along the fault, hence affecting the triggering behavior [*Brodsky and van der Elst*, 2014].

3.4.6 Future Work

Over the last decade, observations of triggered tremor and earthquakes have become abundant, and triggering studies such as this are beneficial to answering questions regarding the interaction of tremor and earthquakes. Future work includes identifying ambient tremor activity along the EPGF and determining its relationship to the potential new series of moderate earthquakes and the triggering of shallow earthquakes in response to deep fault slip. Moreover, ambient and triggered tremor studies focused in the southern Haiti peninsula could elucidate differences between tremor occurring on the EPGF and other strike-slip faults where tremor has been observed.

Specifically, there are a few opportunities for improving this work prior to submitting for publication. First, the aftershock detection technique is somewhat outdated. While selecting earthquakes based on observable *P*- and *S*-wave phases can

insure that a seismic signal is truly an earthquake, this method becomes more difficult when the seismicity rate is extremely high, such as during a time of aftershock activity. That is, overlapping of earthquake phases in seismic recordings will inhibit the identification of earthquakes missing from earthquake catalogs [*Peng et al.,* 2007], as is likely the case in this study (Figure 3.17c). One way to improve earthquake detection is to utilize a recently developed matched filter technique [*Peng and Zhao*, 2009]. This technique scans waveform templates of known earthquakes through continuous seismic recordings in search of similar earthquakes. A new earthquake is detected when the waveform similarity between the template and the continuous recordings exceeds a given threshold. This technique has proven to detect at least 11 times more aftershocks in the first 2 days following a *M*6 earthquake in Parkfield, California than was reported in U.S. Geological Survey earthquake catalogs [*Peng and Zhao*, 2009]. In Haiti, waveforms of known aftershocks (Table S3.6) can be used to search for additional aftershocks that could not be selected based on visual inspection alone (Figure 3.17c). Using the matched filter technique to detect earthquakes instead of visual inspection will provide a new outlook on whether or not Haiti aftershocks can be influenced by seismic waves of the Chile mainshock.

Second, the envelope cross-correlation technique used to locate the triggered tremor is unreliable when determining the depth of the source (Figure S3.16). It is also unclear whether the horizontal locations of the triggered tremor are robust (Figure 3.14), as the dip of the EPGF is not precisely known [*Prentice et al.*, 2010]. One way to elucidate the accuracy of the envelope cross-correlation technique used to locate the tremor sources is to use the same method to locate aftershocks with known locations. The

S-wave peaks of the aftershocks listed in Table S3.6 can be used for location, similar to how the peak of a tremor burst is used to locate its source. There may be some differences in how accurately the earthquakes and tremor are located due to the inherent characteristics of their sources. For example, tremor is emergent and low-amplitude, while earthquakes are impulsive and high-amplitude (Figure 3.15). In addition, tremor has been shown to be predominantly the *S*-wave of many LFEs [*Shelly*, 2009]. Thus, each tremor burst pick is essentially an average *S*-wave arrival of many LFEs, which could affect the source location if the LFEs nucleate from different locations.

While we observed that the Love wave of the Chile mainshock is predominately responsible for the triggering of the tremor, one may notice that the similarity test (c.c. value) between the Love wave stressgram of the Chile mainshock and the tremor envelope is not exactly 1 (Figure 3.18). The Coulomb-failure criterion [*Hill*, 2012] predicts solely Love wave triggering, given that the Love wave has perpendicular incidence on the vertical fault. However, the c.c. value is less than 1, suggesting other factors. For instance, this observation could be a reflection of location accuracy of the tremor, as waveforms are shifted in time to reflect what is happening at the source location. Improving the locations as mentioned previously could improve the c.c. value. A second factor could be that the EPGF is not exactly vertical, a finding suggested by *Prentice et al.* [2010]. In fact, the dip of the EPGF could range from 60-90°. Once the locations of the triggered tremor activity have been finalized, the dip of the EPGF can be varied in the triggering potential model (Section 3.4.4) until the highest cross-correlation (c.c.) value is found. This analysis could provide an estimate of the true dip of the EPGF.

3.4.7 Supplemental Information

3.4.7.1 Supplemental Figures

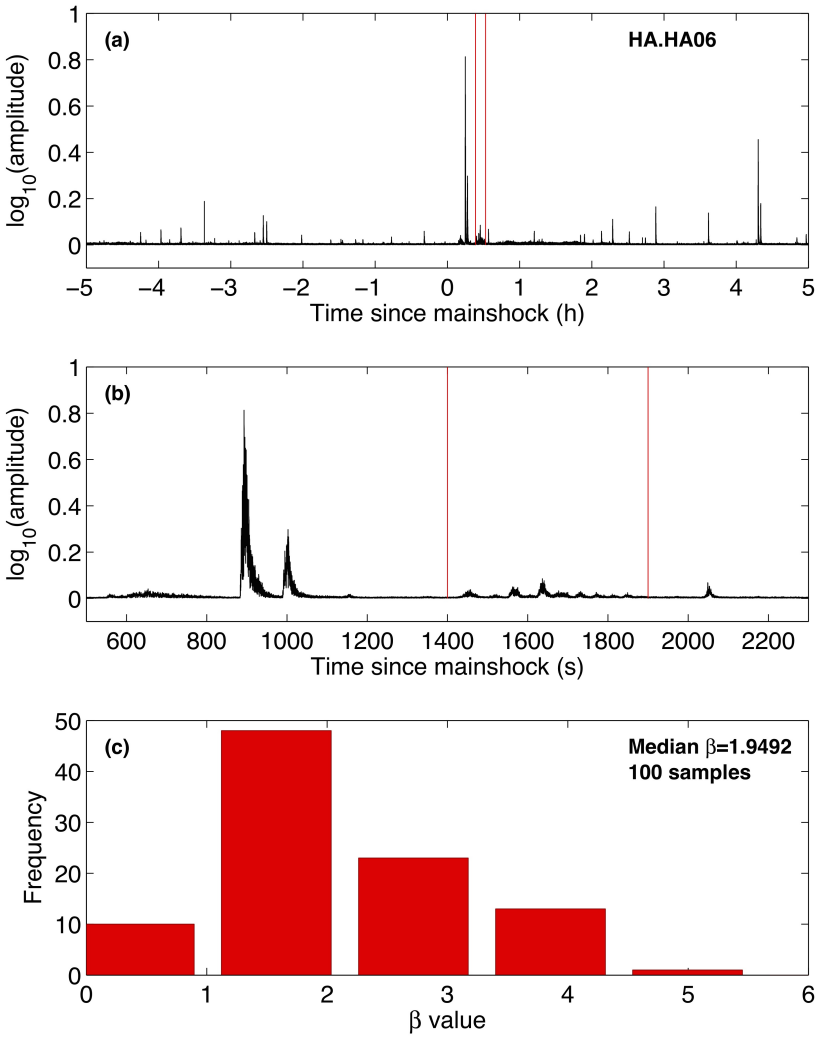

Figure S3.15 - β-point summation test of significance. **(a)** 4-component averaged 2-16 Hz band-pass filtered envelope from OBS station HA06 ± 5 hours around the Chile mainshock. Red lines = triggered tremor window. **(b)** Zoom-in to show triggered tremor window. Peaks around 900 s and 1000 s are Haiti aftershocks. **(c)** β-value distribution. Background time window is the same size as the triggering time window and was sampled 100 times from the 5 hours before the *P*-wave arrival (around 650 s in (b)) of the Chile mainshock.

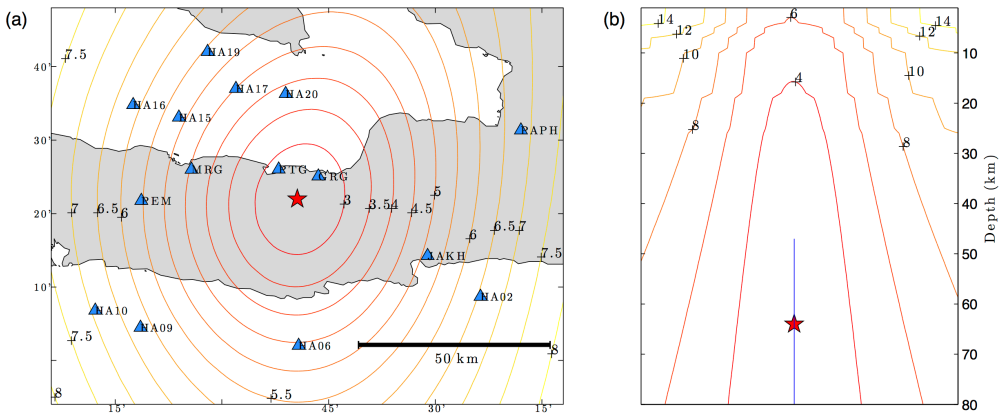

Figure S3.16 – Example of poorly constrained depth when locating triggered tremor sources. **(a)** Average horizontal location of burst # 5 (see Figure 3.17). The horizontal location for this burst is very near to the fault trace. **(b)** Average depth of burst # 5. Note that the error for the depth is quite large, i.e. ± 15 km.

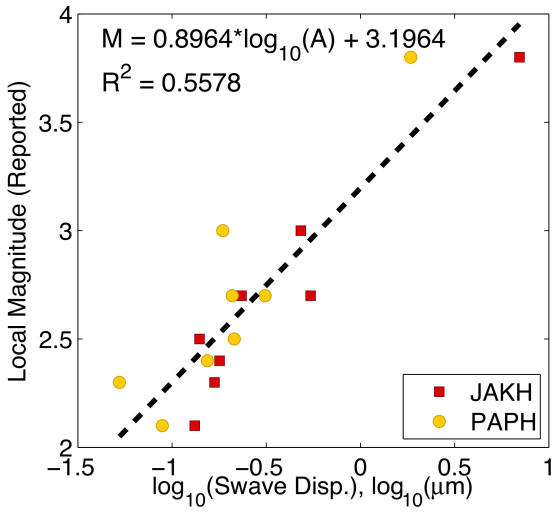

Figure S3.17 – Least square regression analysis for determining constants *a* and *b* in equation 3.2. We utilized 8 known earthquake magnitudes to determine calibrate the magnitudes of our hand-picked earthquakes. The reported magnitude is only weakly correlated to the displacement of the *S*-wave because (1) the waveforms were filtered and integrated for the *S*-wave displacement measurement and (2) because there is no amplitude attenuation term.

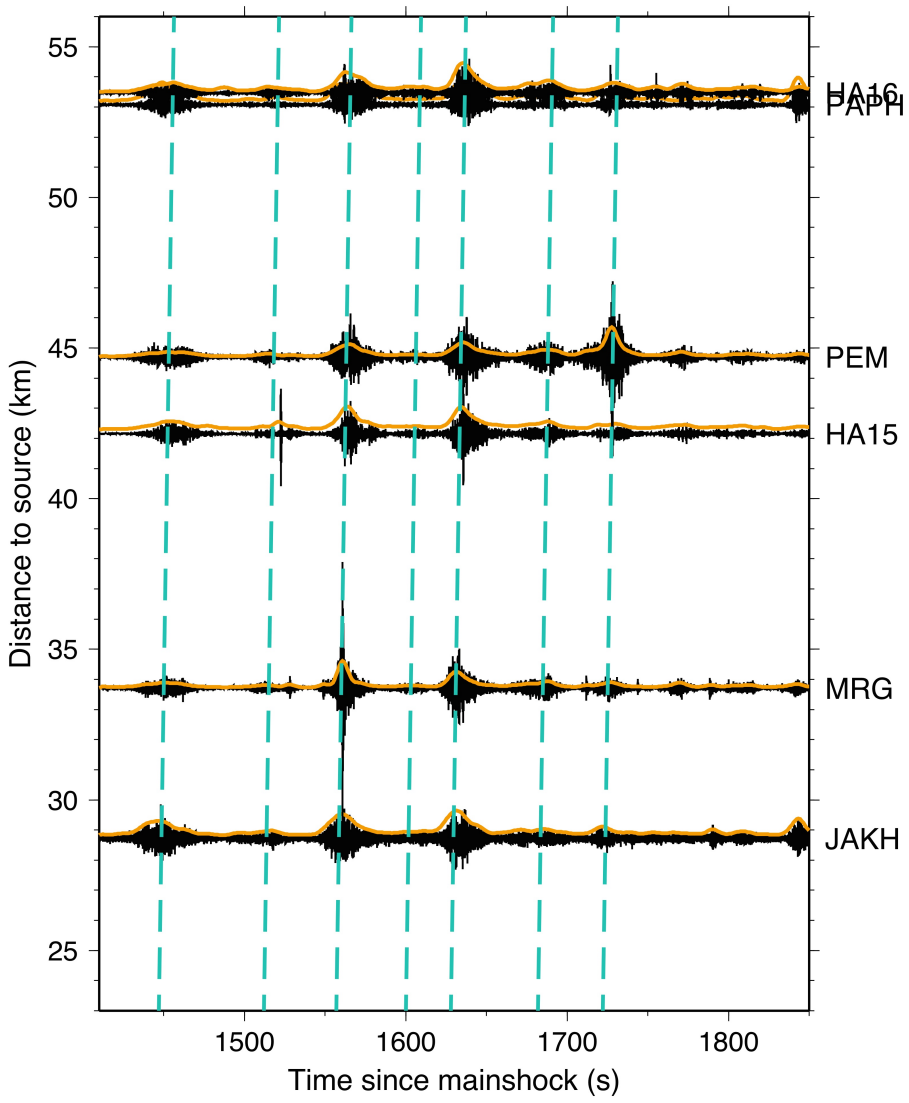

Figure S3.18 – Moveout of tremor activity triggered by the Chile mainshock. Black traces = 2-16 Hz band-pass filtered waveforms. Orange trace = envelope function of the filtered waveforms. Dashed lines = 3.5 km s^{-1} wave speed (i.e. speed of a *S*-wave).

3.4.7.2 Supplemental Tables

Table S3.6 – Earthquakes used for magnitude calibration.*

Time (UTC)	*Douilly et al.* [2013]		*CNSN*		*CNSN*
	Longitude	**Latitude**	**Longitude**	**Latitude**	**Magnitude**
06:48:48	-72.971362	18.497520	-73.055	18.581	3.0
09:27:07	-72.765527	18.419608	-72.883	18.465	2.3
10:10:47	-72.540630	18.521425	-72.644	18.597	2.1
10:52:10	-72.709439	18.503130	-72.775	18.561	2.7
12:37:39	-72.878059	18.405142	-73.031	18.477	2.4
15:57:10	-72.742828	18.483814	-72.858	18.530	3.8
17:40:30	-72.711628	18.471175	-72.847	18.525	2.7
20:22:03	-72.762724	18.427815	-72.902	18.469	2.5

*These events all occur on 27 February 2010 and are listed in both the CNSN and *Douilly et al.* [2013] catalogs.

3.4.7.3 Supplemental Movie

The supplemental movie of *Aiken et al.* [2015a] has been made available via http://geophysics.eas.gatech.edu/people/cautry6/temp/supplementals/dissertationCh3/ (last accessed 17 March 2015). Below is the caption associated with the movie.

Movie S3.3 - Tremor around the EPGF recorded at station CN.JAKH triggered by the 27 February 2010 *Mw*8.8 Chile earthquake. **(Top)** Broadband transverse-component seismogram recorded at the station JAKH. **(Middle)** 5 Hz high-pass-filtered transverse-component seismogram showing the P wave of the distant mainshock, aftershocks, and triggered tremor signals. **(Bottom)** Spectrogram of the transverse-component seismogram. A 0.5-Hz high-pass filter is applied to remove long-period signals before computing the spectrogram [*Peng et al.*, 2011]. The sound is generated by speeding up the seismic data by 100 times [*Kilb et al.*, 2012].

CHAPTER 4

AFTERTHOUGHTS

In this dissertation, several studies were presented on the topic of 'triggering by surface waves of large, distant earthquakes in active tectonic regions'. It was shown that seismic activity, such as earthquakes, tremor, and possibly even icequakes, can be repeatedly triggered by seismic waves of large, distant earthquakes. The works presented here sought to address four main questions: (1) What are the characteristics of the triggered activity? (2) What physical characteristics of the seismic waves are predominantly responsible for the triggered activity? (3) Are their differences in triggering behavior among regions with similar tectonic environments? and (4) Are their similarities/differences between earthquake and tremor triggering? The ultimate goal of this dissertation was to further explain the physical mechanisms responsible for the triggered seismic activity and clarify a region's susceptibility to triggering from transient stress changes.

Triggering of earthquakes has been explored in differing tectonic environments but has been predominantly observed in extensional environments such as geothermal/volcanic regions, where fluids are present and sometimes used for 'green' energy production. One study presented in this dissertation explored earthquake-earthquake interactions in Long Valley Caldera, Coso Geothermal Field, and Geysers Geothermal Field, three geothermal/volcanic regions of California that produce geothermal energy [*Aiken and Peng*, 2014]. In previous studies [e.g., *Prejean et al.*, 2004], triggered earthquake activity has been investigated in these geothermal regions but mostly on an event-by-event basis. My dissertation work examined triggering in these

geothermal/volcanic regions in a more systematic way (over a 12-year period) and illustrated that a region's susceptibility to triggering is proportional to its seismic activity rate. That is, a more seismically productive region (a region that is in a state of critical stress) is more susceptible/responsive to transient stressing and therefore is more easily pushed to failure (triggered).

Susceptibility of geothermal regions to triggering was also found to weakly correlate with heat flow measurements in Long Valley, Coso, and Geysers. The correlation is weak for a few reasons. First, heat flow measurements are not very accurate, as they do not account for heat flow due to convective heat transfer from fluid circulation. Second, heat flow measurements, geothermal energy production, and seismic activity rates in geothermal regions of California appear to be proportional with each other (geothermal production projections for California geothermal regions: http://www.energyalmanac.ca.gov/renewables/geothermal/). For example, cooler geothermal regions have lower energy production levels and lower earthquake productivity rates (at least over the 12-year period investigated here). Because heat flow, energy production, and seismic activity rates appear to be related, it would be interesting to further explore on smaller time scales which factor is predominantly responsible for triggering susceptibility. For example, one could search for the triggering of earthquakes during times of high seismicity rates.

Another contribution of the work presented here was the identification of tremor activity along strike-slip faults where tremor has not been previously observed. Prior to this dissertation, tremor along strike-slip faults was mainly observed in California along faults that are considered part of the San Andreas Fault plate boundary system [e.g.,

Gomberg et al., 2008]. In *Aiken et al.*, [2015b], tremor was uniquely identified on the eastern Denali Fault - a large, intraplate fault that is not intimately connected with a larger plate boundary. This finding opens the door for further exploration of tremor in intraplate settings where slip rates are generally lower than that of interplate settings. For instance, in the four studies of triggered tremor presented here, the minimum amount of transient stress needed to trigger tremor (triggering threshold) varied by strike-slip region. Varied triggering threshold could either be a result of fluid migration or changes in regional stress. Since fluid migration is observationally more difficult to pinpoint, a study of the regional slip rates using geodetic instrumentation could further elucidate whether or not the triggering threshold is related to the regional stress state. In other words, do regions with higher stress have lower triggering thresholds and do triggering thresholds vary proportional with regional stress?

In both types of triggering (earthquake and tremor) presented in this dissertation, the characteristics of the triggering seismic waves, such as amplitude and frequency, were also investigated and compared. In general, amplitude (peak ground velocity) of the triggering seismic waves was found to be a dominant factor controlling the triggering of earthquakes and tremor. However, these measurements are largely based on measurements of the peak ground velocity at the surface of the Earth and not at the depth at which the events are triggered. That is, since surface wave amplitude decreases with depth, a stress estimate from a peak ground velocity measurement at the surface is not a true representation of stress at depth, nor does it account for changes in stress due fluid pressurization. Dependence on amplitude could be further explored by modeling fluid pressurization at depth and its effect on peak ground velocity, as the presence of fluids is

generally considered to be a physical attribute of faults that reduces a fault's effective normal stress and promotes triggering.

With regard to frequency dependence on triggering, seismic waves with periods > 10 seconds were commonly observed to trigger tremor among strike-slip faults. However, no frequency dependence was observed for the triggering of earthquakes, even though in both cases the amplitude spectra were computed exactly the same, i.e. solely for the surface waves that promoted triggering. Truthfully, amplitude and frequency of the passing seismic waves both contribute to the triggering process and therefore should not be considered as individual factors as examined in this dissertation. In recent years, a triggering potential model was developed that incorporates fault orientation (strike and dip), depth of the triggered source, seismic wave amplitude, and seismic wave frequency [*Hill*, 2012; *Gonzalez-Huizar and Velasco*, 2011]. This model was implemented in *Aiken et al.* [2015a] to determine dynamic stress at depth (see Section 3.4.4). In theory, the triggering potential model could also be applied to a more complex tectonic system (e.g., a geothermal region) if the fault orientations and triggered source locations are known. In the geothermal study conducted here [*Aiken and Peng*, 2014], the earthquake locations and fault orientations were not known or investigated. It would be interesting to test the triggering potential model for triggered earthquakes in these geothermal regions to see if it can adequately describe the physical mechanisms responsible for the triggering of earthquakes.

APPENDIX A

METHOD FOR COMPUTING DYNAMIC STRESS FROM MAGNITUDE

Dynamic stresses generated by large, distant earthquakes can be estimated using surface wave magnitudes listed in earthquake catalogs, similar to *van der Elst and Brodsky* [2010]. The first step is to estimate the displacement by earthquake using the surface wave magnitude relation

$$\log_{10}(A_{20}) = M_S - 1.66\log_{10}(\Delta) - 2 \tag{A.1}$$

where A_{20} is displacement in micrometers and Δ is distance in degrees. Next, estimate the peak ground velocity (PGV) using the displacement:

$$PGV \approx \frac{2\pi}{T} A_{20} \tag{A.2}$$

where T is period. The dominant period of surface waves is T = 20 s for a surface wave generated by a remote source. The final step is to estimate dynamic stress (σ) from the peak ground velocity (PGV):

$$\sigma = \frac{(PGV)(\mu)}{v_{ph}} \tag{A.3}$$

where μ is shear rigidity, and v_{ph} is the phase velocity of the surface wave. Assuming crustal shear rigidity (μ = 35 GPa) and phase velocity of 3.5 km s^{-1}, equation A.3 can be reduced to

$$\sigma(\text{kPa}) = 100 * PGV(\text{cm s}^{-1}) \tag{A.4}$$

for a quick calculation, when peak ground velocity has units of cm s^{-1}.

APPENDIX B

EXAMPLE CODE FOR COMPUTING β- AND Z-STATISTICS USING MATLAB

```
function [ B, Z ] = compute_stat(Nb,Na,Tb,Ta)

% created by Chastity Aiken
% last modified August 23, 2013
%
% NOTE: This program computes the Beta and Z-statistic values as presented in Aron
% and Hardebeck [2009] and Marsan and Wyss [2011]. Full references for these
% articles are provided at the end of this introductory comment section.
%
% There are four inputs:
% Nb = number of events occurring in the time window before (background window)
% Na = number of events occurring in the time window after (triggering window)
% Tb = length of time window before (background window).
% Ta = length of time window after (triggering window)
%
% Tb and Ta do not need to be of equal length, but they must have the same unit (i.e.,
% seconds, minutes, hours, days, etc.).
%
% The code will display one Beta and one Z value on screen and store
% the variables so that they can be referenced later (as B and Z, respectively).
%
% USAGE:  [ B, Z ] = compute_stat(Nb,Na,Tb,Ta);
%
% EXAMPLE:
% Say, you identified 5 events occurring in your background window of 6 hours
% (Nb = 5; Tb = 6) and 50 events occurring in your triggering window of 6 hours
% (Na = 50; Ta = 6). Then,
%
% [ B, Z ] = compute_stat(5,50,6,6);
%
% The above example will provide a Beta value of 3.0 and a Z-value of 6.1.
%
% REFERENCES:
%
% Aron, A. and J. L. Hardebeck (2009), Seismicity rate changes along the central
% California coast due to stress changes from the 2003 M6.5 San Simeon and 2004
% M6.0 Parkfield earthquakes, B. Seismol. Soc. Am., 99, no. 4, pp. 2880-2292,
% doi: 10.1785/0120080239.
%
% Marsan, D. and M. Wyss (2011), Seismicity rate changes, Community Online
% Resource for Statistical Seismicity Analysis, doi: 10.5078/corssa-25837590. Available
% at http://www.corssa.org (Theme V).
```

```
%% INITIALIZE
N = Na + Nb;
T = Ta + Tb;

%% COMPUTE BETA [Aron and Hardebeck, 2009]
B = (Na - N*(Ta /T))/sqrt(N*(Ta/T)/(1-Ta/T));

%% COMPUTE Z [Marsan and Wyss, 2011]
Z = (Na*Tb - Nb*Ta)/sqrt(Na*Tb^2 + Nb*Ta^2);

%% PRINT RESULTS TO SCREEN
fprintf('--------------------\n')
fprintf('Beta:  %.1f\n',B)
fprintf('Z:  %.1f\n',Z)
```

APPENDIX C

LIST OF PAPERS PUBLISHED DURING PH.D.

(Papers are listed with most recent first.)

Aiken, C., J. P. Zimmerman, Z. Peng, and J. I. Walter (2014), Triggered seismic events along the Eastern Denali Fault in northwest Canada following the 2012 *Mw*7.8 Haida Gwaii, 2013 *Mw*7.5 Craig, and two *Mw* > 8.5 teleseismic earthquakes, *B. Seismol. Soc. Am.*, **105**(2b), doi: 10.1785/0120140156, in press.

Aiken, C. and Z. Peng (2014), Dynamic triggering of microearthquakes in three geothermal regions of California, *J. Geophys. Res.*, **119**, no. 9, 6992-7009, doi: 10.1002/2014JB011218.

Chao, K., Z. Peng, H. Gonzalez-Huizar, C. Aiken, B. Enescu, H. Kao, A. A. Velasco, K. Obara, and T. Matsuzawa (2013), Global Search of Triggered Tremor Following the 2011 Mw9.0 Tohoku-Oki Earthquake, *B. Seismol. Soc. Am.*, doi:10.1785/0120120171.

Aiken, C., Z. Peng, and K. Chao (2013), Tremors along the Queen Charlotte margin triggered by large teleseismic earthquakes, *Geophys. Res. Lett.*, **40**, 829-834, doi: 10.1002/GRL50220.

Peng, Z., H. Gonzalez-Huizar, K. Chao, C. Aiken, B. Moreno, G. Armstrong (2013), Tectonic Tremor in Cuba Triggered by Large Teleseismic Earthquakes, *B. Seismol. Soc. Am.*, **103**(1), 595-600, doi: 10.1785/0120120253

Hill, D.P., Z. Peng, D.R. Shelly, and C. Aiken (2013), S-wave triggering of tremor beneath the Parkfield, CA, section of the San Andreas Fault by the 2011 Tohoku-Oki Japan earthquake: observations and theory, *B. Seismol. Soc. Am.*, **103**(2b), 1541-1550, doi: 10.1785/0120120114.

.

Peng, Z., C. Aiken, D. Kilb, D. R. Shelly, and B. Enescu (2012), Listening to the 2011 magnitude 9.0 Tohoku-Oki, Japan earthquake, *Seismol. Res. Lett,* **83**(2), 287-293, doi:10.1785/gssrl.83.2.287.

Aiken, C. and J. Veras (2012), An Inverse Source Problem in Near Zero Frequency Sounding of Layered Media, *Fixed Point Theory*, **13**, no. 1, pp. 11-21.

Shelly, D. R., Z. Peng, D. P. Hill and C. Aiken (2011), Triggered creep as a possible mechanism for delayed dynamic triggering of tremor and earthquakes, *Nat. Geosci.*, **4**, pp. 384-388, doi:10.1038/ngeo1141.

Peng, Z., C. Wu, and C. Aiken (2010), Delayed triggering of microearthquakes by multiple surface waves circling the Earth, *Geophys. Res. Lett.*, **38**, L04306, doi:10.1029/2010GL046373.

Peng, Z., D. P. Hill, D. R. Shelly, C. Aiken (2010), Remotely triggered microearthquakes and tremor in Central California following the 2010 Mw 8.8 Chile Earthquake, *Geophys. Res. Lett.*, **37**, L24312, doi:10.1029/2010GL045462.

REFERENCES

Aiken, C. and Z. Peng (2014), Dynamic triggering of microearthquakes in three geothermal regions of California, *J. Geophys. Res.,* **119**, no. 9, pp. 6992-7009, doi: 10.1002/2014JB011218.

Aiken, C., Z. Peng , and K. Chao (2013a), Tremors along the Queen Charlotte margin triggered by large teleseismic earthquakes, *Geophys. Res. Lett.*, **40**, pp. 829-834, doi: 10.1002/GRL50220.

Aiken, C., Z. Peng, D. R. Shelly, D. P. Hill, H. Gonzalez-Huizar, K. Chao, J. P. Zimmerman, R. Douilly, A. Deschamps, J. Haase, E. Calais (2013b), Tectonic tremor triggered along major strike-slip faults around the world, AGU Fall Meeting, abstract S51B-2362, San Francisco, California, 9-13 Dec.

Aiken, C., Z. Peng, K. Chao, R. Douilly, A. Deschamps, E. Calais, and J. Haase (2015a), Effect of the 2010 *Mw*8.8 Maule, Chile earthquake on fault structures in the southern Haiti peninsula, *Earth Planet. Sci. Lett.,* manuscript in preparation.

Aiken, C., J. P. Zimmerman, Z. Peng, and J. I. Walter (2015b), Triggered seismic events along the Eastern Denali Fault in northwest Canada following the 2012 Mw7.8 Haida Gwaii, 2013 Mw7.5 Craig, and two *Mw* > 8.5 teleseismic earthquakes, *B. Seismol. Soc. Am.*, **105**, no. 2b, doi: 10.1785/0120140156.

Aron, A. and J. L. Hardebeck (2009), Seismicity Rate Changes along the Central California Coast due to Stress Changes from the 2003 *M*6.5 San Simeon and 2004 *M*6.0 Parkfield earthquakes, *B. Seismol. Soc. Am.*, **99**, no. 4, pp. 2880-2292, doi: 10.1785/0120080239.

Bakun, W. H., C. H. Flores, and S. Uri (2012), Significant earthquakes on the Enriquillo fault system, Hispaniola, 1500-2010: Implications for seismic hazard, *B. Seismol. Soc. Am.,* **102**, no. 1, pp. 18-30, doi: 10.1785/0120110077.

Bartlow, N. M., D. A. Lockner, and N. M. Beeler (2012), Laboratory triggering of stick-slip events by oscillatory loading in the presence of pore fluid with implications for physics of tectonic tremor, *J. Geophs. Res.*, **117**, B11411, doi: 10.1029/2012JB009452.

Becken, M., O. Ritter, P. A. Bedrosian, and U. Weckmann (2011), Correlation between deep fluids, tremor and creep along the central San Andreas fault, *Nature*, **480**, doi: 10.1038/nature10609.

Beroza, G. C. and S. Ide (2011), Slow earthquakes and nonvolcanic tremor, *Annu. Rev. Earth Planet. Sci.*, **39**, pp. 271-296, doi 10.1146/annurev-earth-040809-152531.

Bertani, R. (2012), Geothermal power generation in the world 2005-2010 update report, *Geothermics*, **41**, pp. 1-29. doi: 10.1016/j.geothermics.2011.10.001.

Bhattacharyya, J. and J. M. Lees (2002), Seismicity and seismic stress in the Coso Range, Coso geothermal field, and Indian Wells Valley region, southeast-central California, *in* A.F. Glazner, J. D. Walker, and J. M. Bartley, eds., Geologic Evolution of the Mojave Desert and Southwestern Basin and Range: Boulder, Colorado, Geological Society of America Memoir **195**, pp. 243-257.

Brodsky, E. E. (2006), Long-range triggered earthquakes that continue after the wave train passes, *Geophys. Res. Lett.*, **33**, L15313, doi: 10.1029/2006GL026605.

Brodsky, E. E. and S. G. Prejean (2005), New constraints on mechanisms of remotely triggered seismicity at Long Valley Caldera, *J. Geophys. Res.*, **110**, B04302, doi:10.1029/2004JB003211.

Brodsky, E. E. and N. J. van der Elst (2014), The Uses of Dynamic Earthquake Triggering, *Annu. Rev. Earth and Pl. Sc.*, **42**, pp. 317-339, doi: 10.1146/annurev-earth-060313-054648.

Brown, J. R., S. G. Prejean, G. C. Beroza, J. S. Gomberg, and P. J. Haeussler (2013), Deep low-frequency earthquakes in tectonic tremor along the Alaska-Aleutian subduction zone, *J. Geophys. Res.*, **118**, pp. 1079–1090, doi:10.1029/2012JB009459.

Bustin, A. M. M., R. D. Hyndman, H. Kao, and J. F. Cassidy (2007), Evidence for underthrusting beneath the Queen Charlotte Margin British Columbia, from teleseismic receive function analysis, *Geophys. J. Int.*, **171**, 1198-1211, doi:10.1111/j.1365-246X.2007.03583.x

Calais, E., A. Freed, G. Mattioli, F. Amelung, S. Jónsson, P. Jansma, S-H. Hong, T. Dixon, C. Prépetit, and R. Momplaisir (2010), Transpressional rupture of an unmapped fault during the 2010, Haiti earthquake, *Nature Geosci*., **3**, doi:/10.1038/ngeo992.

Chao, K. and K. Obara (2012), Widespread triggered tremor in Japan following the 2012 Mw8.6 Sumatra earthquake, AGU Fall Meeting, abstract S41D-06, San Francisco, California, 3-7 Dec.

Chao, K., Z. Peng, A. Fabian, and L. Ojha (2012a), Comparisons of Triggered Tremor in California, *B. Seismol. Soc. Am.*, **102**, no. 2, pp. 900-908, doi: 10.1785/0120110151.

Chao, K., Z. Peng, H. Gonzalez-Huizar, C. Aiken, B. Enescu, H. Kao, A. A. Velasco, K. Obara, and T. Matsuzawa (2013), Global search of triggered tremor following the 2011 Mw9.0 Tohoku-Oki earthquake, *B. Seismol. Soc. Am.*, **103**, no. 2B, doi: 10.1785/0120120171.

Chao, K., Z. Peng, C. Wu, C-C. Tang, and C. Lin (2012b), Remote triggering of non-volcanic tremor around Taiwan, *Geophys. J. Int.*, **188**, pp. 301–324, doi: 10.1111/j.1365-246X.2011.05261.x.

Cochran, E. S., J. E. Vidale, S. Tanaka (2004), Earth tides can trigger shallow thrust fault earthquakes, *Science*, **306**, no. 5699, pp. 1164-1166, doi: 10.1126/science.1103961.

DeMets, C., R. G. Gordon, D. F. Argus (2010), Geologically current plate motions, *Geophys. J. Int.*, **181**, pp. 1-80, doi:10.1111/j.1365-246X.2009.04491.x.

Doran, A. K., Z. Peng, X. Meng, C. Wu, D. Kilb (2011), Dynamic triggering of earthquakes in the Salton Trough of southern California, *Seismol. Res. Lett.*, **82**, no. 2, SSA Spring Meeting Suppl.

Douilly, R., J. S. Haase, W. L. Ellsworth, M. P. Bouin, E. Calais, S. Symithe, J. G. Armbruster, B. Mercier de Lépinay, A. Deschamps, S. L. Mildor et al. (2013), Improving the resolution of the 2010 Haiti earthquake fault geometry using temporary seismometer deployments, *B. Seismol. Soc. Am.*, 103, no. 4, pp. 2035-2325, doi: 10.1785/0120120303.

Eberhart-Phillips, D., P. J. Haeussler, J. T. Freymueller, A. D. Frankel, C. M. Rubin, P. Craw, N. A. Ratchkovski, G. Anderson, G. A. Carver, A. J. Crone et al. (2003), The 2002 Denali Fault earthquake, Alaska : a large magnitude, slip-partitioned event, *Science*, **300**, pp. 1113-1118, doi : 10.1126/science.1082703.

Enescu, B., K. Chao, K. Obara, Z. Peng, and T. Matsuzawa, and Y. Yagi (2013), Remote Love wave triggering of tremor in the Nankai subduction zone: New observations and dynamic stress modeling, AGU Fall Meeting, abstract S42B-03, San Francisco, California, 9-13 Dec.

Felzer, K. R. and E. E. Brodsky (2006), Decay of aftershock density with distance indicates triggering by dynamic stress, *Nature*, **441**, pp. 735-738, doi: 10.1038/nature04799.

Freed, A. M. (2005), Earthquake triggering by static, dynamic, and postseismic stress transfer, *Annu. Rev. Earth. Pl. Sc.*, **33**, pp. 335-367, doi: 10.1146/annurev.earth.33.092203.122505.

Fry, B., K. Chao, S. Bannister, and Z. Peng (2011), Deep tremor in New Zealand triggered by the 2010 Mw8.8 Chile earthquake, *Geophys. Res. Lett.*, **38**, L15306, doi: 10.1029/2011GL048319.

Ghosh, A., J. E. Vidale, Z. Peng, K. C. Creager, and H. Houston (2009), Complex nonvolcanic tremor near Parkfield, California, triggered by the great 2004 Sumatra earthquake, *J. Geophys. Res.*, **114**, B00A15, doi:10.1029/2008JB006062.

Gomberg, J. and S. Prejean (2013), Triggered tremor sweet spots in Alaska, *J. Geophys. Res.*, **118**, pp. 6203-6218, doi :10.1002/2013JB010273.

Gomberg, J., S. Prejean, and N. Ruppert (2012), Afterslip, Tremor, and the Denali Fault Earthquake, *B. Seismol. Soc. Am.*, **102**, no. 2, pp. 892-899, doi: 10.1785/0120110142.

Gomberg, J., J. L. Rubinstein, Z. Peng, K. C. Creager, J. E. Vidale, and P. Bodin (2008), Widespread triggering of nonvolcanic tremor in California, *Science*, **319**, no. 5860, p. 173, doi: 10.1126/science.1149164.

Gonzalez-Huizar, H. and A. A. Velasco (2011), Dynamic triggering : Stress modeling and a case study, *J. Geophys. Res.*, **116**, no. B2, doi : 10.1029/2009JB007000.

Gonzalez-Huizar, H., A. A. Velasco, Z. Peng, and R. R. Castro (2012), Remote triggered seismicity caused by the 2011, M9.0 Tohoku-Oki, Japan earthquake, *Geophys. Res. Lett.*, **39**, no. 10, doi : 10.1029/2012GL051015.

Guilhem, A., Z. Peng, and R. M. Nadeau (2010), High-frequency identification of non-volcanic tremor triggered by regional earthquakes, *Geophys. Res. Lett.*, **37**, L16309, doi: 10.1029/2010GL044660.

Harris, R., R. Simpson, and P. Reasenberg (1995), Influence of static stress changes on earthquake locations in southern California, *Nature*, **375**, pp. 221-224.

Hayes, G. P., R. W. Briggs, E. J. Fielding, C. Prentice, K. Hudnut, P. Mann, F. W. Taylor, A. J. Crone, R. Gold, T. Ito, and M. Simons (2010), Complex rupture during the 12 January 2010 Haiti earthquake, *Nature Geosci.*, **3**, doi:10.1038/ngeo977.

Hill, D. P. (2006), Unrest in Long Valley Caldera, California, 1978-2004, *in* C. Troise, G. De Natale, and C. R. J. Kilburn (eds.) Mechanisms of Activity and Unrest at Large Calderas, Geological Society, London, Special Publications, **269**, pp. 1-24.

Hill, D. P. (2012), Surface wave potential for triggering tectonic (non-volcanic) tremor - corrected, *B. Seismol. Soc. Am.*, **102**, pp. 2337-2355, doi:10.1785/0120120086.

Hill, D. P., Z. Peng, D. R. Shelly, and C. Aiken (2013), S-wave triggering of tremor beneath the Parkfield, CA, section of the San Andreas Fault by the 2011 Tohoku-Oki Japan earthquake: observations and theory, *B. Seismol. Soc. Am.*, **103**, no. 2b, doi: 10.1785/0120120114.

Hill, D. P. and S. G. Prejean (2014), Dynamic Triggering, in *Treatise on Geophysics* 2nd edition (G. Schubert, ed.), Chapter 8 in Volume **4**, "Earthquake Seismology" (H. Kanamori, ed.), Elsevier, Amsterdam.

Hill, D. P., P. A. Reasenberg, A. Michael, W. J. Arabaz, G. Beroza, D. Brumbaugh, J. N. Brune, R. Castro, S. Davis, D. dePolo et al. (1993), Seismicity Remotely Triggered by the Magnitude 7.3 Landers, California, Earthquake, *Science*, **260**, no. 5114, pp. 1617-1623.

Hill, D. P., Z. Peng, D. R. Shelly, and C. Aiken (2013), *S*-wave triggering of tremor beneath the Parkfield, California, section of the San Andreas fault by the 2011 Tohoku, Japan, earthquake: Observations and theory, *B. Seismol. Soc. Am.*, **103**, no. 2B, doi: 10.1785/0120120114.

Hirose, H., H. Kimura, B. Enescu, and S. Aoi (2012), Recurrent slow slip event likely hastened by the 2011 Tohoku earthquake, *Pro. Natl. Acad. Sci. Unit. States Am.*, **109**, no. 38, pp. 15157-15161, doi: 10.1073/pnas.1202709109.

Hough, S. E. and H. Kanamori (2002), Source properties of earthquakes near Salton Sea triggered by the 16 October 1999 M7.1 Hector Mine, California, earthquake, *B. Seismol. Soc. Am.*, **92**, no. 4, pp. 1281-1289, doi: 10.1785/0120000910.

Jiang, T., Z. Peng, W. Wang, and Q.-F. Chen (2010), Remotely triggered seismicity in Continental China by the 2008 Mw7.9 Wenchuan earthquake, *B. Seismol. Soc. Am.*, **100**, no. 5b, pp. 5274-5289, doi: 10.1785/0120090286.

Kane, D. L., D. Kilb, A. S. Berg, and V. G. Martynov (2007), Quantifying the remote triggering capabilities of large earthquakes using data from the ANZA Sesimic Network catalog (southern California), *J. Geophys. Res.*, **112**, B11302, doi: 10.1029/2006JB004714.

Kao, H., S.-J. Shan, A. Bent, C. Woodgold, G. Rogers, J. F. Cassidy, and J. Ristau (2012), Regional centroid-moment-tensor analysis for earthquakes in Canada and adjacent regions: An update, *Seismol. Res. Lett.*, **83**, pp. 505-515, doi: 10.1785/gssrl.83.3.505.

Kilb, D., J. Gomberg, and P. Bodin (2000), Triggering of earthquake aftershocks by dynamic stresses, *Nature*, **408**, pp. 570-574, doi: 10.1038/35046046.

King, G., R. Stein, and J. Lin (1994), Static stress changes and the triggering of earthquakes, *B. Seismol. Soc. Am.*, **84**, no. 3, pp. 935-953.

Lamontagne, M, S. Halchuk, J. F. Cassidy, and G. C. Rogers (2008), Significant Canadian Earthquakes of the Period 1600-2006, *Seismo. Res. Lett.*, **79**, no. 2, pp. 211-223, doi:10.1785/gssrl.79.2.211.

Lay, T., L. Ye, H. Kanamori, Y. Yamazaki, K. F. Cheung, K. Kwong, and K. D. Koper (2013), The October 28, 2012 Mw7.8 Haida Gwaii underthrusting earthquake and tsunami: Slip partitioning along the Queen Charlotte Fault transpressional plate boundary, *Earth Planet. Sci. Lett.*, **375**, pp. 57-70, doi: 10.1016/j.epsl.2013.05.005.

Manaker, D. M., E. Calais, A. M. Freed, S. T. Ali, P. Przybylski, G. Mattioli, P. Jansma, C. Prépetit, and J-B. de Chabalier (2008), Interseismic plate coupling and strain partitioning in the northeastern Caribbean, *Geophys. J. Int.*, **98**, no. 1, doi:10.111/j.1365-246X.1989.tb05513.x.

Meighan, L., J. F. Cassidy, S. Mazzoti, and G. Pavlis (2013), Microseismicity and tectonics of southwest Yukon territory, Canada using a local dense seismic array, *B. Seismol. Soc. Am.*, **103**, no. 6, pp. 3341-3346, doi: 10.1785/0120130068.

Mercier de Lépinay, B., A. Deschamps, F. Klingelhoefer, Y. Mazabraud, B. Delouis, V. Clouard, Y. Hello, J. Crozon, B. Marcaillow, D. Graindorge, M. Vallée, J. Perrot, M-P. Bouin, J-M. Saurel, P. Charvis, and M. St-Louis (2011), The 2010 Haiti earthquake: A complex fault pattern constrained by seismologic and tectonic observations, *Geophys. Res. Lett.*, **38**, L22305, doi:10.1029/2011GL049799.

Miyazawa, M., E. E. Brodsky, and J. Mori (2008), Learning from dynamic triggering of low-frequency tremor in subduction zones, *Earth Planets Space*, **60**, e17-e20.

Nadeau, R. M. and A. Guilhem (2009), Nonvolcanic tremor evolution and the San Simeon and Parkfield, California, earthquakes, *Science*, **325**, pp. 191-193, doi: 10.1126/science.1174155.

Nettles, M. and G. Ekström (2010), Glacial Earthquakes in Greenland and Antarctica, *Annu. Rev. Earth Planet. Sci.*, **38**, pp. 467-491, doi: 10.1146/annurev-earth-040809-152414.

Obara, K. (2002), Nonvolcanic deep tremor associated with subduction in southwest Japan, Science, **296**, pp. 1679-1681, doi: 10.1126/science.1070378.

Parsons, T., M. Segou, and W. Marzocchi (2014), The global aftershock zone, *Tectonophysics*, **618**, doi: 10.1016/j.tecto.2014.01.038.

Peng, Z. and J. Gomberg (2010), An integrated perspective of the continuum between earthquakes and slow-slip phenomena, *Nat. Geosci.*, **3**, pp. 599-607, doi: 10.1038/ngeo940.

Peng, Z., C. Aiken, D. Kilb, D. R. Shelly, and B. Enescu (2012), Listening to the 2011 magnitude 9.0 Tohoku-Oki earthquake, *B. Seismol. Soc. Am.*, **103**, no. 2b, doi : 10.1785/0120120171.

Peng, Z., H. Gonzalez-Huizar, K. Chao, C. Aiken, B. Moreno, and G. Armstrong (2013), Tectonic tremor beneath Cuba triggered by the Mw8.8 Maule and Mw9.0 Tohoku-Oki earthquakes, *B. Seismol. Soc. Am.*, **103**, no. 1, pp. 595-600, doi: 10.1785/0120120253.

Peng, Z., D. P. Hill, D. R. Shelly, and C. Aiken (2010), Remotely triggered microearthquakes and tremor in central California following the 2010 M_w8.8 Chile earthquake, *Geophys. Res. Lett.*, **37**, L24312, doi: 10.1029/2010GL045462.

Peng. Z., J. E. Vidale, K. C. Creager, J. L. Rubinstein, J. Gomberg, and P. Bodin (2008), Strong tremor near Parkfield, CA excited by the 2002 Denali Fault earthquake, *Geophys. Res. Lett.*, **35**, L23305, doi:10.1029/2008GL03608.

Peng, Z., J. E. Vidale, M. Ishii, and A. Helmstetter (2007), Seismicity rate immediately before and after main shock rupture from high-frequency waveforms in Japan, *J. Geophys. Res.*, **112**, no. B3, doi: 10.1029/2006JB004386.

Peng. Z., J. E. Vidale, A. G. Wech, R. M. Nadeau, and K. C. Creager (2009), Remote triggering of tremor along the San Andreas Fault in central California, *J. Geophys. Res.*, **114**, B00A06, doi:10.1029/2008JB006049.

Peng, Z., D. P. Hill, D. Shelly, and C. Aiken (2010), Remotely triggered microearthquakes and tremor in Central California following the 2010 *Mw*8.8 Chile Earthquake, *Geophys. Res. Lett.*, **37**, L24312, doi:10.1029/2010GL045462.

Peng, Z., J. I. Walter, R. Aster, A. Nyblade, D. A. Wiens, and S. Anandakrishnan (2014), Antarctic icequakes triggered by the 2010 Maule earthquake in Chile, *Nat. Geosci.*, **7**, pp. 677-681, doi: 10.1038/ngeo2212.

Peng, Z., C. Wu, and C. Aiken (2011), Delayed triggering of microearthquakes by multiple surface waves circling the Earth, *Geophys. Res. Lett.*, **38**, L04306, doi: 10.1029/2010GL046373.

Peng, Z. and P. Zhao (2009), Migration of early aftershocks following the 2004 Parkfield earthquake, *Nature Geosci.*, **2**, pp. 877-881, doi: 10.1038/ngeo697.

Peterson, C. L., and D. H. Christensen (2009), Possible relationship between nonvolcanic tremor and the 1998–2001 slow slip event, south central Alaska, *J. Geophys. Res.*, **114**, B06302, doi:10.1029/2008JB006096.

Pollitz, F. F., R. S. Stein, V. Sevilgen, and R. Bürgmann (2012), The 11 April 2012 east Indian Ocean earthquake triggered large aftershocks worldwide, *Nature*, **490**, pp. 250-253, doi:10.1038/nature11504.

Prejean, S. G., D. P. Hill, E. E. Brodsky, S. E. Hough, M. J. S. Johnston, S. D. Malone, D. H. Oppenheimer, A. M. Pitt, and K. B. Richards-Dinger (2004), Remotely Triggered Seismicity on the United States West Coast following the M_w7.9 Denali Fault Earthquake, *B. Seismol. Soc. Am.*, **94**, no. 6B, pp. S348-S359, doi: 10.1785/0120040610.

Prentice, C. S., P. Mann, A. J. Crone, R. D. Gold, K. W. Hudnut, R. W. Briggs, R. D. Koehler and P. Jean (2010), Seismic hazard of the Enriquillo-Plantain Garden fault in Haiti inferred from paleoseismology, *Nature Geosci.*, **3**, pp. 789-793, doi: 10.1038/ngeo991.

Rohr, K. M. M. and A. J. Tryon (2010), Pacific-North America plate boundary reorganization in response to a change in relative plate motion: Offshore Canada, *Geochem. Geophys. Geosy.*, **11**, Q06007, doi: 10.1029/2009GC003019.

Rubinstein, J. L., J. E. Vidale, J. Gomberg, P. Bodin, K. C. Creager, and S. D. Malone (2007), Non-volcanic tremor driven by large transient shear stresses, *Nature*, **448**, pp. 579-582, doi: 10.1038/nature06017.

Rubinstein, J. L., J. Gomberg, J. E. Vidale, A. G. Wech, H. Kao, K. C. Creager, and G. Rogers (2009), Seismic wave triggering of nonvolcanic tremor, episodic tremor and slip, and earthquakes on Vancouver Island, *J. Geophys. Res.*, **114**, no. B2, doi: 10.1029/2008JB005875.

Shelly, D. R. (2009), Possible deep fault slip preceding the 2004 Parkfield earthquake, inferred from detailed observations of tectonic tremor, *Geophys. Res. Lett.,* **36**, L17318, doi:10.1029/2009GL039589.

Shelly, D. R., G. C. Beroza, and S. Ide (2007), Non-volcanic tremor and low-frequency earthquake swarms, *Nature*, **446**, no. 7133, pp. 305-307, doi: 10.1038/nature05666.

Shelly, D. R., G. C. Beroza, S. Ide, and S. Nakamula (2006), Low-frequency earthquakes in Shikoku, Japan, and their relationship to episodic tremor and slip, *Nature*, **442**, no. 7099, pp. 188-191, doi: 10.1038/nature04931.

Shelly, D. R., W. L. Ellsworth, T. Ryberg, C. Haberland, G. S. Fuis, J. Murphy, R. M. Nadeau, and R. Bürgmann (2009), Precise location of San Andreas Fault tremors near Cholame, California using seismometer clusters: Slip on the deep extension of the fault?, *Geophys. Res. Lett*., **36**, L01303, doi:10.1029/2008GL036367.

Shelly, D. R. and J. L. Hardebeck (2010), Precise tremor source locations and amplitude variations along the lower-crustal central San Andreas Fault, *Geophys. Res. Lett.*, **37**, 14, doi: 10.1029/2010GL043672.

Shelly, D. R., Z. Peng, D. P. Hill, and C. Aiken (2011), Triggered creep as a possible mechanism for delayed dynamic triggering of tremor and earthquakes, *Nature Geosci.*, **4**, pp. 384-388, doi: 10.1038/ngeo1141.

Sibson, R. H. (2012), Reverse fault rupturing: competition between non-optimal and optimal fault orientations, *Geological Society*, London, Special Publications, **367**, pp. 39-50, doi: 10.1144/SP367.4.

Smith, E. F. and J. Gomberg (2009), A Search in Strainmeter Data for Slow Slip Associated with Triggered and Ambient Tremor near Parkfield, California, *J. Geophys. Res.*, **113**, B00A14, doi:10.1029/2008JB006040.

Stark, M. and S. Davis (1996), Remotely triggered microearthquakes at The Geysers geothermal field, California, *Geophys. Res. Lett.*, **23**, no. 9, doi:10.1029/96GL00011.

Sullivan, B., Z. Peng, C. Wu, and C. Aiken (2012), Delayed triggering of earthquakes by multiple waves circling the Earth, *Seismol. Res. Lett.*, **82**, no. 278, Spring Meet. Suppl.

Tape, C., M. West, V. Silwal, and N. Ruppert (2013). Earthquake Nucleation and Triggering on an Optimally Oriented Fault, *Earth Planet. Sci. Lett.*, **363**, doi: 10.1016/j.epsl.2012.11.060.

Thomas, A. M., R. Burgmann, D. R. Shelly, N. M. Beeler, and M. L. Rudolph (2012), Tidal sensitivity of low frequency earthquakes near Parkfield, CA: implications for fault mechanics within the brittle-ductile transition, *J. Geophys. Res.*,**117**, B05301, doi: 10.1029/2011JB009036.

van der Elst, N. J. and E. E. Brodsky (2010), Connecting near-field and far-field earthquake triggering to dynamic strain, *J. Geophys. Res.*, **115**, B07311, doi:10.1029/2009JB006681.

Velasco, A. A., S. Hernandez, T. Parsons, K. Pankow (2008), Global ubiquity of dynamic earthquake triggering, *Nature Geosci.*, **1**, pp. 375 - 379, doi:10.1038/ngeo204.

Vidale, J. E., D. C. Agnew, M. J. S. Johnston, and D. H. Oppenheimer (1998), Absence of earthquake correlation with Earth tides: An indication of high preseismic fault stress rate, *J. Geophys. Res.*, **103**, no. B10, pp. 24567-24572, doi: 10.1029/98JB00594.

Wang, T.-H., E. S. Cochran, D. Agnew, and D. D. Oglesby (2013), Infrequent triggering of tremor along the San Jacinto fault near Anza, California, *B. Seismol. Soc. Am.*, **103**, no. 4, pp. 2482-2497, doi: 10.1785/0120120284.

Wech, A. G., C. M. Boese, T. A. Stern, and J. Townsend (2012), Tectonic tremor and deep slow slip on the Alpine Fault, *Geophys. Res. Lett.*, **39**, L10303, doi: 10.1029/2012GL051751.

West, M. (2014). Tracking glaciers with the Alaska Seismic Network, *Seismol. Res. Lett.*, **85**, no. 2, p. 477.

West, M., J. J. Sanchez, and S. R. McNutt (2005), Periodically Triggered Seismicity at Mount Wrangell, Alaska, After the Sumatra Earthquake, *Science*, **308**, pp. 1144-1146, doi: 10.1126/science.1112462.

Worthington, L. L., H. J. A. Van Avendonk, S. P. S. Gulick, G. L. Christeson, and T. L. Pavlis (2012), Crustal structure of the Yakutat terrane and the evolution of subduction and collision in southern Alaska, *J. Geophys. Res.*, **117**, B01102, doi: 10.1029/2011JB008493.

Wu, J., Z. Peng, W. Wang, X. Gong, Q. Chen, and C. Wu (2012), Comparisons of dynamic triggering near Beijing, China following recent large earthquakes in Sumatra, *Geophys. Res. Lett.*, **39**, L21310, doi:10.1029/2012GL053515.

Yang, H. and Z. Peng (2013), Lack of additional triggered tectonic tremor around the Simi Valley and the San Gabriel Mountain in southern California, *B. Seismol. Soc. Am.*, **103**, no. 6, pp. 3372-3378, doi: 10.1785/0120130117.

Zigone, D., D. Rivet, M. Radiguet, M. Campillo, C. Voisin, N. Cotte, A. Walpersdorf, N. Shapiro, G. Cougoulat, P. Roux, V. Kostoglodov, A. Husker, J. S. Payero (2012). Triggering of tremors and slow slip event in Guerrero, Mexico, by the 2010 Mw8.8 Maule, Chile, earthquake, *J. Geophys. Res.*, **117**, no. B9, doi: 10.1029/2012JB009160.

Ziv, A., A. M. Rubin, and D. Kilb (2003), Spatiotemporal analyses of earthquake productivity and size distribution: observations and simulations, *B. Seismol. Soc. Am.*, **93**, no. 5, pp. 2069-2081, doi: 10.1785/0120020117.

VITA

Chastity A. Aiken

CHASTITY AIKEN was born in Gastonia, North Carolina under the surname Autry. She attended public schools in Gaston County, North Carolina and received a B.S. in Physics & Astronomy from Georgia State University, Atlanta, Georgia in 2010 before coming to Georgia Tech to pursue a doctorate in Earth & Atmospheric Sciences. She is an invited lifetime member of Sigma Pi Sigma, a physics honors society as well as a lifetime scholar of Achievement Rewards for College Scientists (ARCS) Foundation Atlanta. She is also a member of the American Geophysical Union (AGU) and the Seismological Society of America (SSA).

She was granted a number of awards during her undergraduate and graduate studies. In 2009, she received a National Science Foundation Research Experience for Undergraduates scholarship and studied under the tutelage of Dr. Alexandru Tamasan at the University of Central Florida, Orlando, Florida. She received the Robert Hankla award from the Physics & Astronomy Department at Georgia State University, Atlanta, Georgia in 2010 for her outstanding academic performance. She won a National Science Foundation Graduate Research Fellowship in 2012 and an ARCS Foundation award in 2013 as well as 2014, one of which was for the global impact of her work. She also received an Outstanding Student Paper Award for the research she presented at the AGU Fall Meeting in 2013 and Best Paper Award from the Georgia Institute of Technology School of Earth & Atmospheric Sciences in 2015.

Chastity Aiken is the first in her family to receive a B.S. degree as well as a doctorate. After completing her doctorate, she plans to join a research group as a postdoctoral fellow in the Earthquake Research Institute at the University of Tokyo, Tokyo, Japan for a short time. She will then continue her research as a postdoctoral fellow at the Institute for Geophysics, University of Texas - Austin. When she is not working on her research, she enjoys rock climbing, hiking, volunteering, and crocheting. She also has a fondness for animals, especially dogs.